# Mechanisms of Injury Associated with Extracorporeal Shock Wave Lithotripsy (Part I)

Thesis by

Danny D. Howard

In Partial Fulfillment of the Requirements

for the Degree of

Doctor of Philosophy

California Institute of Technology

Pasadena, California

1996

(Submitted April 5, 1996)

# Acknowledgements

First of all I would like to thank God for giving me the strength, knowledge and motivation to complete such an intricate venture.

I am deeply indebted to my advisor, Professor Bradford Sturtevant, for his support and guidance. I am also grateful to Dr. Bruce Hartenbaum and Dr. G. Ravichandran for their support on this project. I would like to thank my thesis committee for their patience in reviewing this document: Professors Hans G. Hornung, Chris E. Brennen, G. Ravichandran and Joe E. Shepherd. Many thanks to the faculty and staff of GALCIT for their support, especially the Aeroshop and Administration staff.

On a personal level I would like to thank my family for their support: my grandparents, Lessie and James Sparks (in memoriam), Lucy and Titus (in memoriam) Howard; my mother and father, Janie B. and Willie J. (in memoriam) Howard; my sisters, Veronica Hill, Carmella Howard, Cosandra Howard and Denise Howard; my best friend and cousin, Tony C. Webber; my dear friends in California, Jean Andino, David Beam, Gabby Beam, Connie Calderón, V. Nenaji Jackson and Frances K. Jackson; and a host of other relatives and friends. I want to extend special thanks to Professor Keith Koenig for his encouragement and guidance.

Lastly, I would like to thank The James Irvine Foundation and The National Institute of Health for their financial support.

# Abstract

Shock waves are focused in extracorporeal shock wave lithotripsy (ESWL) machines to strengths sufficient to fracture kidney stones. Substantial side effects—most of them acute—have resulted from this procedure, including injury to soft tissue. The focusing of shock waves through various layers of tissue is a complex process which stimulates many bio-mechano-chemical responses.

This thesis presents results of an *in vitro* study of the initial mechanical stimulus. Planar nitrocellulose membranes of order 10 $\mu$m thick were used as models of thin tissue structures. Two modes of failure were recorded: Failure due to cavitation collapsing on or near the membranes, and failure induced by altering the structure of shock waves. Tests were done in water at and around F2 to characterize the extent of cavitation damage, and was found to be confined within the focal region, 1.2 cm along the axis of focus.

Scattering media were used to simulate the effects of acoustic nonuniformity of tissue and to alter the structure of focusing shock waves. 40 $\mu$m diameter (average) hollow glass spheres were added to ethylene glycol, glycerine and castor oil to vary the properties of the scattering media. Multiple layer samples of various types of phantom tissue were tested in degassed castor oil to gauge the validity of the scattering media. The scattering media and tissue samples increased the rise time—decreased strain rate—in a similar fashion. Membranes were damaged by the decreased strain rate and accumulated effects of the altered structure: After about 20 or so shocks immersed in the scattering media and after about 100 shocks behind the tissue samples. The mode of failure was tearing with multiple tears in some cases from about .1 cm to about 3 cm depending of the number of shocks and membrane thickness.

# Contents

# List of Figures

# List of Tables

# Chapter 1  Introduction

## 1.1  Motivation

About two to three percent of the total population will experience the formation of a kidney stone at least once in their lives. It is most unfortunate that these stones have been observed in many cases to recur; surgical removal each occurrence can possibly place the kidney in jeopardy. However, there are alternative non–invasive methods to remove these stones; the method we are concerned with is Extracorporeal Shock Wave Lithotripsy (ESWL). This technique went into service in the United States between 1983 and 1984, and has become the treatment of choice for 60 to 90% of patients with kidney and ureteral calculi (Cao *et al.* 1993; Chuong *et al.* 1989; Gravenstein *et al.* 1986).

When this technique was first introduced, there was no information available about the possible side effects of this procedure. However, it was assumed that these effects were minimal. This deluded the physicians to believe that the ESWL machine was totally safe; hence, some centers tended to exceed the manufacturer's suggested guide lines for the number of shock waves to be administered in a single treatment [98].

Since that time a number of reports have shown that this process can cause substantial acute side effects. This damage includes the following: bleeding within and around the kidney; loss of image contrast between the inner and outer kidney in magnetic resonance imaging, perhaps due to a release of fluids throughout the kidney; a decrease in blood flow through the kidney; destruction of red and white blood cells in the blood system; injury to other organs, including the liver, skeletal muscle tissue, the pancreas and gastrointestinal systems; bruising of the skin where the shock wave enters and exits; and blockage of the ureter by fragments of a kidney stone (Gravenstein *et al.* 1986).

# 1.2 Chosen Lithotripter Machine

There are several types of lithotripters on the market that generate shock waves by different methods, utilizing electrohydraulic, electromagnetic and piezoelectric shock wave generators. In the current study, an electrohydraulic shock wave generator was used. This machine was design to replicate a modified Dornier model HM-3, which is by far the most widely used and effective in renal stone operations; however, this machine is not an exact replica. The research lithotripter—the detailed design of this machine will be discussed in the next chapter—has four essential parts: high voltage capacitors, a discharge system, electrode and brass ellipsoidal reflector.

Capacitors are charged to a high voltage, 18 kV; the discharge system dumps this energy across an electrode in a time of order 2 $\mu$s. The electrode is precisely located at the focal point (F1) of the reflector; the gap separating the tips is initially .4 mm, but they are eroded with each discharge. A weak aqueous solution of sodium bicarbonate fills the ellipsoid, so when the voltage is discharged, a plasma channel forms. This is followed by a sharp increase in the current causing a large amount of energy to be transfered through the small plasma channel. The temperature increases steeply causing the plasma channel to expand which produces a high transient pressure in the water leading to the formation of a shock wave. A 261° solid angle sector of the shock wave reflects off the ellipsoid and is focused at the second focal point (F2)—the location where the test specimen (or kidney stone) is placed.

This machine suffers from an inherent defect. In an ideal situation the arc takes the shortest path—directly across the gap, generating a shock wave precisely at F1. Unfortunately, this is not always the chosen path, so the actual F1 does not always coincide with the geometrical F1. Also, the instability of F1 increases as the electrode is eroded. As will be seen in a later chapter, a small aberration in F1 can lead to a large aberration in F2, causing an imperfect focus: The shock wave becomes crossed and folded.

# 1.3 Current Study Objectives

The objective of this study is to find mechanisms of injury associated with electro-hydraulic lithotripter machines. This was done by studying and exploiting different aspects of focused shock waves. Other workers in this area have studied in detail the process of stone comminution, but few have studied injury to tissue (Coleman *et al.* 1987; Coleman *et al.* 1991; Coleman & Sanders 1992; Filipczynski *et al.* 1992; Filipczynski *et al.* 1994; Finney *et al.* 1991).

The problem was attacked in the following manner: First, the structure of shock waves were studied in different liquids with varying viscosities, sound speeds and inhomogeneities. Second, the effect of shock waves on thin circular unsupported membranes in the above mentioned configurations was studied. Nitrocellulose membranes were used to simulate biological membranes. This was done to find a link between shock structures and damage observed in the membranes. The membranes are thick enough to resist damage due to differential motions induced by shock waves, and thin enough so as not to be susceptible to mode conversion. Additionally, the structure of shock waves and membrane damage were studied behind tissue phantoms.

Chapter 2 describes the experimental methods used in this study. Chapter 3 gives an in–depth review of shock wave focusing. Chapters 4 and 5 present detailed results from pressure and membrane studies; and Chapter 7 summarizes and concludes the study.

# Chapter 2   Experimental Method

## 2.1   Experimental Apparatus

The experimental lithotripter is patterned after the Dornier HM3 commercial lithotripter, and was designed and built largely by Dr. B. Hartenbaum of H–Tech Laboratories Inc. This facility is shown pictorially in Figure 2.1 and in part schematically in Figure 2.3. The basic system consists of a charging system, power pack, triggering unit, pre-break-down network, feed system, brass ellipsoidal reflector and test tank.

### 2.1.1   Charging System

Figure 2.2 shows a schematic of the electrical circuit; the components of the charging system are boxed and labeled. $V_0$ represents the power supply, model HV300–502M, which is manufactured by Plastic Capacitor Inc. This system can generate up to 30 kV DC with a current of 5 mA; it can charge the power pack in about five seconds. R1, 5.82 M$\Omega$, represents the charging resistor. R4 and R5 are components of the voltage divider network across which voltage can be safely measured; their respective values are 182.5 M$\Omega$ and 18.24 k$\Omega$—the voltage is measured across R5.

### 2.1.2   Power Pack

The power pack is a removable unit designed to be charged to high voltages, 22 kV, and discharged rapidly, 2 $\mu$s. The components of the power pack are shown in Figure 2.2, while the mechanical schematic can be seen in Figure 2.3. Two 40 nF capacitors are connected in parallel in order to decrease the total inductance of the system; they are held together by a Plexiglas spacer, two Plexiglas end plates and six Plexiglas support straps. The spark gap holder connects and feeds current from the positive terminals of the capacitors to the spark gap (trigger gap or discharge switch), which
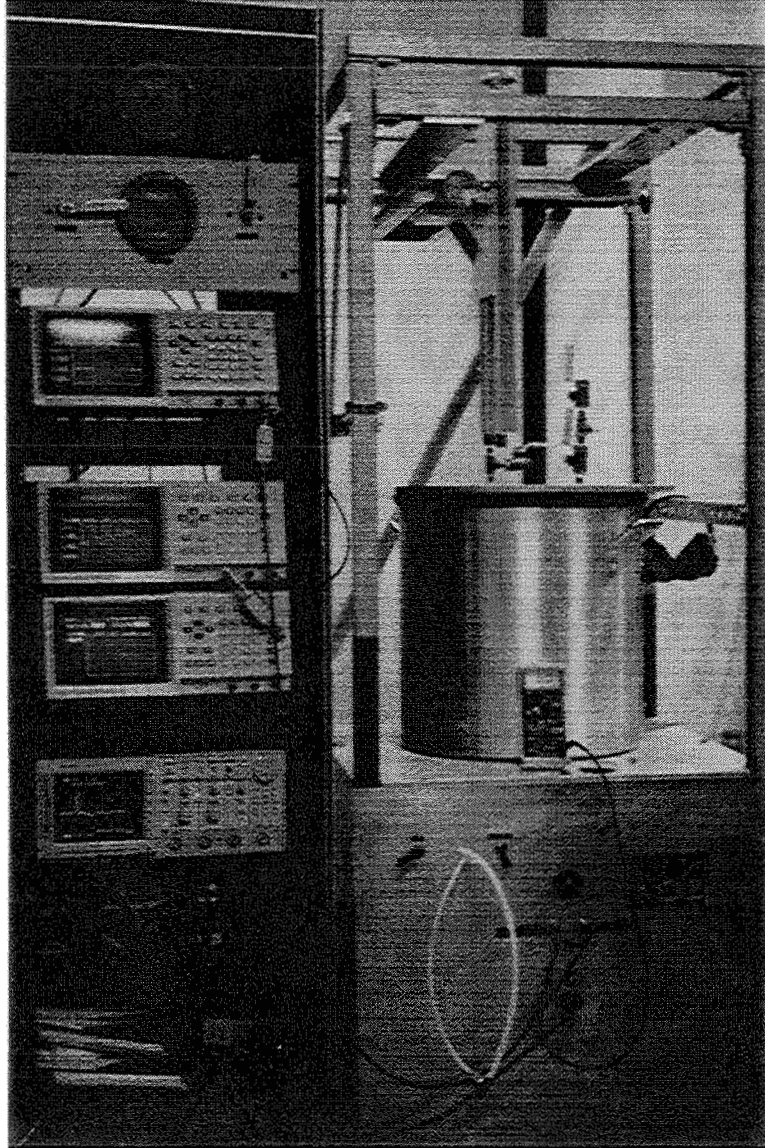
Figure 2.1: Experimental lithotripter machine.
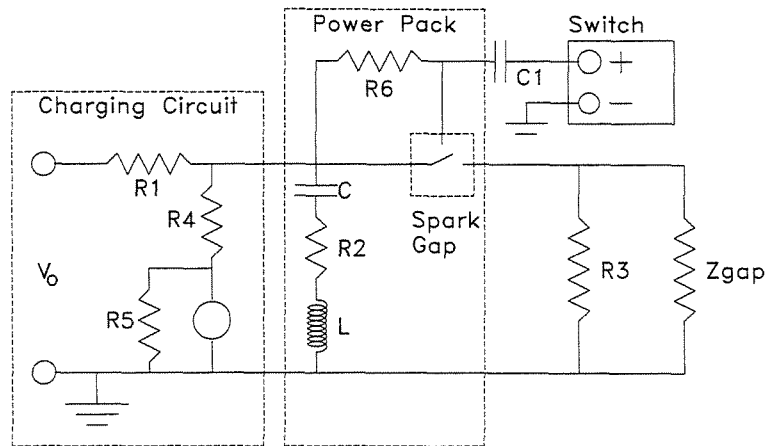
Figure 2.2: Circuit schematic of the experimental lithotripter.

when triggered, relays the current to the coaxial feed system via a positive feed plate mounted on top. The top of the positive feed plate is screwed into the coaxial feed system. On either side of the capacitors, there are negative feed plates which bolt to the negative terminals. Between the negative feed plates and positive feed plate, six sheets of .013 mm–thick mylar provide insulation. These plates are bolted to the circumference of the coaxial feed system.

## 2.1.3 Coaxial Feed System

The coaxial feed system transfers current from the power pack to the electrode. This system has five parts: a shell which holds the electrode and provides a ground path; a floating clamp which bolts the system to the reflector; a phenolic insulator which isolates the electrode; an insulator end cap which isolates the inner conductor; and an inner conductor which transfers current from the positive feed plate to the electrode. Figure 2.4 shows a schematic of the coaxial feed system.

## 2.1.4 Triggering Unit

The triggering unit, EG&G TM–11A Trigger Module, is connected to the spark gap in the power pack, Figure 2.2. This unit provides a high voltage pulse between 20 to 30 kV peak amplitude to the spark gap. The rise time of this pulse is very fast, 1 $\mu$s,

MEMBRANE HOLDER

TEST CONTAINER

TEST TANK

COAXIAL FEED

REFLECTOR

POSITIVE FEED PLATE

POWER PACK

NEGATIVE FEED PLATE

NEGATIVE FEED PLATE
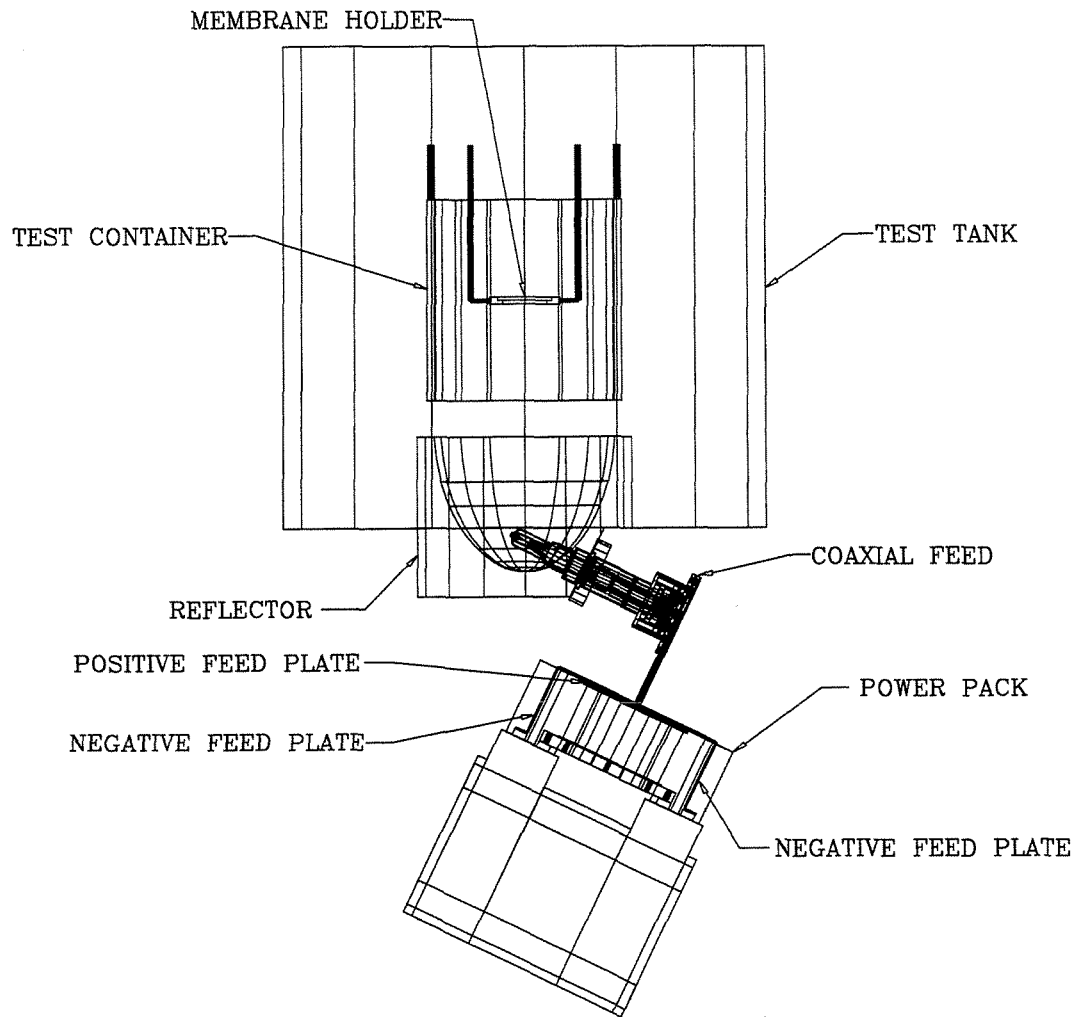
Figure 2.3: Mechanical schematic of the experimental lithotripter.

with a recycle time of about 100 ms nominal. Total capacitance of the system, C1, is 500 pF.

## 2.1.5   Pre-Break-Down Network

The pre-break-down network can be seen in Figure 2.2 as R3, 7.86 k$\Omega$. This network allows current to flow until the electrode has a high enough potential to arc across the gap. It aids in increasing the life of the discharge unit by creating a "softer" discharge. R6, 1 M$\Omega$, is located between the spark gap and positive terminals to aid in the break–down process.
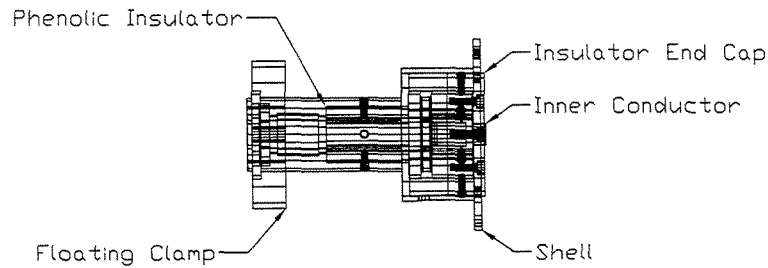
Figure 2.4: Coaxial feed system.

## 2.1.6 Reflector

The reflector is ellipsoidal in shape and made of free–cutting brass. Its dimensions reflect a modification incorporated by Dornier in the original model HM3 lithotripter. The major and minor axes are 143.6 mm and 86 mm, respectively, i.e. the eccentricity is 0.8. The major half axis is truncated by 15 mm. Dornier's HM3 ellipse major and minor axes are 139 mm and 78 mm, respectively, and will be used in the new lithotripter. The electrode is located 43.6 mm from the bottom of the ellipse oriented at an angle of 64° with the major axis; F2 is located 258.6 mm from the bottom of the ellipse. The coaxial feed system bolts to the ellipsoid; a seal is made between the electrode and reflector with a Parker 2-020 O-ring. The ellipsoid is bolted to a cylindrical test tank 45.7 cm in diameter and depth, and sealed with RTV silicone gel.

## 2.2 Associated Systems

The test water is stored in a holding tank, which is 1.2 m in height, and has an outer diameter of 30.5 cm with a capacity of 87 l. It is supported vertically by three legs. Water is transfered from the holding tank to the test tank and back by pulling a vacuum on either tank. The plumbing system consists of 3/8 inch diameter Imperial Eastman tubing connected with Swagelok fittings and Conbraco ball valves. There are two absolute pressure gauges which have a 0 to 15 psi range that monitor the pressure in both tanks simultaneously. When the water is pumped from the holding tank to the test tank, it is filtered with Millipore filters, model CRA501006; this model can

filter particles as small as 0.5 $\mu$m. The vacuum pump is a Duo–Seal vacuum pump, model 1402, manufactured by Welch Inc.

Test specimens, pressure gauges and test container, are located and supported by Velmax slides, model A6024-02. These slides are mounted such that movement in the three principal directions is possible; they are manually driven with a resolution of 51 turns per cm.

A host of meters were used to monitor various parameters during an experiment. The voltage was monitored by a Fluke Multimeter, model 77, the oxygen content by a Cole Parmer Dissolved Oxygen Meter, model 5946–75, the conductivity of the water by a Cole Parmer Conductivity Meter, model 1481-SS, and the capacitance of the PVDF transducers by a GW LCR Meter, model LCR–814.

## 2.3    Instrumentation

Shock pressure was measured with polyvinylidene fluoride (PVDF) transducers designed and built in house. Commercial pressure transducers, such as Imotech and K-tech, possessing the characteristics desired, 50 ns or less rise time, were very expensive, with a relatively short life at F2. Gauges were made from a poled (about 9 $\frac{\mu C}{cm^3}$) PVDF plastic coupon, 25 $\mu$m in thickness, with gold–over–platinum (2500 angstroms thick) leads (model M–25–01–PL), manufactured by K-Tech Inc. The lead configuration, indicated schematically in Figure 2.5, is chosen because platinum adheres to PVDF better than gold, but gold is a better conductor.



| Gold |
| Platinum |
| PVDF |
| Platinum |
| Gold |
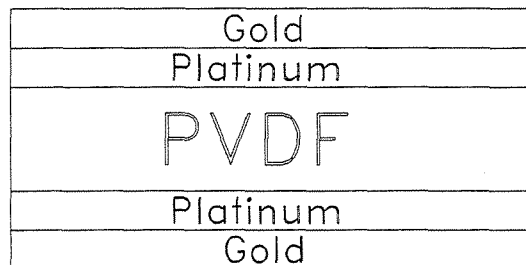
Figure 2.5: Electrical schematic of gauge.

When poled, PVDF exhibits piezoelectric properties; i.e. when the gauge is com-

pressed or placed in tension, a charge is generated. The relationship between charge and stress is very nearly linear. Neglecting cross–coupling terms and in–plane stresses, the following simplified equation results:

$$q\prime = d_{33}\sigma_{33}, \tag{2.1}$$

where $q\prime$, $d_{33}$ and $\sigma_{33}$ represent charge per unit area, a piezoelectric coefficient and normal stress, respectively. The charge and voltage are related by

$$q = CV, \tag{2.2}$$

where C and V represent the capacitance and voltage of the gauge, respectively. The coupons used have a sensitive area of about $1mm^2$ and a piezoelectric coefficient of about 20 pC/N, so the measured voltage is nominally related to the imposed pressure by

$$p = \sigma_{33} = \frac{CV}{Ad_{33}} \tag{2.3}$$

where A represent the active area of the coupon (sensitive spot).
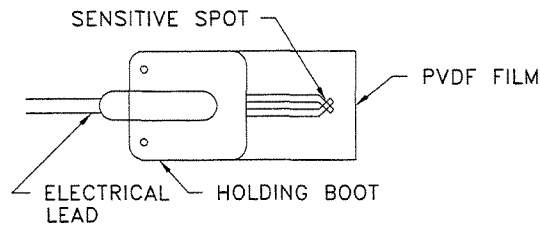


Figure 2.6: Mechanical schematic of gauge.

A gauge was constructed by soldering a coupon to Micro–Dot coaxial cable using low temperature indium–bismuth solder. The coupon and cable were then placed into a mold, and epoxy resin, consisting of equal parts of Eccobond 45 Clear Epoxy Resin and Eccobond 15LV Clear Epoxy Resin Hardener, was injected into the mold. The mold was designed by Dr. B. Hartenbaum. The epoxy was allowed to cure for eight hours, after which a rubberized consistency was formed. A schematic of the finished

gauge can be seen in Figure 2.6.

A lumped-parameter model for this gauge is given in Figure 2.7, where $R_m$ and
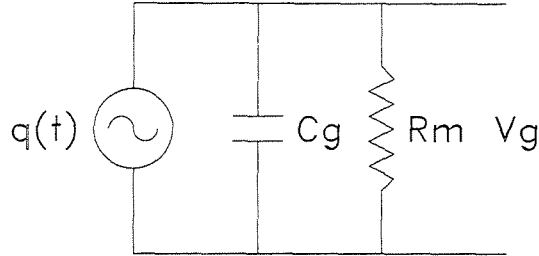


Figure 2.7: Electrical model of gauge.

$C_g$ are the resistance and capacitance of the gauge, including any effects of immersion in liquid. The impedance of Figure 2.7 takes the following form:

$$Z = \frac{R_m}{1 + j\left(\frac{\omega}{\omega_0}\right)} \tag{2.4}$$

where $\omega$, $\omega_0$ and j represent the frequency, corner frequency, $\frac{1}{R_m C_g}$, and $\sqrt{-1}$, respectively. The above model is over simplified if the transducer is immersed in a liquid with a dielectric constant much larger than PVDF (6.7), in this case water (78.5). Additionally, the dielectric constant of water increases when electrolytes are added. Thus, it is necessary to develop a model for water, or to use a liquid with a lower dielectric constant.

The gauge response was measured with a variable frequency power supply, Figure 2.8. Measurements were made in air, water and castor oil. Air and castor oil have dielectric constants close to that of PVDF, 1 and 4.7, respectively. Castor oil was found to give a similar response as air. The solid line is a fit to Equation 2.4. Using the corner frequency, 600 Hz, and the DC response, the capacitance of the gauge was calculated; this is very close to the measured value, 120 pf. At about 18 kHz, the data deviate from the model: This reflects the limited bandwidth of the measuring instrument. The curve in water indicates a very complicated circuit; no model could be found to fit this curve.

In light of this, the gauge was encapsulated in castor oil to make pressure mea-
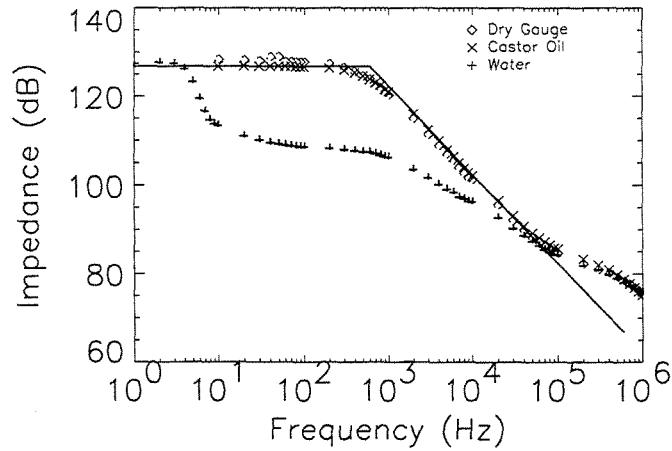
Figure 2.8: Gauge response in different fluids.

surements. There are two additional advantages to this method: 1.) castor oil has essentially the same sound speed and density as water, so the shock wave is not diverted or reflected when traveling from water to castor oil; and 2.) the cavitation threshold of castor oil is not reached in the lithotripter at the experimental conditions. This increases the life of the gauge practically to infinity; whereas, other gauges would eventually erode by collapsing cavities in their vicinity. The encapsulation medium is latex, manufactured by Schmid Laboratories Inc. Once encapsulated in castor oil the rise time in water is 50 ns or better at F2.

A signal conditioner designed by Dr. B. Hartenbaum was used to compensate the signal. It consists of a damping resistor(110 $\Omega$) to damp ringing in the line and a shunt capacitor(130 pF). This network has been proven to reduce the leading edge rise time error from 60 % to 5 %.

## 2.4 Data Acquisition

Data acquisition was accomplished using two types of oscilloscopes; their properties can be seen in Table 2.1. Data were taken directly from Hewlett Packard oscilloscopes, model 54200A, onto the local GALCIT network and a suite of SUN

| Property | Unit | Tektronix | Hewlett Packard |
|----------|------|-----------|-----------------|
| Model | N/A | 540A | 54200A |
| Input Resistance | MΩ | 1.0 | 1.0 |
| Input Capacitance | pF | 10.0 | 14.0 |
| Band Width | MHz | 500.0 | 50.0 |
| Sampling Rate | MS/s | 1000.0 | 200.0 |

Table 2.1: Properties of oscilloscopes.

workstations with the aid of an Iotech bus, model SCSI488/S. Data were saved from the Tektronix oscilloscope, model TDS540A, using $3\frac{1}{2}$ inch floppy disk, and transfered to the computer. Because the sampling rate of the Tektronix oscilloscope is faster, all of the pressure traces shown will be from this machine.

## 2.5 Experimental Conditions

### 2.5.1 Test Liquids

Four test liquids were used: distilled water, castor oil, glycerine and ethylene glycol. The oxygen content of water was monitored and kept constant for all of the experiments, 9.8 ppm. An electrolyte concentration of 620 $\mu$S/cm was used for all of the tests. The necessary liquids and mixtures were degassed in the test tank for at least two hours. Hollow glass micro-spheres were used in some tests. These mico-spheres were manufactured by Emerson and Cuming Inc., and contained a slurry of diameters: 62-100 $\mu$m (51%), 44-62 $\mu$m (23%) and < 44 (12%). The wall thickness of each mico-sphere is approximately 1.2 $\mu$m thick. The properties of the liquids can be seen in Table 2.2, and solids in Table 2.3.

### 2.5.2 Membranes

The membranes were made from a nitrocellulose solution, manufactured by Micro–X Inc. They were made by drawing precise amounts of solution, with a syringe and releasing it in a shallow container of water 25 × 25 × 5 cm deep. The solution spreads as a result of surface tension and dries forming a nitrocellulose membrane. The

membranes are on the order of 10 $\mu$m thick. The order of thickness was determined by electron microscopy at Caltech. Circular plywood holders, 1.6 mm thick with a 1 cm O.D. and 4.1 cm I.D., were sprayed with glue and placed on the membrane. After lifting from the water, the membrane was then trimmed to conform to the holder. Membrane properties can be found in Table 2.5 (Hercules Inc. 1995). The membranes appear to be multi-colored because of constructive and destructive interference of reflected and refracted light rays, and the variation in membrane thickness.

Pictures were taken before and after each run using a Nikon 35 mm camera, model N6006, and a Nikon zoom lens. The zoom lens, Nikkor AF, is capable of a zoom range from 70 mm to 210 mm. Between the camera and zoom lens a Nikon Bellow, model PB-6, was placed. This device allows the camera to be moved in order to place the film at the image location. By adjusting the zoom lens and bellow, detailed photographs of of damage were taken. The membranes were placed against a black background when photographed so that damage areas would appear dark.

## 2.5.3   Test Container

The test container, which was used to hold the test liquid, is 19.0 cm in height and has a 18.5 cm outer diameter with a wall thickness of 1.0 cm. It was made from polyvinyl chloride (PVC) plastic; the bottom was made from .08 mm thick low density polyethylene, manufactured by TRM Inc. (Table 2.3). A test specimen, pressure gauge or membrane was placed such that the shock wave traversed 7.5 cm of test liquid before reaching F2. Both test container and specimen are suspended from the same support.

| Property | Unit | Water | Castor Oil | Glycerine | Ethylene Glycol |
|---|---|---|---|---|---|
| Chemical Formula | N/A | $H_2O$ | $C_{11}H_{10}O_{10}$ | $C_3H_8O_3$ | $C_2H_6O_2$ |
| Molecular Weight | N/A | 18.02 | N/A | 92.096 | 62.070 |
| Vapor Pressure@20C | Pa | 2330.00 | N/A | .014 | 10.000 |
| Boiling Point@1atm | K | 373.10 | N/A | 563.400 | 470.000 |
| Density@25C | $kg/m^3$ | 997.00 | 956.1 | 1259.00 | 1097.000 |
| Sound Speed | m/s | 1500.00 | 1474.0 | 1909.000 | 1644.000 |
| Surface Tension@300K | $N/m \times 10$ | 0.72 | N/A | 0.633 | 0.482 |
| Viscosity@300K | $Ns/m^2 \times 10^3$ | 0.89 | 650.0 | 950.000 | 162.000 |
| Dielectric Constant | N/A | 78.50 | 4.7 | 40.000 | 37.700 |

Table 2.2: Physical properties of test liquids.

| Property | Unit | PVDF | Poly-ethylene | Gum Rubber | Glass Spheres | PVC |
|---|---|---|---|---|---|---|
| Dielectric Constant | N/A | 6.1 | 2.3 | N/A | N/A | 3.5 |
| Density@25C | $kg/m^3$ | 1779.0 | 900.0 | 950.0 | 238.0 | 1392.0 |
| Longitudinal Sound Speed | m/s | 1930.0 | 1950.0 | 1550.0 | 3980.0 | 2376.0 |
| Shear Sound Speed | m/s | 775.0 | 540.0 | N/A | 2380.0 | N/A |
| Particle Diameter | $\mu$m | N/A | N/A | N/A | 65.0 | N/A |
| Thickness | $\mu$m | 22.0 | 100.0 | 20.0 | 1.2 | 1.0 |

Table 2.3: Physical Properties of solids.

| Property | Unit | Muscle | Fat | Skin | Kidney |
|---|---|---|---|---|---|
| Density@25C | $kg/m^3$ | 1050.0 | 920.0 | 1050.0 | 1050.0 |
| Longitudinal Sound Speed | m/s | 1580.0 | 1430.0 | 1580.0 | 1580.0 |

Table 2.4: Physical Properties of solids.

| Property | Unit | Nitro–Cellulose |
|---|---|---|
| Tensile Strength | MPa | 110.0 |
| Modulus of Elasticity | GPa | 1.4 |
| Dielectric Constant | N/A | 6.0 |
| Density@25C | $kg/m^3$ | 1600.0 |
| Index of Refraction | N/A | 1.5 |
| Thickness | $\mu$m | 10.0 |

Table 2.5: Physical properties of nitrocellulose.

# Chapter 3   Converging Shock Waves

There are many instances where shock waves are focused naturally—plane shock waves traveling in inhomogeneous or moving media—or intentionally—focusing of spherical waves to break kidney stones. The behavior of the shock wave in these encounters depends on the strength of the initial shock wave and, of course, the medium in which the shock wave is traveling. Regardless of the vehicle, once formed the wave converges to a point or region where the amplitude is a maximum at the center of focus, and diverges from this point. Since a focusing shock wave is curved and of nonuniform strength, shear develops in the shocked fluid. Diffracted waves perform the function of equilibrating the downstream flow.

This chapter reviews the behavior of focused shock waves. A brief review of geometrical acoustic and shock dynamics is given along with a discussion of different types of foci, followed by implications of wrinkling shock waves and, finally, the effects of an offset F1.

## 3.1   Theory of Converging Waves

The limit of a zero thickness shock wave with a small amplitude is a sound pulse; waves of this type can be handled linearly by geometrical acoustics. It should be pointed out that the actual process of focusing has nonlinear effects, and can not be predicted exactly by geometrical acoustics. In fact for strong converging shock waves, nonlinear effects dominate. Figure 3.1a shows the focusing of a sound pulse; the thick line represents a shock wave, and the lines with arrows represent rays. The ray trajectories are straight and orthogonal to the wave front at its respective location, and the sound speed along each ray is constant.

The amplitude of the front is inversely proportional to the ray tube area. When the ray tube area becomes zero at the focus, the amplitude goes to infinity. Obviously,

geometrical acoustics is not valid near singular regions of this nature. In actuality, diffracted waves are present to support this difference and eventually equilibrate the pressure field far down stream. This method is used to understand the physical process of shock wave focusing in its initial stages.

Geometrical acoustics assumes a zero thickness shock wave and an invariant sound speed along the rays, as well as small amplitude waves. Shock waves are at least a few mean free paths in thickness, and the amplitude of the wave is finite. One result is an increase in wave speed with amplitude. Whitham takes these factors into account in his theory of Shock Dynamics (Whitham 1974). In this method he uses an approach similar to geometrical acoustics with rays normal to the shock front, but the shock front is allowed to travel at different speeds along different rays depending on its amplitude: The rays are bent, and the shock front is turned as a result. Each section of the shock wave is treated as a plane shock wave traveling in a curved ray tube.

The concave portion of the shock front is accelerated relative to other parts of the shock wave and is amplified. With this, the rays curve causing the shock wave to be flattened; no loop is formed like that in the case of the weak amplitude, zero thickness shock wave. This process shows how nonlinear effects change the focusing process. However, it should be kept in mind that shock dynamics does not consider shock interactions where new shocks might be formed—the Euler equation must be used for problems of such complexity. This approach would give a better qualitative description of the complex interactions at the focus.

## 3.2   Classification of Foci

There are three types of foci that can be identified: caustic, arêtes and perfect foci. Sturtevant and Kulkarny differentiated the types of foci by expressing the radius of curvature of the traveling shock front as a function of arc length and time (Sturtevant & Kulkarny 1976).

$$R(S, t) = R(S, 0) - ct \qquad (3.1)$$

where c is the speed of sound. With this the foci can be defined as follows:

(i)  R(S,t) = 0 implies a caustic

(ii)  $R(S,t) = \frac{\partial R(S,t)}{\partial S} = 0$ implies an arête, and

(iii)  R(S,t) = 0 for all S in some nonzero range of S

implies a perfect focus.

A local minimum in R will lead to a cusp caustic, arête, and a discontinuity in the radius of the shock wave generates a caustic with a constant radius of curvature called a smooth caustic or simply a caustic.

### 3.2.1  Acoustic Waves

If we assume that the fluid is inviscid, homogeneous and isotropic, and the flow is irrotational with only small perturbations, then the continuity and inviscid Eulers equations can be linearized—the resulting equations do not contain products of unknowns or products of unknowns with derivatives of unknowns—and combined to form the wave equation,

$$\frac{\partial^2 \phi}{\partial t^2} = c^2{}_0 \nabla^2 \phi \tag{3.2}$$

where $\phi$ and $c_0$ represent the velocity potential and local speed of sound. Entropy change in this process is neglectable—it changes with third order in pressure. The solution to the above equation can be seen as follows:

$$\phi = B e^{i(\Sigma \pm \omega t)} \tag{3.3}$$

where $\Sigma \pm \omega t = $ constant, $\Sigma(x)$ is called the Eikonal, and B(x) and $\omega$ represents the amplitude and frequency, respectively. This leads to the Eikonal equation,

$$|\nabla \Sigma| = k \tag{3.4}$$

where k, $\frac{\omega}{c}$, represents a wave number. Because $\Sigma$ defines the surface, then $\nabla \Sigma$ defines the rays (Thompson 1972).

## 3.2.2 Finite Amplitude Shock Waves

A finite amplitude shock wave is modified as it is focused by nonlinear effects. Since velocity increases behind a shock wave, successive waves eventually catch up with it and increase its amplitude and thickness. Whithams Shock Dynamics deals with these nonlinear effects. The objective of this method is to describe a shock front in a situation where there is an interaction between a shock wave and some geometry, along with weak interactions with down stream waves.

In this approach Whithman used rays normal to the wave front, but allowed each ray to travel at different speeds depending on its local amplitude, so the rays curve away from regions of large amplitude. The shock is constructed as a series of plane shock waves traveling in a straight tube with a slowly varying cross section. Waves behind the shock wave are neglected.

Whitham used the one-dimensional isentropic unsteady flow equations from which the characteristic rule was developed, along with the Rankine–Hugoniot jump conditions to derive the CCW—Chester, Chisnel and Whitham—theory (Whitham 1974; Chester 1954; Chisnell 1955; Chisnell 1957). For weak shock waves, the following form is obtained:

$$4\frac{M}{M^2 - 1}dM = \frac{dA}{A}.$$

(3.5)

Next equations were derived to describe how the area changed:

$$\frac{\partial \theta}{\partial \beta} = \frac{1}{M}\frac{\partial A}{\partial \alpha}$$

(3.6)

$$\frac{\partial \theta}{\partial \alpha} = -\frac{1}{A}\frac{\partial M}{\partial \beta}$$

(3.7)

where $\alpha$ and $\beta$ represent the ray trajectories and normals, respectively. $\theta$, M and A are then found as functions of $\alpha$ and $\beta$. The shock position is then found by integrating along the rays.

The system describing the shock motion is a set of hyperbolic partial differential equations. There are waves traveling along the deforming shock wave; these waves travel at the local speed of sound of this region. This can be seen by obtaining characteristics of Equations 3.6 and 3.7,

$$c = \sqrt{-\frac{M}{AA'}}. \tag{3.8}$$

These waves carry information of shape change and shock strength along the shock wave. Since these waves are nonlinear and $c(M)$ is an increasing function of M, an increase in Mach number will lead to the breaking of these waves. A shock wave with a discontinuity in slope and Mach number will be referred to as a shock–shock. Shock–shocks and three–shock intersections occur quite often in concave shock fronts.

## 3.3   Diffracted Waves

Waves that form behind the focusing main front are called diffracted waves. Because of pressure gradients along the front, the flow will be nonuniform down stream. Diffracted waves act to drive the pressure to a uniform state. An example of this can be seen in Figure 3.1a for the perfect focus of a sound pulse. Diffracted waves are initiated at the aperture of the reflector and travel, at the speed of sound in this region, radially outwards while staying attached to the main front. These waves are generally not shock waves—even if the wave front is a strong shock wave—but expansion or compression waves (Kulkarny 1975). Diffracted waves that travel into the high pressure region are expansion waves, and diffracted waves that travel into the low pressure region are compression waves: The net effect is to equilibrate the pressure field.

If the curvature of the shock wave is discontinuous, a discontinuity in pressure will develop which will grow. This location merits the creation of a reflected wave field (Mach reflection). However, for an arête and a caustic, the curvature and amplitude of the shock wave will change continuously along the front. Even though there

are no distinct diffraction fronts observed in the case of an arête, as will be seen, the same effects mentioned above must be exhibited. For a finite thickness shock wave near the focus, diffraction waves act to weaken the shock wave at the focus, making the amplitude finite. On the other hand, if shock waves have essentially no amplitude, diffracted waves do not affect the amplitude, and singularities predicted by geometrical acoustics prevail.

## 3.4   Observed Foci

Sturtevant and Kulkarny performed a detailed study of focused weak shock waves using shadow graphs and pressure measurements Sturtevant & Kulkarny 1976. The shocks were brought to three types of foci—perfect foci, arête and caustic—by focusing an initially plane shock wave using different reflectors. These experiments were performed in a 17 inch shock tube using air as the test gas. Because the current study is concerned with shock wave focusing, each type of focus will be considered in detail.

### 3.4.1   Perfect Foci

Four processes of a perfect focus were characterized: perfect focus of a sound pulse; perfect focus of a weak shock wave; perfect focus of a moderately strong shock wave; and perfect focus of a strong shock wave. Figure 3.1a shows a perfect focus of a sound pulse. A plane shock wave was reflected off a concave reflector with a sharp edge. Diffraction waves—initiated at the sharp edge—take two forms: expansion waves behind the shock wave and compression waves in the low pressure field. The diffracted expansion waves cross when the main front reaches the focus. This is the point of maximum amplitude, and also the point of infinite amplitude predicted by geometrical acoustics. However, the diffracted expansion waves overtake the main front at this point and decrease the amplitude. Beyond the focal point, the diffracted compression waves cross and precede the main front, forming a triangular loop. In the experiments, this type of a focus occurred at an initial Mach number of 1.005.

(a) Sound pulse (acoustic theory).  (b) Weak shock wave.



(c) Moderate strength shock wave.  (d) Strong shock wave.
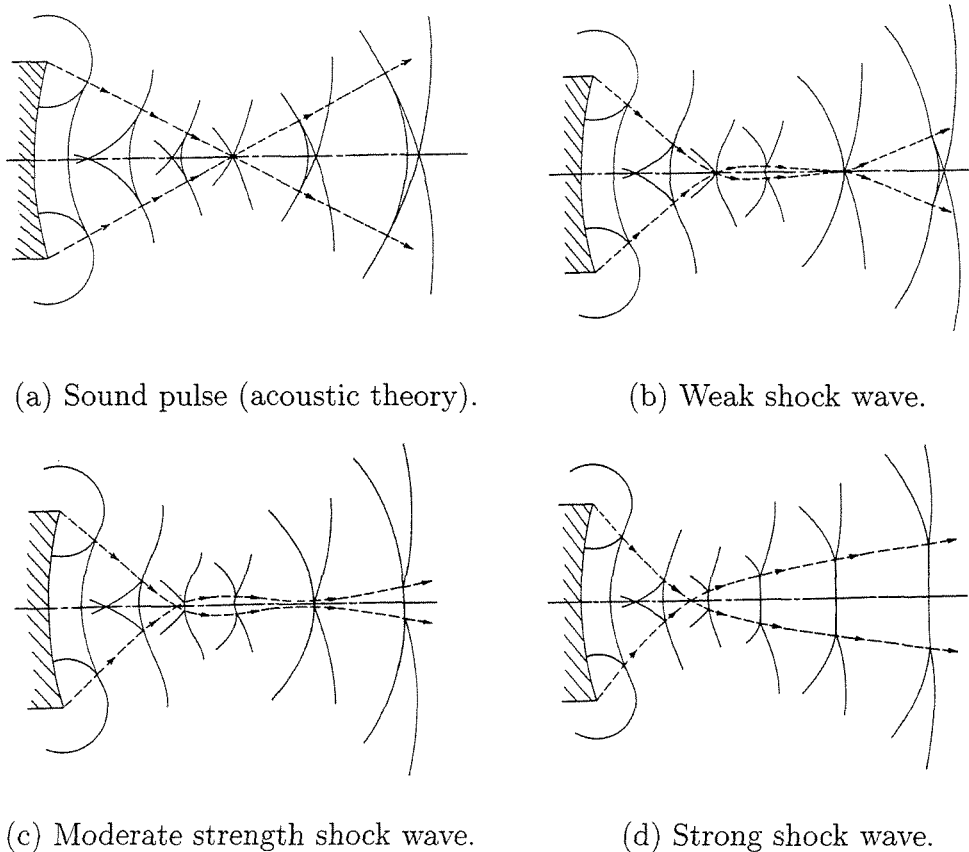
Figure 3.1: Types of focus behavior at a perfect focus.

Figure 3.1b shows a schematic of a perfect focus of a weak shock wave. This process is simular to that of a sound pulse; however, the diffracted expansion waves cross in front of the geometrical focus. This point marks the beginning of the focal region and two three–shock intersections. The stem–shock grows and shortens as the diffracted compression waves cross to mark the end of the focal region. As the initial shock strength increases, the stem–shock becomes stronger and more plane. For the moderately strong shock case, the stem–shock shortens, but the shock–shocks never meet: The diffracted compression waves never cross or fold. The focal region is marked by the crossing of the diffracted expansion waves on one end and the location where the stem–shock becomes the shortest on the other.

The strong shock case exhibits simular features: Diffracted expansion waves cross and evolve into two three–shock intersections before the shock front reaches the focus However, these events occur much earlier for the strong shock wave. The stem–

shock is very plane, and instead of closing, it spreads apart, making the focal region infinite—this is a strong nonlinear effect.

### 3.4.2 Arête



(a) Sound pulse (acoustic theory).      (b) Weak shock wave.

(c) Moderate strength shock wave.      (d) Strong shock wave.
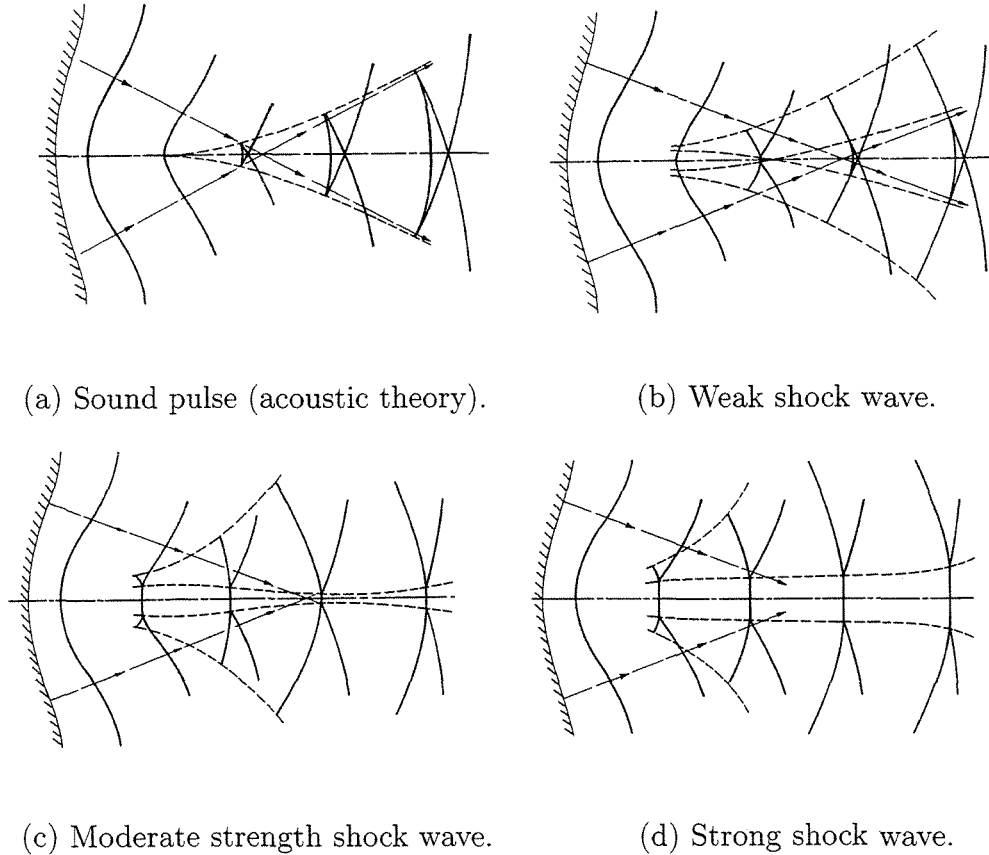
Figure 3.2: Types of focus behavior at an arête focus.

The focusing of a caustic with a cusp is known as an arête. Four types of arête were distinguished: focusing of a sound pulse; focusing of a weak shock wave; focusing of a moderately strong shock wave; and focusing of a strong shock wave. In these experiments an arête was formed by reflecting an initially plane shock wave off a reflector with no sharp edge—as a result, no diffraction waves were formed. The amplitude change is continuous along this type of a shock front; the pressure gradients set up wave fields to equilibrate the flow.

For the case of a sound pulse, Figure 3.2a, the wave becomes crossed and folded coming out of the cusp. A triangular loop is formed in which the pressure is high.

The loop increases indefinitely, and the wave diverges. For a weak shock wave, Figure 3.2b, diffraction waves—both compression and expansion waves—are created at the cusp of the caustic. Diffracted compression waves help to form two sets of three-shock intersections with the main front, while the diffracted expansion waves follow the main front to drop the pressure. As the diffracted compression waves propagate, they become stronger. The main front crosses and folds in front of the focal point.

As the initial shock strength becomes stronger, the location of the cusp becomes closer to the reflector. In the case of a moderately strong shock wave, the two three-shock intersections are formed. The stem–shock becomes stronger: It grows and shortens to a minimum value, but the two shock–shocks never touch—from the cusp to this location is called the focal region. Beyond the focal region, the diffracted compression waves strengthen into a shock wave, and the stem–shock begins to grow again. The only difference in the strong shock case is that the cusp of the caustic is closer to the reflector, and once the two three–shock intersections are formed, they never close, but grow indefinitely , forming an infinite focal region.

### 3.4.3 Caustic

The last type of focus defined by Sturtevant and Kulkarny is a caustic with a constant radius of curvature, known as a "smooth" caustic or simply a caustic, Figure 3.3; this is different from an arête which has a cusp and no constant radius of curvature. In order to generate this type of a wave, a reflector with an aperture half smooth and sharp was used. Diffracted compression and expansion waves were formed at the sharp corner. Diffracted compression waves crossed the main front creating a discontinuity in the radius of curvature, marking the beginning of a caustic; this location is an intersection point of three waves for a sound pulse—two compression waves and the main front. For stronger shock waves, there is a three shock intersection: the stem–shock, diffracted compression waves and diffraction shock. The top half of this wave is reminiscent of an arête, while the lower half is reminiscent of a perfect focus.
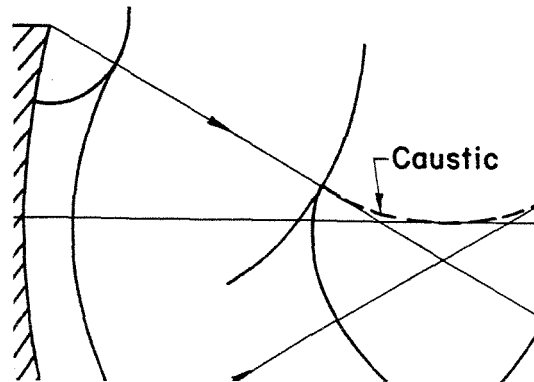
Figure 3.3: Sound pulse at a smooth caustic.
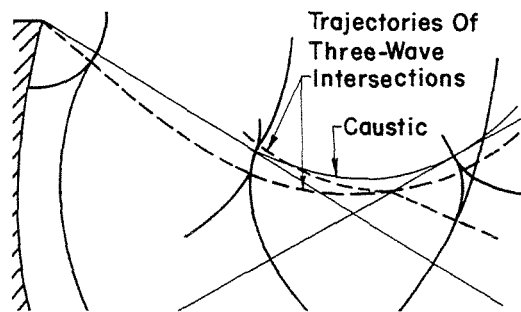
Figure 3.4: Weak shock at a smooth caustic.

## 3.5 Shock Waves in Random Medium

Although there is much literature on waves in inhomogeneous media, few discuss focusing of shock waves in this environment. When shock waves travel in a inhomogeneous medium, the shock wave has an effect on the fluctuations in the fluid, and the non-uniformities have an effect on the shock wave. This is particularly true for moderate strength shocks and large non-uniformities. If the wave is weak enough to be considered acoustic, the non-uniform media can be treated by using scattering theory which is linear, and the acoustic wave does not effect the non-uniformities (Hesselink & Sturtevant 1988). Kulkarny and White (1982) investigated focusing of shock waves through turbulent, inhomogeneous medium by using geometrical acoustics; however, they used nonlinear terms which were not used in previous work. They showed computationally that caustics occurred on rays, and there is an exponential growth of the fluctuations of the ray tube area.

In order to understand the effects of shock waves traveling in random medium, consider the simple problem of a plane shock wave traveling through a inhomogeneous medium. Hesselink studied the propagation of a plane shock wave traveling through a inhomogeneous mixture of helium and refrigerant (Hesselink 1977). He showed that shock waves with $M_s$ < 1.1 were affected by the inhomogeneities, and stronger shock waves became stable. Plane shock waves were strongly modified by the random medium; instead of wrinkling the shock front, a multiplicity of fronts were created. In other words, there is a tendency to focus that is so strong that a number of caustics occur. So the effect of random media on a shock wave is to act as an array of lenses, focusing and defocusing the shock wave: The refraction from this process is so strong that the shock wave becomes multiply folded.

## 3.6   Offset Focus Location

An unfortunate indigenous characteristic of the Dornier ESWL machine is that the geometrical F1 and actual F1 are not always coincidental—F1 is an uncontrollable variable. This is, to say the least, an undesirable feature in a controlled experimental environment. However, there was no feasible way to rectify this problem. So, this varying parameter had to be taken into account when designing experiments and analyzing data. To obtain a qualitative understanding of the effects of an offset F1, it is useful to study cases using acoustic ray tracing. Figure 3.5 (computed by Cates 1996) shows a ray tracing result obtained by moving a source either to the left or right, $\pm\zeta$, or up or down, $\pm\eta$, from the geometrical F1. The computational and experimental ellipse have the same eccentricity, 0.8. In each plot the curve drawn is a connection of crossed rays. If the source were located at the geometrical F1, all of the rays would intersect at the geometrical F2. These curves, caustics, describe the path traveled by a fold in the shock wave. It is interesting to note the deviation in the path of the caustic for a very small change in source location.
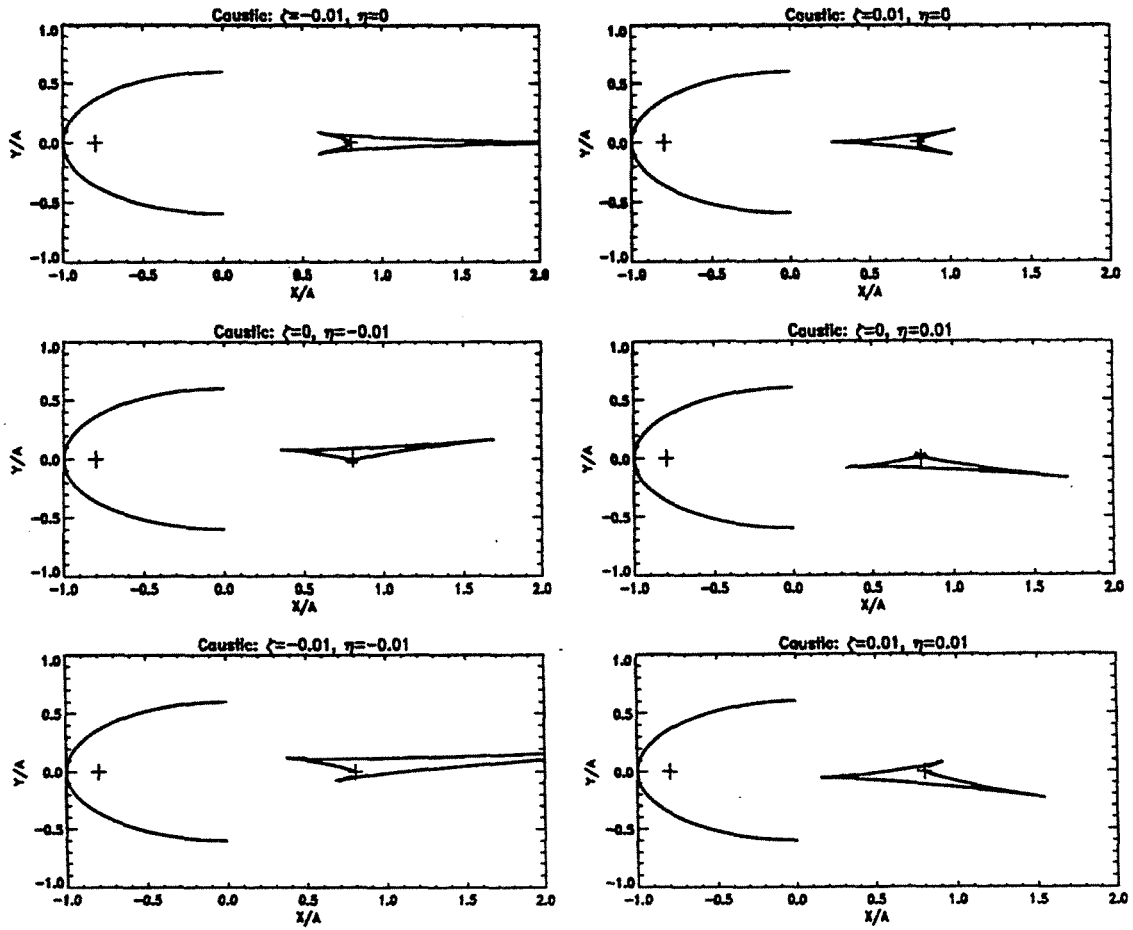
Figure 3.5: Paths of caustics resulting from off–set focus. "A" represent the major axis of the ellipse; $\zeta$ and $\eta$ are normalized x and y coordinates, respectively.

# Chapter 4   Pressure Experiments

There are two complications which make interpretation of pressure data very difficult without flow visualization: The influence of nonlinear effects, and the instability of F1. The aforementioned PVDF pressure transducers (Section 2.3) were used to measure pressure in and around the geometrical F2 in different liquids and behind phantom tissue; the ESWL machine was set to discharge at 18 kV in all cases.

## 4.1   Pressure Measurements in Water

Many workers have looked at the problem of focusing shock waves in water (Coleman *et al.* 1989; Coleman *et al.* 1987; Coleman *et al.* 1991; Coleman & Sanders 1992; Muller 1987; Muller 1988; Sommerfield 1986; Sturtevant 1990; Takayama 1993). Coleman *et al.* (1991) provides both experimental and numerical pressure traces at and around the focus of an ESWL machine in various liquids. Müller *et al.* (1987, 1988) conducted a thorough study of focusing of shock waves in water with both shallow and deep reflectors, using shadowgraphs and pressure measurements. Figure 4.1 shows a
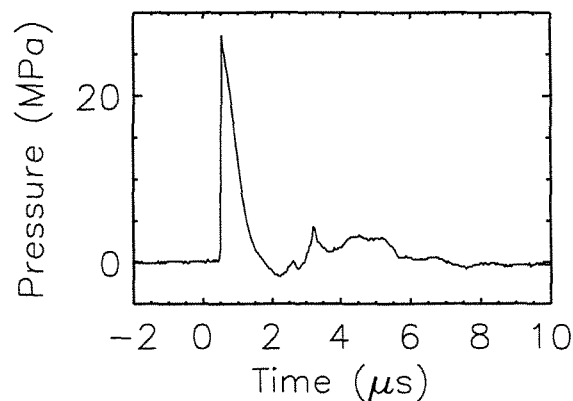


Figure 4.1: Pressure at F2 in water; rise time 50 ns.

pressure trace in water at F2 for a 18 kV discharge. This trace has a peak positive and negative pressure of about 28 MPa and 2 MPa, respectively. After the diffracted expansion waves pass—dropping the pressure below ambient conditions—other waves are noticeable which bring the fluid back to an equilibrium state. Shock waves are very thin; the rise time in Figure 4.1 is about 50 ns, which corresponds to a shock thickness of 75.7 $\mu$m. However, if we use an approximate formula for weak shock waves (Thompson 1972):

$$\delta = \frac{8}{3} \frac{\mu_0}{\rho_0 \left( c - a_0 \right)} \tag{4.1}$$

where $\mu_0$, $\rho_0$, c and $a_0$ represent the viscosity, density, shock speed and local speed of sound, respectively, we determine 79 nm (56 ps rise time). However, if we consider the thickness of the gauge, 22 $\mu$m, it would take the shock wave 12 ns to compress the PVDF—K-Tech quotes a 15 ns rise time for its bare gauges. The rise time, 50 ns, is a base to peak measurement of the rise time, as are all of the rise times quoted, and are not the conventional 10 to 90 % method commonly used. If the measurement is made in this manner, the rise time is 34 ns. The smallest rise time measured was 40 ns base to peak. This can be explained by only 3.4° misalignment of the 1 mm sensitive spot of the transducer relative to the shock wave.

If we assume that this trace is representative of a weak shock wave at a perfect focus, then we can correlate this trace with the schematic in Figure 3.1b; the steep part of the pressure trace represents the Mach stem, and the low pressure field represents crossed diffracted expansion waves. To further substantiate that Figure 3.1b represents the case of interest, Figures 4.2 and 4.3 show a series of pressure measurements taken along the line of focus.

Figure 4.2a shows a trace 2 cm in front of F2. The diffracted expansions from the aperture have crossed, but have not overtaken the main front—it is 0.5 $\mu$s behind. These waves overtake the main front at about 0.4 cm in front of F2, forming a Mach stem and two three–shock intersections, and mark the beginning of the focal region. Two effects are obvious as the main front closes on F2, and the Mach stem becomes
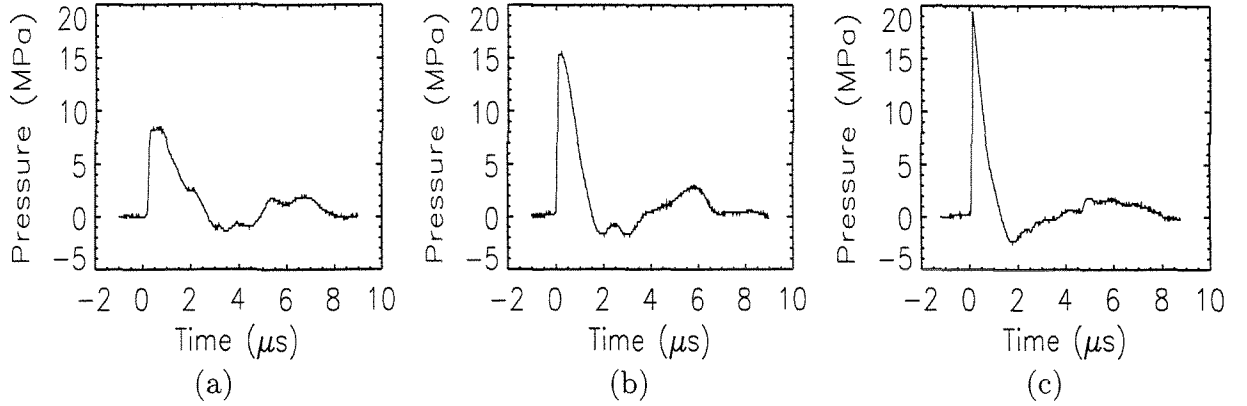
Figure 4.2: a.) F2-2.0 cm, b.) F2-0.8 cm and c.) F2; in water.
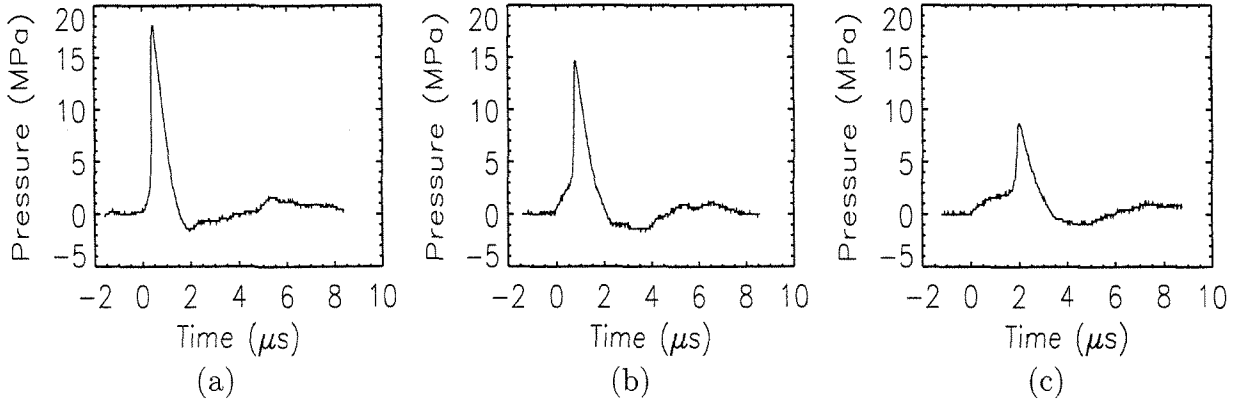


Figure 4.3: a.) F2+1.0 cm, b.) F2+2.0 cm and c.) F2+4.0 cm; in water.

stronger: There is an increase in the maximum and minimum pressure, and the shock wave becomes steeper. Behind the focus, the Mach stem shrinks to zero, and the diffracted compression waves cross 1 cm behind F2—the diffracted waves can be seen in Figures 4.3a, b, and c as precursor waves. This intersection begins to move ahead of the main front, indicating that the triangular loop is growing. The vertical extent of the focus zone is about 1.4 cm.

Because the Mach stem is some–what planar, the shock speed can be estimated by solving the jump equations along with the Modified Taits Equation:

$$P = A\rho^{\gamma} - B \qquad (4.2)$$

$$\rho_1 w_1 = \rho_2 w_2 \tag{4.3}$$

$$P_1 + \rho_1 w_1{}^2 = P_2 + \rho_2 w_2{}^2 \tag{4.4}$$

where A, B,$\gamma$, P, $\rho$ and w represent constants of the Modified Taits Equation, pressure, density and relative velocity, and the subscripts 1 and 2 denote upstream and downstream conditions, respectively. Combining these equations gives the following relation:

$$M_1{}^2 = \frac{\beta}{\gamma} \frac{\beta^\gamma - 1}{\beta - 1} \tag{4.5}$$

where $\beta(M) = \frac{\rho_2}{\rho_1}$ and $M_1$ represents the shock wave Mach number. Because this equation requires a numerical solution, we can obtain an estimate for weak shocks by expanding Equation 4.5 is small powers of $\beta$ - 1.

$$\beta = 1 + \frac{4\gamma}{\gamma + 1} (M_1 - 1) \tag{4.6}$$

For a Mach stem that has an amplitude of 20 MPa, $M_1 = 1.02$, which is a weak shock wave. A plot of the maximum and minimum pressures, as well as standard deviations, versus distance along the line of focus can be seen in Figure 4.4. The mean maximum and minimum pressures occur about 0.4 cm and 0.25 cm behind F2 respectively. The standard deviations result from imperfect focusing.

## 4.2  Pressure Measurements In Other Fluids

Pressure measurements were made at the geometrical F2—the actual and geometrical F2 can differ for some liquids—in three other liquids: ethylene glycol, castor oil and glycerine, in order of increasing viscosity. Figure 4.5 shows a pressure trace in ethylene glycol at the geometrical F2; it has a viscosity about 20 times that of water. The maximum and minimum pressures and rise time are similar to those measured in
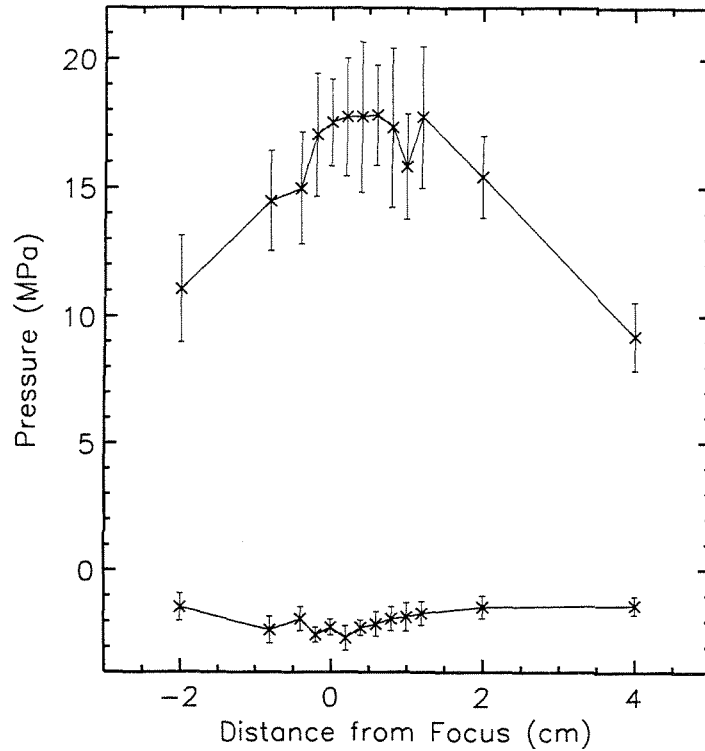
Figure 4.4: Pressure along the axis of focus in water.

water, 20 MPa, 2.5 MPa and 60 ns, respectively. Evidently, increasing the viscosity by an order of magnitude has no effect on the shock wave. Figure 4.6 shows a pressure trace in castor oil at the geometrical F2: This trace is similar to that obtained by Coleman *et al.* (1991). Finney *et al.* (1991) also measured shock waves in castor oil; however, their pressure traces showed two peaks of almost equal magnitude. Castor oil has a viscosity almost 3 orders of magnitude higher than water with a similar acoustic impedance, and as a result, the rise time increases to about 100 ns. With the increase in shock thickness, peak positive and negative pressures attenuate 8 % and 21 %, respectively: The mean peak positive and negative pressures in water are about 18 MPa and 2.5 MPa, respectively, Figure 4.4, whereas the peak positive and negative pressures in castor oil are about 16.5 MPa and 2.2 MPa, respectively. Castor oil has a cavitation threshold lower than tensions induced by diffracted expansion waves in this series of experiments. One possibility for this is that castor oil has significantly
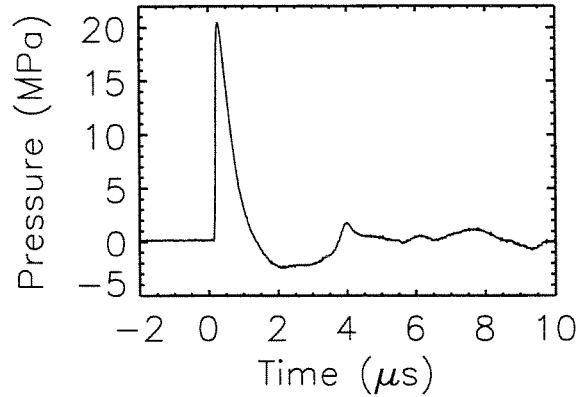
Figure 4.5: Pressure at the geometrical F2 in ethylene glycol; rise time 60 ns.

less nuclei than the other liquids.

Figure 4.7 shows a pressure trace in glycerine at the geometrical F2. It displays a maximum pressure of 16 MPa and a minimum pressure of 2.8 MPa, with a rise time of 100 ns—similar to that in castor oil. There are compression waves that precede the main front at F2, Figure 4.7, resulting from the sound speed discontinuity at the water—glycerine interface. As the shock wave travels from water to glycerine, it refracts. Snells Law is :

$$\frac{\sin\theta_w}{a_w} = \frac{\sin\theta_g}{a_g}, \tag{4.7}$$

where $\theta_w$, $\theta_g$, $a_w$ and $a_g$ are the initial and transmitted angles of the shock front normals, and speed of sound in water and glycerine, respectively. Since $a_g > a_w$, then $\theta_g > \theta_w$; this acts to focus the shock wave. Precursor waves seen in Figure 4.7 are diffracted compression waves, and cross at a new location about 1 cm below F2. The diffracted expansion waves cross about 2.5 cm below F2, with the mean peak pressure occurring 2 cm below F2, indicating that the focal region has been shifted down, Figure 4.8. Figures 4.9 and 4.10 show the linear case of focusing in water and with a water–glycerine boundary. Figure 4.10 shows that the focal point is not only shifted down by about 2.5 cm, but caustics form as well—crossed rays. Table
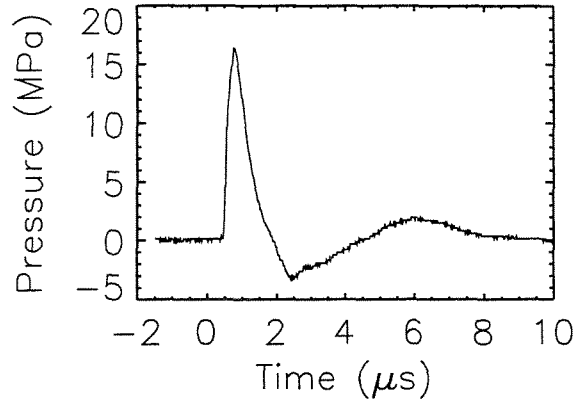
Figure 4.6: Pressure at the geometrical F2 in castor oil; rise time 100 ns.

4.1 gives a summary of all the peak positive and negative pressures, rise times, half widths and total widths for shock waves in all of the liquids discussed.

## 4.3 Pressure Measurements In Random Media

In order to simulate the effect of inhomogeneities on shock focusing, micro–spheres were dispersed in all the liquids except water. This diameter distribution of these beads are as follows: 62-100 $\mu$m(51%), 44-62 $\mu$m (23%) and < 44 (12%). These micro–spheres were hollow with glass walls 1.2 microns thick, and a true density of 238 $\frac{kg}{m^3}$; this makes them buoyant in all of the liquids studied in this work. However, the viscosity of ethylene glycol, castor oil and glycerine retard their rise to the surface. The objective of this study was to obtain a qualitative understanding of focusing and defocusing in tissue due to microscopic inhomogeneities. It should be mentioned that the terms 'micro–sphere', 'sphere' and 'bead' will be used interchangeably.

Four concentrations of glycerine and beads—10, 40, 160 and 1600 beads/$\mu$l—two concentrations of castor oil and beads—40 and 160 beads/$\mu$l—and one concentration of ethylene glycol and beads, 10 beads/$\mu$l, were used. The mean bead separation for 10, 40, 160 and 1600 beads/$\mu$l is 0.46, 0.29, .18 and .09 mm, respectively.

Figure 4.11 shows a schematic of the linear focusing process into a glycerine and
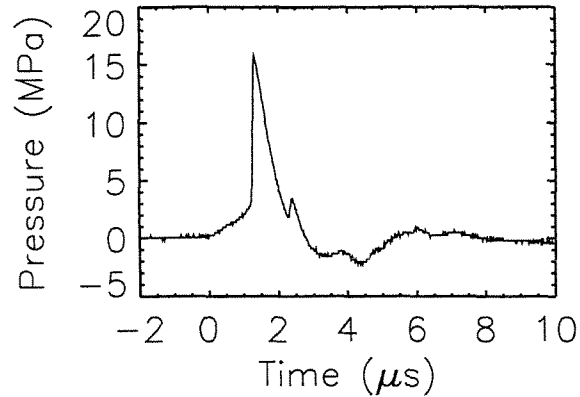
Figure 4.7: Pressure at the geometrical F2 in glycerine; rise time 100 ns.

bead concentration of 40 beads/$\mu$l. The refraction is determined by the volume ratio of glycerine to beads (actually air); this value was determined to be 0.1% for 40 beads/$\mu$l. To account for the refraction induced by the beads, a layer of air was introduced between the glycerine and water interface which is 0.1% of the propagation length in glycerine. The rays travel from water into air and then into glycerine. The focal point has shifted towards the geometrical F2 by 7 mm, comparing Figures 4.10 and 4.11. The beads act to defocus the wave, but their primary effect is to scatter the wave by refraction designated by dashed lines in Figure 4.11.

Figure 4.12 shows a summary of pressure traces taken at the geometrical F2, displaying how the shock structure was altered by the above mentioned concentrations. The first row shows an attenuation of amplitude, as well as an increase in rise time, of shock fronts for an increase in viscosity. It also shows that even though F2 is shifted down for glycerine and ethylene glycol, glycerine has a peak pressure equal to castor oil, and ethylene glycol has a peak pressure equal to water. As the inhomogeneity is increased, the shock front is modified: Inhomogeneity causes severe scattering which forms multiple fronts; rise times are increased which correspond to a thicker shock wave. There is a distinct difference between the scattering effect in glycerine and ethylene glycol mixtures, and the castor oil mixture. Attenuation is not as severe in castor oil (48.5%) as it is in ethylene glycol (88.5%) and glycerine (89.4%), comparing
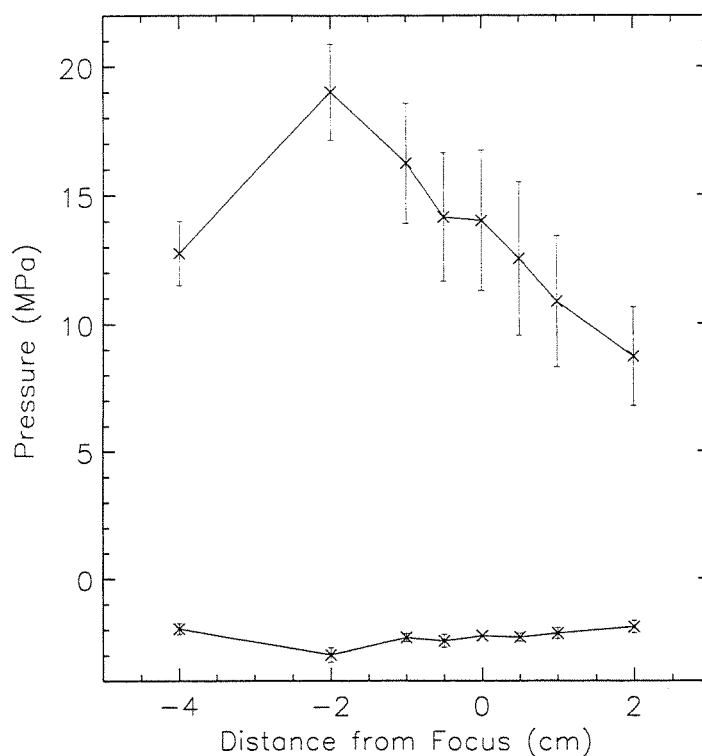
Figure 4.8: Pressure along the axis of focus in glycerine.

0 and 40 beads/$\mu$l, Figure 4.12. Also, multiple fronts do not form as readily in castor oil (2 fronts) as in ethylene glycol (3 fronts) and glycerine (3 fronts), comparing the half-width of the traces at 40 beads/$\mu$l. Table 4.1 gives a summary of all the peak positive and negative pressures, rise times, half widths and total widths for shock waves in all of the concentrations discussed.

To address the repeatability of the wave forms in Figure 4.12, consider the case of glycerine and beads at a concentration of 40 beads/$\mu$l. Six consecutive traces at this condition are shown in Figure 4.13. Notice that the double peak at the maximum amplitude is repeatable, although the amplitude is not—it ranges from about 1.5 to 2.3 MPa. If the last five pressure traces are time shifted by -0.2 $\mu$s, and all of the waves averaged, Figure 4.14 is obtained. The precursor wave at 1 $\mu$s is smeared because some traces did not show this wave; however, the double peaks are still prominent. The general features of each wave are repeatable at some micro-scale, but the energy tends to fluctuate.
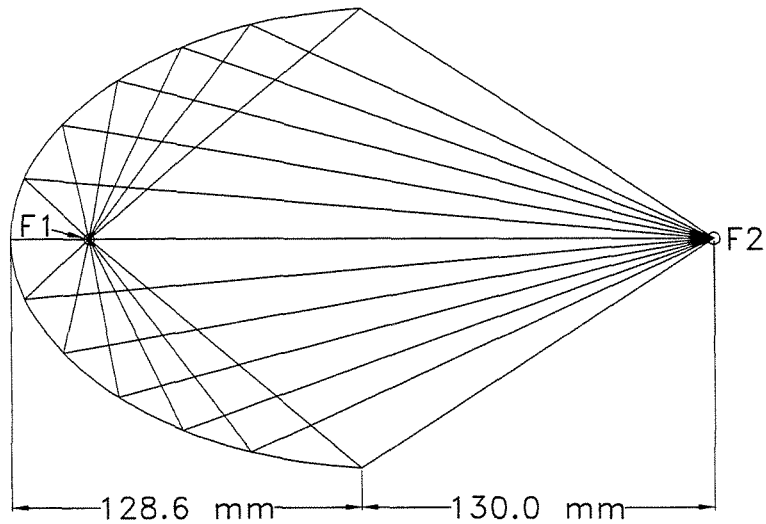
Figure 4.9: Shock wave focusing in water using ray.

## 4.4   Pressure Measurements Behind Tissue

### 4.4.1   Homogeneous Tissue

Muscle tissue was used to alter the shock wave structure. Figure 4.15 shows the linear focusing case in which the wave propagates from water into castor oil and then into muscle tissue. Th focus is shifted down by about 4 mm, but the primary effect of the tissue is to scatter the wave (seen Figure 4.15, dashed lines). Figure 4.16 shows a pressure trace behind a muscle tissue 3.8 cm thick immersed in castor oil. The shock wave does not appear to be wrinkled or folded, although the rise time has increased (400 ns) and amplitude has decreased (6.5 MPa peak positive and 1.75 peak negative pressure). Table 4.1 gives a summary of the wave properties.

### 4.4.2   Non–Homogeneous Tissue

To study the structure of shock waves in the kidney, a more realistic model of the treatment process was instituted. Degassed skin, muscle, fat and kidney tissue—0.1, 1.9, 1.0 and 3.0 cm thick, respectively—were stacked along the focal path in castor oil.
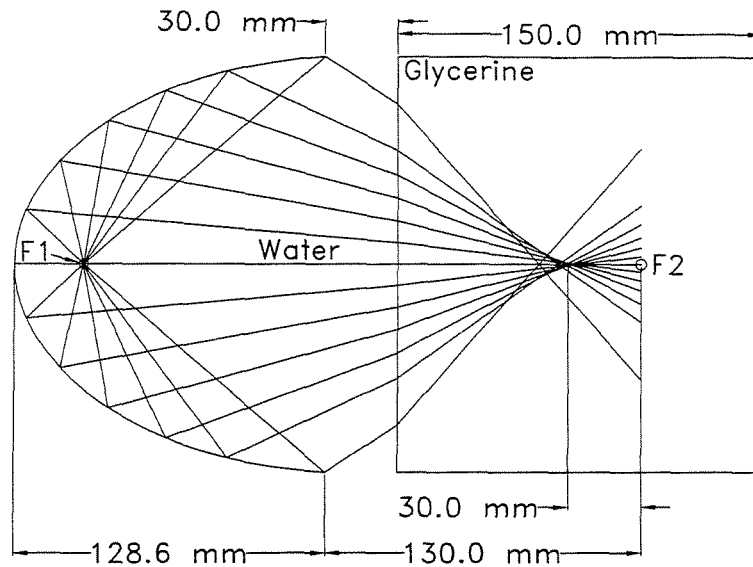
Figure 4.10: Shock wave focusing with a water–glycerine boundary using ray tracing.

Figure 4.17 shows the linear case. The shock wave passes from water into castor oil and through the multi-layered tissue sample. The refraction of the rays depend on the tissue property. In this case the focus is shifted down by about 2 mm; however, the primary effect of the tissue stack is to scatter the wave (see Figure 4.17, dashed lines). This sample altered the shock structure by creating one large fold and increasing the rise time significantly, Figure 4.18. The fold is a result of non-parallel tissue layers, so that refraction at different times causes caustics to form. The peak positive and negative pressures of this shock wave are 4.5 MPa and 1.5 MPa, respectively, with a rise time of 700 ns for the second peak. A summary of wave properties can be seen in Table 4.1. Altered structures of this type were seen in some of the bead concentrations, Figure 4.12.
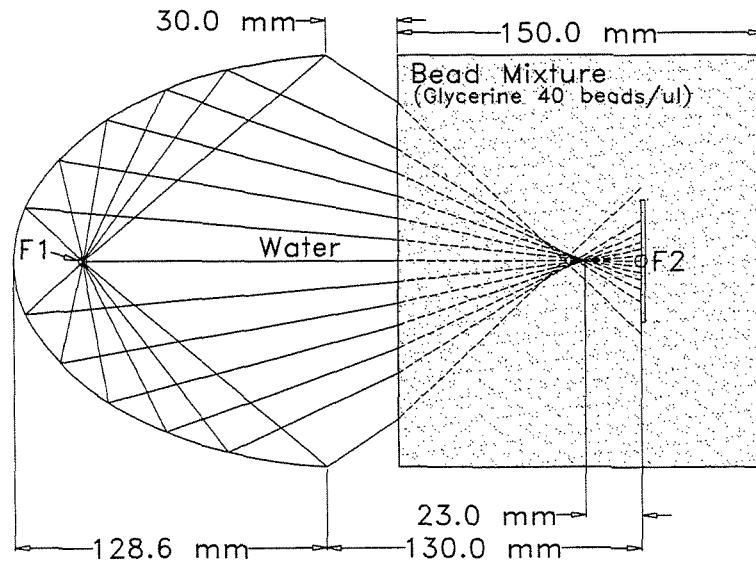
Figure 4.11: Shock wave focusing in glycerine and beads (40 beads/$\mu$l); - - - region of wave scattering.

| Fluid, Mixture or Solid | Concen-tration beads/$\mu$l | P$_+$ Peak MPa | P$_-$ Peak MPa | Rise Time ns | Half Width ns | Total Width ns |
|---|---|---|---|---|---|---|
| Water | N/A | 28.00 | 2.00 | 50 | 1240 | 2520 |
| Castor Oil | N/A | 16.50 | 2.20 | 100 | 1400 | 4100 |
| Castor Oil and Beads | 40 | 8.00 | 1.20 | 150 | 1780 | 3200 |
| Castor Oil and Beads | 160 | 3.90 | 0.50 | 640 | 2440 | 3720 |
| Glycerine | N/A | 16.0 | 2.80 | 100 | 1440 | 4200 |
| Glycerine and Beads | 10 | 3.80 | 0.30 | 236 | 1380 | 2340 |
| Glycerine and Beads | 40 | 1.80 | 0.50 | 960 | 2100 | 3680 |
| Glycerine and Beads | 160 | 0.15 | 0.11 | 144 | 272 | 584 |
| Ethylene Glycol | N/A | 20.00 | 2.50 | 60 | 1140 | 3630 |
| Ethylene Glycol and Beads | 10 | 7.00 | 0.50 | 190 | 2360 | 3160 |
| Ethylene Glycol and Beads | 40 | 2.40 | 0.00 | 460 | 1800 | 3500 |
| Muscle Tissue | N/A | 6.50 | 1.75 | 400 | 1680 | 4040 |
| Stacked Tissue | N/A | 4.50 | 1.50 | 700 | 2220 | 4640 |

Table 4.1: Summary of shock wave characteristics.
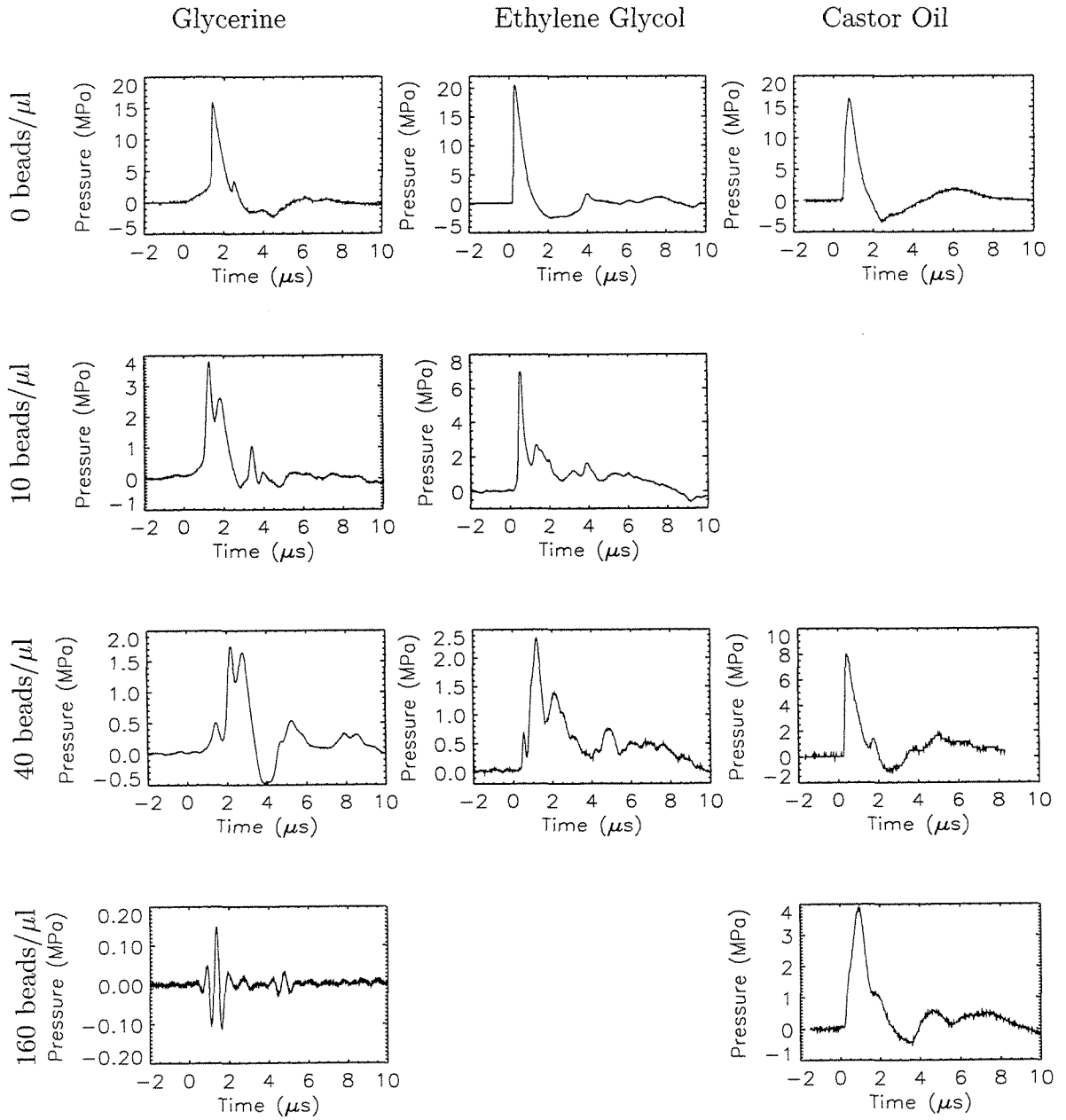
Figure 4.12: Effects of bead concentration on shock waves at the geometrical F2.
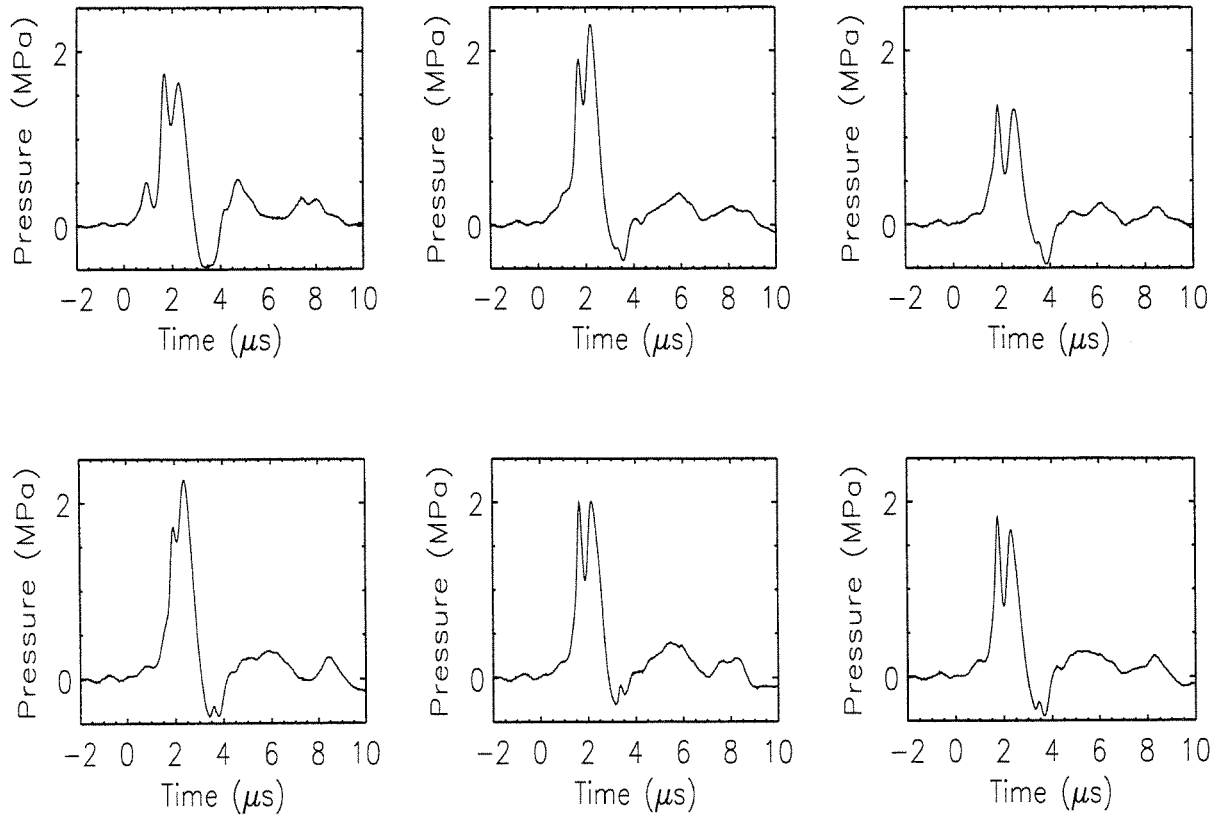
Figure 4.13: Pressure traces in glycerine and beads (40 beads/$\mu$l) at the geometrical F2.
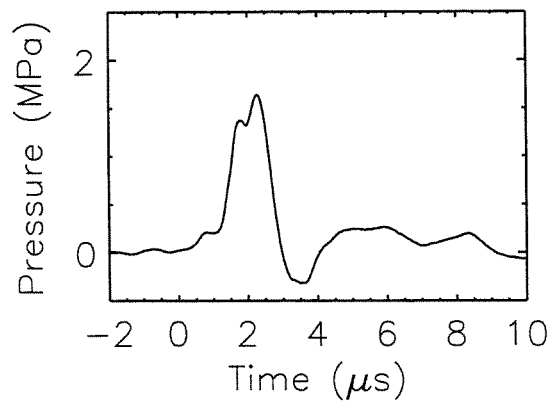


Figure 4.14: Average of pressure traces in Figure 4.13.
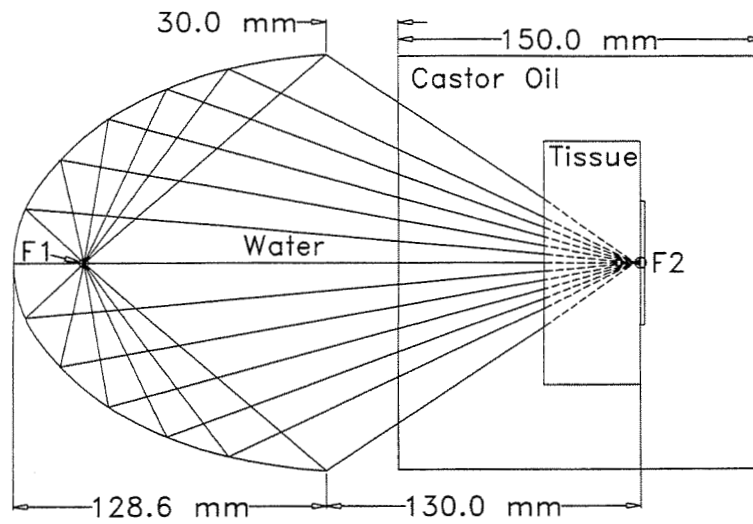
Figure 4.15: Shock wave focusing through homogeneous tissue, 3.8 cm thick; - - - region of wave scattering.
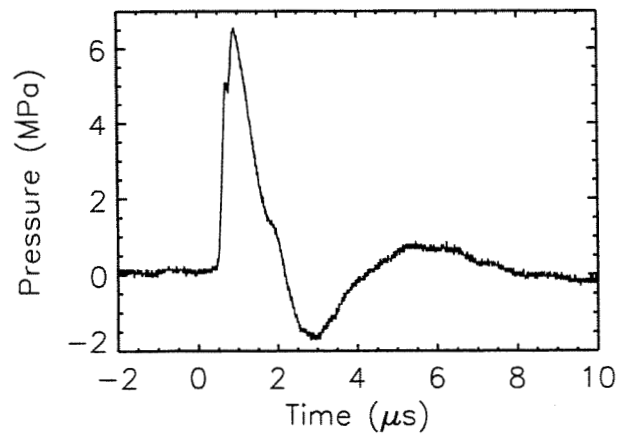


Figure 4.16: Pressure at the geometrical F2 behind 3.8 cm of muscle tissue; rise time 400 ns.
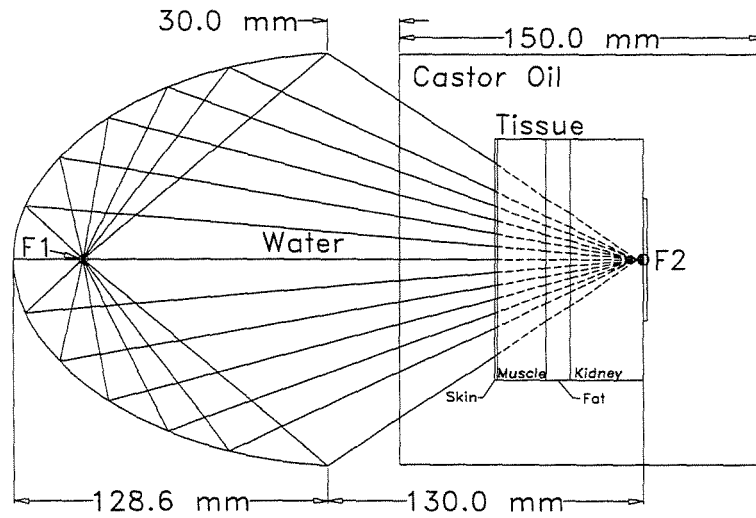
Figure 4.17: Shock wave focusing in stacked tissue, 6.1 cm thick; - - - region of wave scattering.
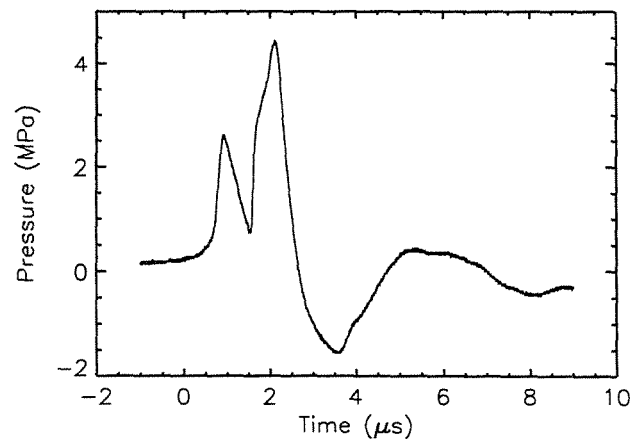


Figure 4.18: Pressure at the geometrical F2 behind stacked tissue 6.1 cm thick; rise time 700 ns.

# Chapter 5   Membrane Tests

Studies were conducted to obtain a qualitative understanding of tissue failure during an ESWL operation. Thin unsupported hydrocarbon membranes were used to simulate a layer of tissue. Because of the method used to make membranes, the exact thickness could not be precisely controlled. When the nitrocellulose was introduced onto the water's surface, the area covered by the membrane depended on the surface tension of the water, which was a variable. Two effects were studied: Damage to simulated tissue induced by cavitation; and damage induced by stress, resulting from inhomogeneities in liquids and tissue layers.

## 5.1   Cavitation Experiments

The high pressure field induced by a focused shock wave is equilibrated by diffracted waves emanating from the aperture of the reflector. In particular, the pressure state behind the diffracted expansion waves is such as to place the fluid in tension. Figure 5.1 shows a plot of negative pressures along the axis of focus.

With sufficient tension, a liquid will be "torn" apart forming a cavity(s) and then vaporized. The minimum radius for this cavity to grow is termed the critical radius:

$$R_{cr} = \frac{2\sigma}{\Delta P} \qquad (5.1)$$

where $\sigma$ represents surface tension, and $\Delta P$ pressure across the cavity interface. Because of decreased liquid pressure , $\Delta P$ becomes larger, so smaller bubbles can grow; this is the driving mechanism for this process. The minimum pressure to cause a cavity to form is known as the tensile strength of the liquid. Theoretical tensile strengths are on the order of hundreds of bars for most liquids; however, observed values are an order of magnitude less. This discrepancy is due to the presence of microscopic
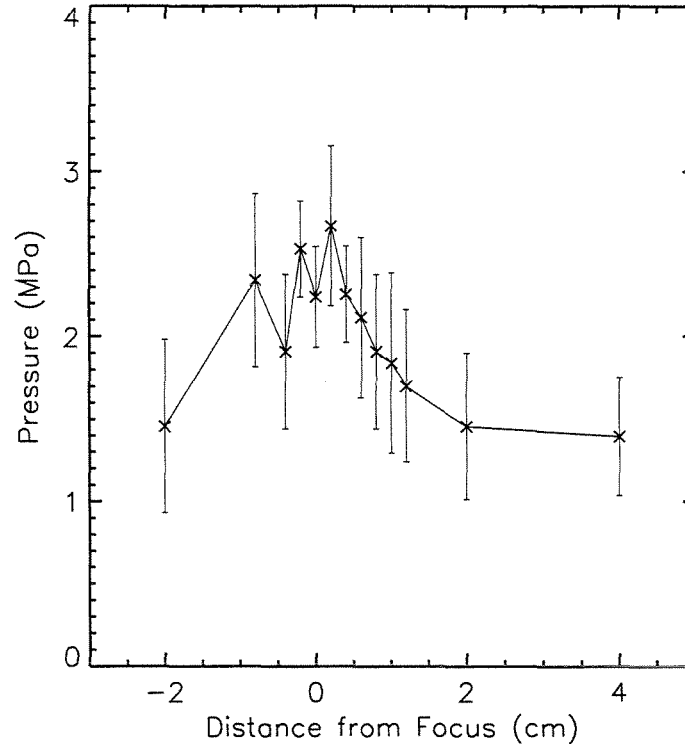
Figure 5.1: Negative pressure in water along the axis of focus.

inhomogeneities.

As the diffracted expansion waves leave the focal region, compression waves follow and establish ambient conditions. This increase in pressure causes cavities to collapse. When a cavity collapses near a solid boundary, a jet is formed which impinges on the solid; this jet causes a shock wave to be transmitted into the solid. Zhong *et al.* (1993a, b) computed pressures in infinite solids resulting from a cavity collapsing in their vicinity, and solved for the shock front in an infinite solid, taking into account the elasticity of the solid.

In the current experiments, these jets impact near or on the boundaries of thin membranes. When the jet impacts the surface of a membrane, instead of a spherical shock wave, the wave is confined to a very thin region: The membrane serves as a wave guide, and the governing system is a wave equation. Stresses in the membrane will be different from an infinite solid. The waves are dispersive with two characteristic

speeds: a group velocity and phase velocity. This merits a more complex solution for the pressure field than the one obtained for an infinite elastic solid.

## 5.2   Tests In Water

Membranes were placed at F2 and subjected to shock waves. Figure 5.2 shows a picture of a membrane that was damaged in water; the size of the hole is about 0.18 cm across. These holes tend to be somewhat circular in shape. This hole is too large to have been caused by a single collapsing cavity, so it is judged to be a result of numerous collapsing cavities in this region. Figure 5.3 shows a membrane with a much smaller hole—0.038 cm across, in the center of the picture—also tested at F2. Hole locations depend on the location of liquid failure in relation to the membrane.

Figure 5.4 plots hole locations for all the membranes tested along the axis of focus. For orientation, the electrode lies at x,y = 0. Most of the cavitation damage occurs within a radius of 0.5 cm of F2. Referring back to Figure 5.1, the mean negative pressure rise is steeper in front of F2 than the drop behind. Membranes were tested in the range of -0.4 cm < F2 < 1.4 cm; it was found that after ten shocks at F2 -0.4 cm and F2 + 1.4 cm, no damage was observed, Figure 5.5. In order to exclude the possibility of a thin membrane, each membrane was moved to F2 and subjected to one shock after which damage was observed. The threshold value for cavitation can not be determined from Figure 5.1, but it is suggested to be higher than 1.2 MPa. Holland *et al.* (1990) experimentally determined the cavitation threshold to be between about 1.1 MPa and 1.4 MPa for distilled water in the frequency range of 0.5 MHz to 3.0 MHz. This relationship is a linear one with a gentle slope.

The damage occurred in the focal region: After the diffracted expansion waves catch the main front and before the diffracted compression waves cross. Each symbol represents the location of a hole in the membrane at a given location. Membranes— except the ones at the extremities where no damage was recorded—were subjected to up to 4 shocks. The extent of the damage region is 1.2 cm.

Figure 5.6 plots the number of holes versus hole diameter. This plot illuminates
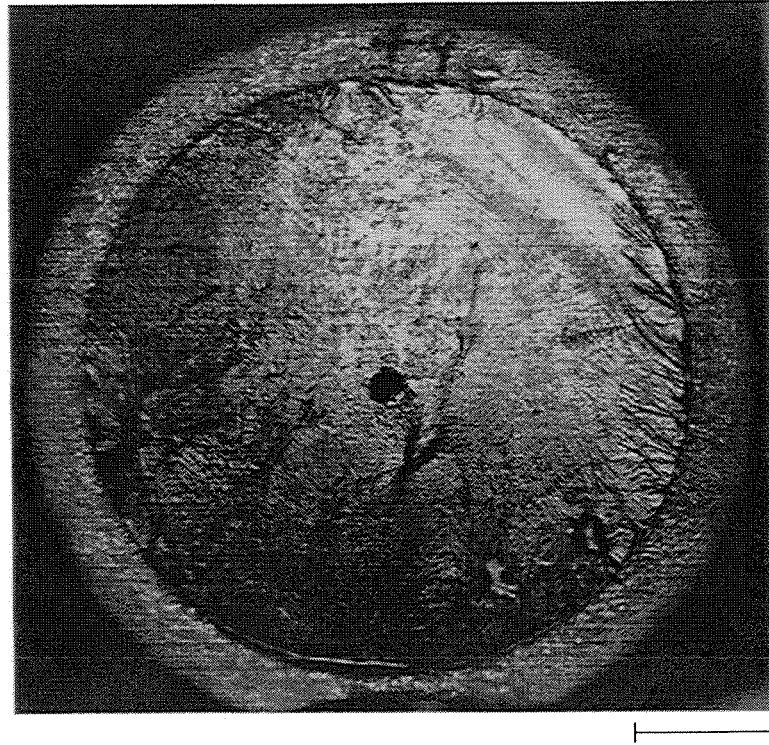
Figure 5.2: Damage at F2 in Water; 1 shock; Membrane ♮49; Scale = 1 cm.
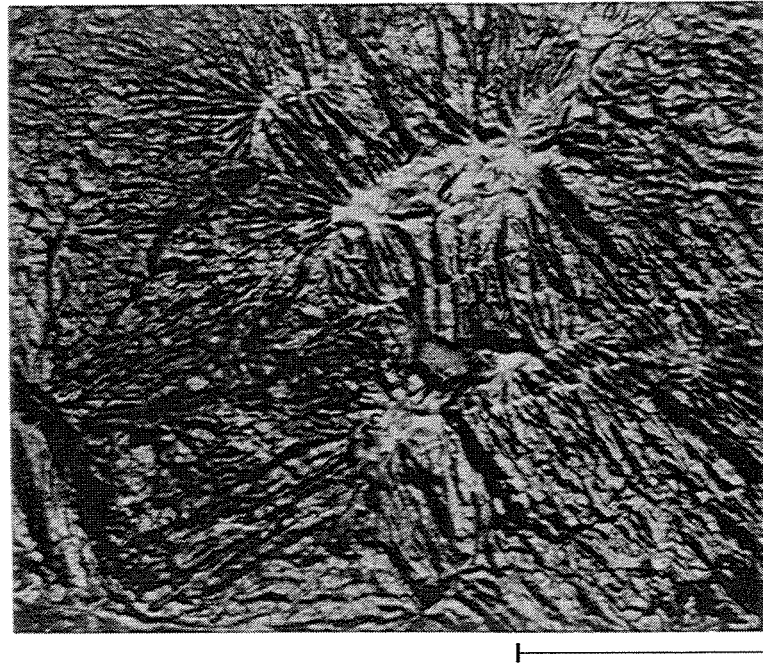


Figure 5.3: Damage at F2 in water; 1 shock; Membrane ♮77; Scale = .25 cm.
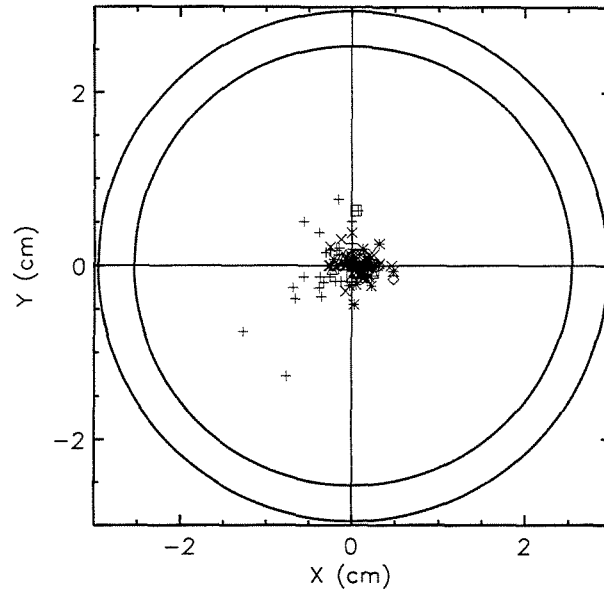
Figure 5.4: Axial cavitation damage in water; 88 membranes and 157 total holes.

two points: 1.) There are a significant number of small holes located very close to the line of focus—center of the membrane—which indicates that cavitation is more intense in this area; and 2.) larger holes result from many smaller holes.

## 5.3   Tests In Other Liquids

Membranes were tested in several other liquids at F2; similar damage was observed, even in liquids with vapor pressure as much as 5 orders of magnitude lower than water (glycerine). In this cases about 20 shocks were required to induce damage. Membranes were subjected to 100 shocks or more in castor oil; the only damage recorded was a few small holes in some membranes at sporadic locations. Since there was no organized pattern to these holes, they are suggested to be caused by impurities or air trapped during testing. The surface tension and vapor pressure of castor oil are unknown. However, it was obvious that the cavitation threshold was not reached, so for the purposes of testing, castor oil was deemed a non–cavitating fluid.
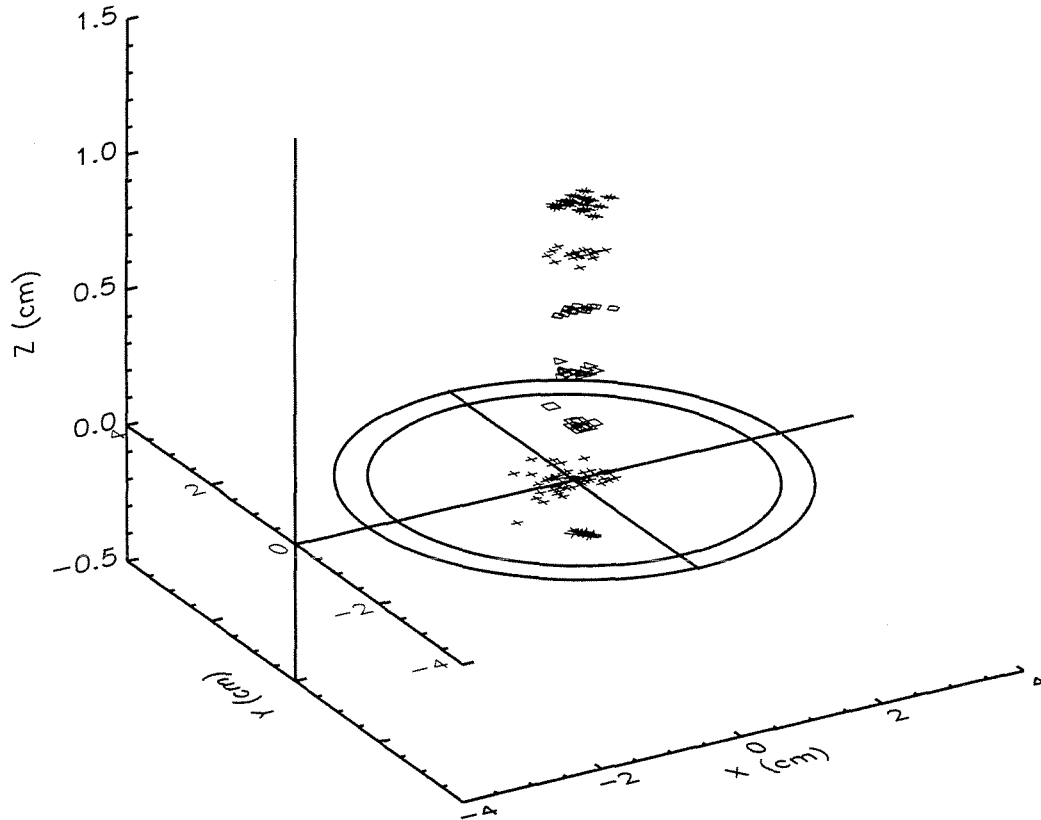
Figure 5.5: Axial cavitation damage in water; 88 membranes and 157 total holes.

## 5.4   Tests In Random Media

### 5.4.1   Membranes Horizontal

Membranes were tested in varying concentrations of micro–spheres in ethylene glycol, glycerine and castor oil. The membranes were oriented such that their normals were coincident with the path of the shock wave. Micro–spheres caused focusing and defocusing of the shock wave which—as will be seen in a later section—decreases the strain rate, making the membranes more susceptible to failure.

Figure 5.7 shows a picture of a membrane that failed in a mixture of castor oil and beads (160 beads/$\mu$l)—this membrane failed after 40 shocks. The failures are tensile
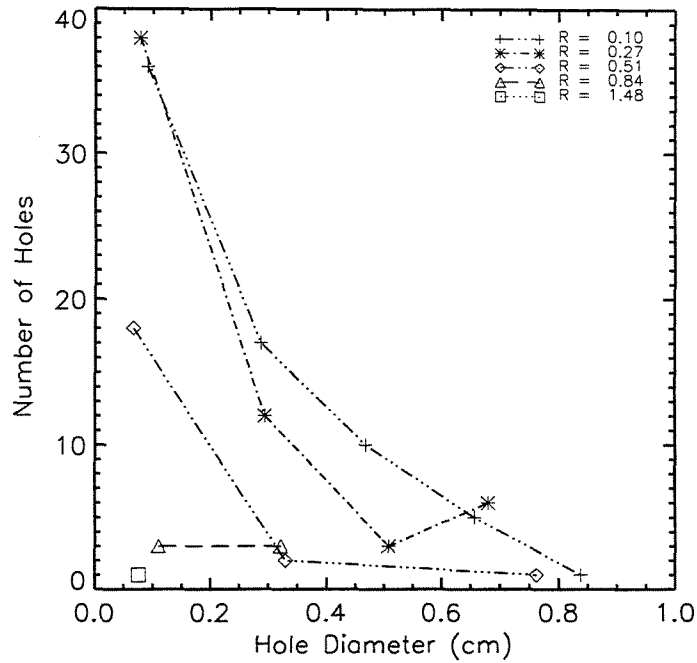
Figure 5.6: Number of holes in relation to the center; 88 membranes and 157 total holes.

and tear at the circumference in most cases, probably because this is a weak area. This implies that connecting tissue are more suspectable to damage. The smaller tears resulted from recent shocks, whereas the larger tears resulted from many shocks— the mixture is not transparent, so it is not possible to observe when a failure is first initiated. It is reemphasized that castor oil does not cavitate in this test environment.

Similar damage was also observed in some concentrations of glycerine and ethylene glycol. One might argue that the damage in these liquids was enhanced by cavitation effects; however, the density of scatterers damp the magnitude of the diffracted expansion waves below their cavitation thresholds. Figure 5.8 shows a picture of a very thick membrane that was subjected to 20 shocks in a mixture of glycerine and beads (40 beads/$\mu$l); no cavitation damage is observed. A tear is developing on the circumference. If this membrane were subjected to say 20 more shocks, or if it were
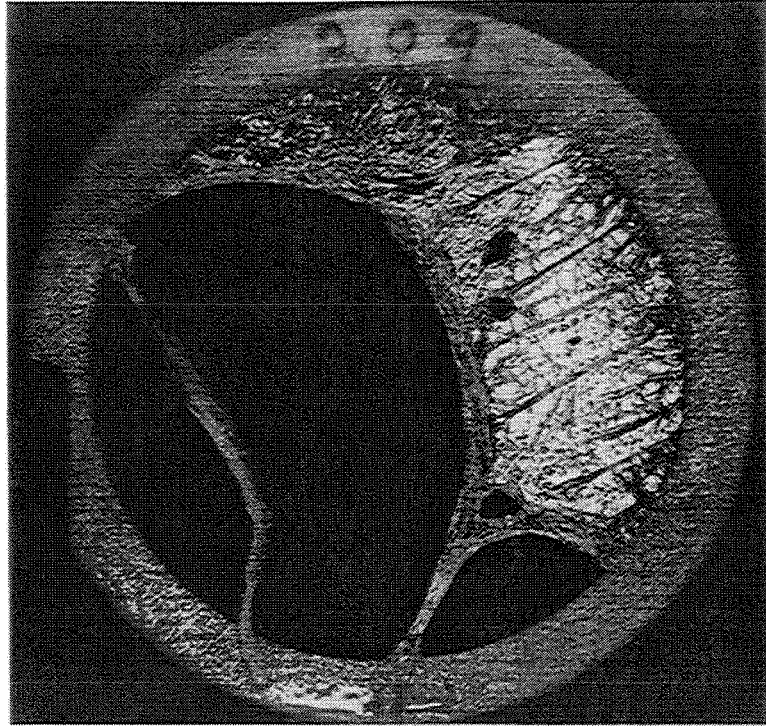
Figure 5.7: Damage at F2 in castor oil and beads (160 beads/$\mu$l); 40 shocks; Membrane $\natural$209; Scale = 1.0 cm.
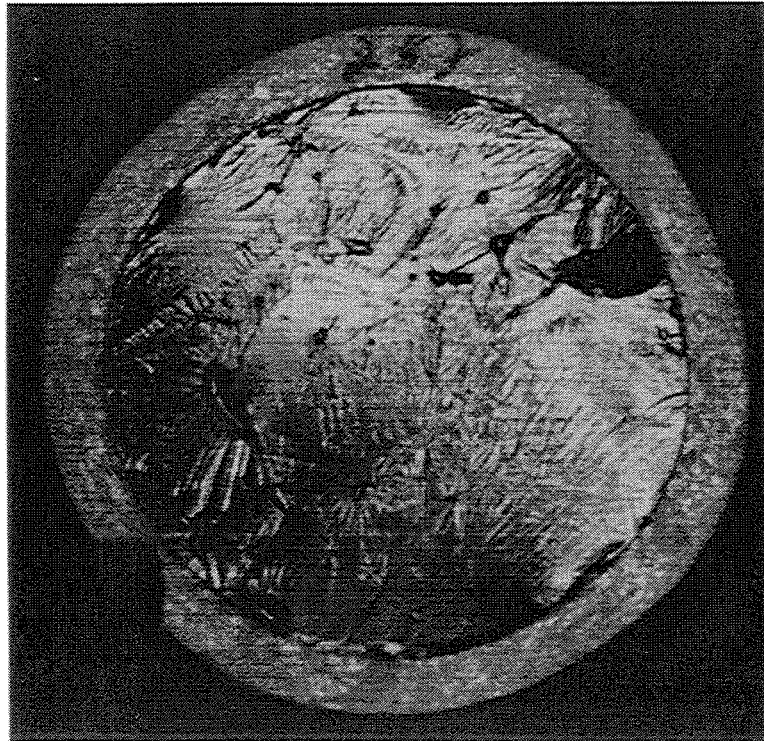


Figure 5.8: Damage at F2 in glycerine and beads (40 beads/$\mu$l); 20 shocks; Membrane $\natural$282; Scale = 1.0 cm.

| Fluid/Mixture | Concentration | Failure | No Failure | Total Tested |
|---|---|---|---|---|
| Castor Oil | N/A | 0 | 9 | 9 |
| Castor Oil and Beads | 160 beads/$\mu$l | 20 | 7 | 27 |
| Castor Oil and Beads | 40 beads/$\mu$l | 0 | 3 | 3 |
| Glycerine | N/A | 4 | 25 | 29 |
| Glycerine and Beads | 1600 beads/$\mu$l | 7 | 8 | 15 |
| Glycerine and Beads | 160 beads/$\mu$l | 27 | 10 | 37 |
| Glycerine and Beads | 40 beads/$\mu$l | 21 | 4 | 25 |
| Glycerine and Beads | 10 beads/$\mu$l | 2 | 8 | 10 |
| Ethylene Glycol | N/A | 0 | 3 | 3 |
| Ethylene Glycol and Beads | 10 beads/$\mu$l | 4 | 1 | 5 |

Table 5.1: Summary of tests.

thinner, the tear would have continued to grow.

Table 5.1 lists a summary of tests conducted in various liquids and mixtures. Depending on the thickness of the membrane, some fail in pure liquid. In a given batch of membranes, an array of thicknesses are present. This uncontrolled factor is accounted for in Table 5.1 by listing both the number of membranes that failed, and those that did not fail for each test. Figure 5.9 shows a plot of the ratio of failed to non–failed membranes versus concentration for mixtures of glycerine and beads. This attempts to eliminate the question of variability both in the membranes and in the lithotripter. At a concentration of 40 beads/$\mu$l, the curve peaks; the arrow pointing to the vertical axis indicates the ratio at zero concentration. This figure implies that there is an optimum concentration of liquid and beads to induce damage with a minimum number of shock waves.

Figure 5.10 shows a plot of the mean number of shocks, along with the standard deviation, to cause membrane failure versus concentration for all liquids tested. The minimum number of shocks to damage a membrane in glycerine and beads (22) occurred at 40 beads/$\mu$l, the same concentration which results in the highest ratio of failed to non-failed membranes. Membranes tested in castor oil and beads (160 beads/$\mu$l) fail after about 30 shocks, as compared to 40 shocks in ethylene glycol and beads(10 beads/$\mu$l). Concentrations outside of the respective ranges plotted, Figure 5.10, do not alter the shock structure such to induce damage.
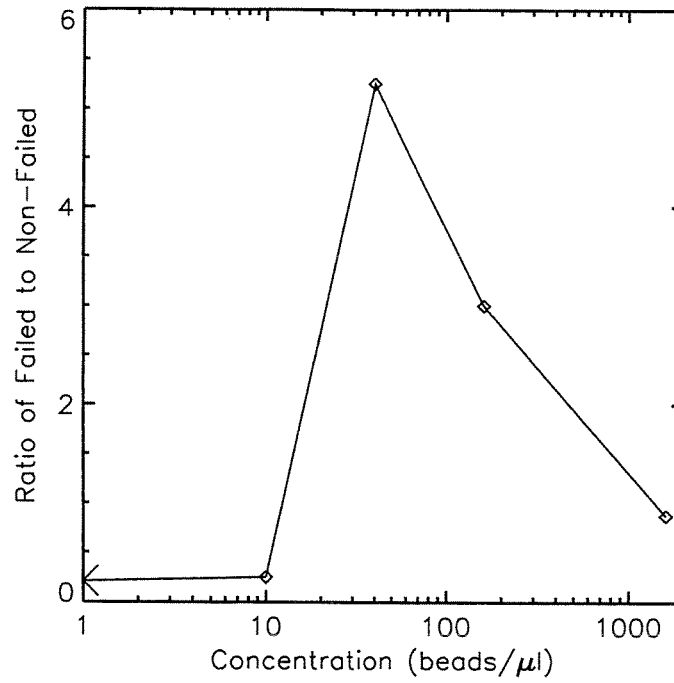
Figure 5.9: Ratio of failed to non–failed membranes in glycerine and beads.
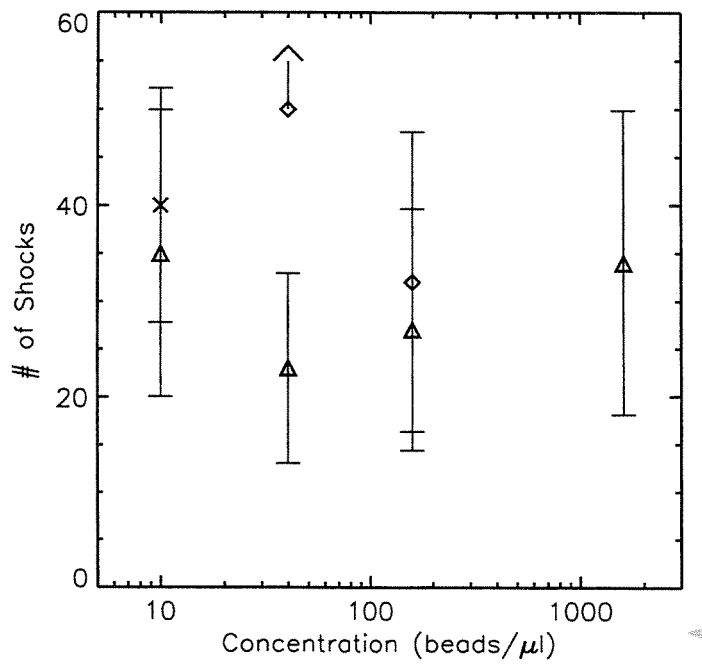


Figure 5.10: Number of shock waves to failure; $\triangle$–Glycerine, $\diamond$–Castor Oil and X–Ethylene Glycol.

To allay the possibility that the aforementioned damage was caused by shock waves accelerating micro–spheres into membranes, tests were conducted with isolated membranes. The membranes were placed in zip-loc bags with a layer of about 0.1 mm thick homogeneous test liquid separating the membrane surface from the bead mixture. Six out of the eight membranes tested in glycerine and beads (40 beads/$\mu$l), and three out of the four tested in castor oil and beads (160 beads/$\mu$l) failed as a result of tearing.

### 5.4.2   Membranes Vertical

Membranes were tested in a concentration of castor oil and beads at F2; they were turned vertically so that they were parallel to the axis of propagation. The center of the membranes were located at F2. Damage was observed both above and below F2, to the extremities of the membranes ($\pm$ 2.1 cm), and was similar to the horizontal tests. These tests demonstrate the longitudinal extent of damage.

## 5.5   Tests Behind Tissue

### 5.5.1   Homogeneous Tissue

Membranes were tested in both water and castor oil behind a muscle tissue sample 3.8 cm thick. The liquids and samples were degassed for two hours before tests were conducted. Damage was observed in water after one shock; it was the classical holes due to cavitation observed in previous tests. Some membranes were subjected to as many as 60 shocks after which catastrophic damage was observed.

In castor oil another mode of damage was identified: In addition to entrained bubbles puncturing the membranes, small tears were observed. Figure 5.11 shows a picture of a membrane after 100 shocks displaying both modes of damage: The long tear on the right (arrow) is due to stress, and the other circular holes to the left are due to collapsing bubbles. All three of the membranes tested exhibited this type of damage.

## 5.5.2 Non–Homogeneous Tissue

Membranes were tested behind tissue stacks used in the pressure tests: Skin, muscle, fat and kidney tissue—.1, 1.9, 1.0 and 3.0 cm thick, respectively. This sample was also degassed in castor oil for two hours. Significant damage was observed after 100 shocks in castor oil, and in some cases catastrophic failure was observed. Figure 5.12 shows a picture of such damage after 100 shocks. The membrane failed at the circumference in two places and tore form the two respective locations. Out of the six membranes tested, three were to the extent shown in Figure 5.12; two received small multiple tears on the circumference; and the last suffered small tears on the interior surface. This damage is similar to that observed with some concentrations of liquids and beads.

# 5.6   Analysis of Membrane Tearing

In the previous section membranes were shown to fail as a result of altered shock waves. In order to investigate the critical parameter(s) of the shock wave that induces damage, consider a very simplistic model of a thin circular membrane subjected to a static triangular load that is a maximum at r = 0 and tapers linearly to 40 % at r = a, with a clamped circumference. This is one extreme of the problem—the steady state solution. Because the problem is dynamic, in order to evaluate the actual stress, strain and displacement fields of the membrane, a dynamical analysis must be done in order to account for the transient response. This response may cause the membrane to have as much as twice the deflection of the steady state solution. In order to determine the deflection of the membrane in the transient, the following convolution must be solved:

$$w(t) = \int_0^t f(\xi)h(t - \xi)d\xi \tag{5.2}$$

where $f(\xi)$ and $h(t - \xi)$ are the impulsive force and response of the membrane. The force as a function of time is known, but the response of the membrane in this highly

damped environment is not. So as a first estimate, the steady state case will be considered.

Timoshenko (1940) solved this problem for large deflections. Equations for displacements in the axial and radial directions can be seen in the following form:

$$w = w_0 \left[ .74 - 1.57 \left( \frac{r}{a} \right)^2 + \left( \frac{r}{a} \right)^4 - .17 \left( \frac{r}{a} \right)^5 \right]$$

(5.3)

$$u = r(a - r)(C_1 + C_2 r + \ldots)$$

(5.4)

where $w_0$, $a$, $C_1$ and $C_2$ represent the displacement at $r = 0$, radius of the membrane and constants. The strain energy of bending and stretching of the membrane are

$$V = \frac{D}{2} \int_0^{2\pi} \int_0^a \left[ \left( \frac{\partial^2 w}{\partial r^2} \right)^2 + \frac{1}{r^2} \left( \frac{\partial w}{\partial r} \right)^2 + \frac{2\nu}{r} \frac{\partial w}{\partial r} \frac{\partial^2 w}{\partial r^2} \right] r \, dr \, d\theta = 5.27\pi \frac{w_0^2 D}{a^2}$$

(5.5)

$$V_1 = \frac{\pi E h}{1 - \nu^2} \int_0^a \left( \epsilon_r^2 + \epsilon_t^2 + 2\nu \epsilon_r \epsilon_t \right) r \, dr$$

(5.6)

where E represent the modulus of elasticity, and D, $\epsilon_r$ and $\epsilon_t$ are the flexural rigidity, radial strain and tangential strain having the following forms:

$$D = \frac{E h^3}{12 \left( 1 - \nu^2 \right)}$$

(5.7)

$$\epsilon_{rr} = \frac{du}{dr} + \frac{1}{2} \left[ \left( \frac{du}{dr} \right)^2 + \left( \frac{du}{dr} \right)^2 \right]$$

(5.8)

$$\epsilon_t = \frac{u}{r}$$

(5.9)

with h representing the thickness of the membrane. $C_1$ and $C_2$ are determined from Equation 5.6 by enforcing that the total energy of the plate be a minimum for any

position.

$$C_1 = 1.185 \frac{w_0^2}{a^3} \tag{5.10}$$

$$C_2 = -1.74 \frac{w_0^2}{a^4} \tag{5.11}$$

Adding the stretching ($V_1 = 2.59\pi \frac{w_0{}^4 D}{a^2 h^2}$) and bending energies gives an equation for $w_0$,

$$w_0 = \frac{pa^4}{44D} \frac{1}{1 + 0.98 \frac{w_0^2}{h^2}} \tag{5.12}$$

where p represent the pressure at r = 0. The equation for radial stress takes the form

$$\sigma_{rr} = \frac{E}{1 - \nu^2} \left[ \frac{du}{dr} + \frac{1}{2} \left( \frac{dw}{dr} \right)^2 + \nu \frac{u}{r} \right]. \tag{5.13}$$

Using the displacements, Equations 5.3 and 5.4, and Equations 5.8 and 5.13, the radial stress can be obtained,

$$\sigma_{rr} = \frac{E}{1-\nu^2} [g_0 + g_1 \left( \frac{r}{a} \right) + g_2 \left( \frac{r}{a} \right)^2 + g_3 \left( \frac{r}{a} \right)^3 + g_4 \left( \frac{r}{a} \right)^4$$
$$+ g_5 \left( \frac{r}{a} \right)^5 + g_6 \left( \frac{r}{a} \right)^6 + g_7 \left( \frac{r}{a} \right)^7 + g_8 \left( \frac{r}{a} \right)^8 ] \tag{5.14}$$

where the $g_i$s are given by the following equations:

$g_0 = (\nu + 1) aC_1$, $g_1 = (\nu + 2)(aC_2 - C_1)$, $g_2 = -(\nu + 3)C_2 + 4.95 \frac{w_0{}^2}{a^4}$, $g_3 = 0$,

$g_4 = -12.59 \frac{w_0{}^2}{a^6}$, $g_5 = 2.69 \frac{w_0{}^2}{a^7}$, $g_6 = 8 \frac{w_0{}^2}{a^8}$, $g_7 = -3.41 \frac{w_0{}^2}{a^9}$ and $g_8 = .364 \frac{w_0{}^2}{a^{10}}$.

The radial strain is given by

$$\epsilon_{rr} = [h_0 + h_1 \left( \frac{r}{a} \right) + h_2 \left( \frac{r}{a} \right)^2 + h_3 \left( \frac{r}{a} \right)^3 + h_4 \left( \frac{r}{a} \right)^4$$
$$+ h_5 \left( \frac{r}{a} \right)^5 + h_6 \left( \frac{r}{a} \right)^6 + h_7 \left( \frac{r}{a} \right)^7 + h_8 \left( \frac{r}{a} \right)^8 ] \tag{5.15}$$

where the $h_i$s are given by the following equations:

$$h_0 = aC_1 \left(1 + \tfrac{aC_1}{2}\right), \quad h_1 = 2C_1 + 2aC_2 + 2C_1a\left(aC_2 - C_1\right),$$

$$h_2 = 4.95w_0^2 + 3C_2 + 2a^2C_2^2 - 7C_1C_2 + 2C_1^2, \quad h_3 = -6\left(aC_2 - C_1\right)C_2,$$

$$h_4 = 4.5C_2^2 - 12.59\tfrac{w_0^2}{a^6}, \quad h_5 = 2.69\tfrac{w_0^2}{a^7}, \quad h_6 = 8\tfrac{w_0^2}{a^8}, \quad h_7 = -3.41\tfrac{w_0^2}{a^9} \text{ and } h_8 = .364\tfrac{w_0^2}{a^{10}}.$$

Equation 5.12 was solved to determine the displacements at $r = 0$. The peak pressures in Table 4.1 were used to compute deflections for water, castor oil, glycerine and tissue. These deflections were used in Equations 5.14 and 5.15 to determine the radial stresses and strains. To conceptualize this problem in a dynamic sense, a strain rate was defined as follows:

$$\dot{\epsilon} = \frac{\epsilon_{rr}}{t_{rise}} \tag{5.16}$$

where $t_{rise}$ is the rise time of the shock wave.

To test the static radial failure stress of membranes used in the experiments, a point load was applied to wet and dry membranes, and deflections were measured at $r = 0$. Radial stresses were approximated with the following equation (Timoshenko 1940):

$$\sigma_{rr} = \alpha_r E \frac{w_0^2}{a^2} \tag{5.17}$$

where $\alpha_r = .976$ for a clamped circular plate. Equation 5.17 was determined in a similar fashion as Equation 5.14, by using strain energy arguments. Dry membranes were seen to fail at a radial stress of 129 MPa, while thoroughly soaked membranes in glycerine and castor oil (24 hours) were observed to fail at a radial stress 140 MPa and 105 MPa, respectively.

Figure 5.13 shows a plot of $\sigma_{rr}$ at $r = 0$ versus $\dot{\epsilon}$. The horizontal solid line indicates the static failure stress, 110 MPa, as given by Hercules Inc. (1995). The vertical dashed line represents a failure boundary. The criteria for this boundary is that tearing was observed in membranes tested in each configuration on or to the left of the boundary (Zone B), while no membranes were observed to fail as a result

of this mode to the right of this boundary (Zone A). In fact cavitation damage is observed in membranes tested in water and glycerine with the same respective radial stresses; however, if these liquids did not cavitate in this environment, no damage would be observed, as is the case with castor oil. $*$, $\triangle$, $\diamond$ and $\square$ represent water, glycerine, castor oil and tissue. Glycerine and castor oil range from the pure state to their respective mixtures (see Table 5.1), and the two tissue samples are muscle and stacked tissue. The mnemonics close to each symbol represent the respective configuration and number of shock waves to failure.

The membrane support such unusually high stresses because the load is dynamic. $\sigma_{rr}$ decreases with decreasing $\dot{\epsilon}$; however, so does the failure stress. As $\dot{\epsilon}$ goes to zero the static tensile strength is obtained. To the left of the failure boundary damage was usually observed. Membranes tested in environments close to the boundary do not damage as readily as membranes far away. The $\diamond$ to the right and closest to the failure boundary represent castor and beads, 40 beads/$\mu$l; no damage was observed with this concentration. The $\triangle$ on the failure boundary represents a glycerine concentration of 10 beads/$\mu$l; few damaged membranes were observed with this concentration. The $\square$ closest to the failure boundary represent muscle tissue; only minor if any damage was observed with this configuration. A decrease in $\dot{\epsilon}$ from this point has a significant effect on the membranes in these environments. The other symbols farther to the left (in order of decreasing $\dot{\epsilon}$), $\square$, $\diamond$, $\triangle$ and $\triangle$, represent stacked tissue, castor oil and beads (160 beads/$\mu$l) and glycerine and beads (160 and 40 beads/$\mu$l), respectively (see Table 5.1).

Membranes do not fail after one shock wave, in fact it takes many shock waves for damage to be observed. So, the failure is a result of cumulative effects. Miner (1945) suggested that in a fatigue test, damage at a given stress could be considered to accumulate linearly with the number of stress repetitions. Failure occurs when the accumulated damage reached some critical value. Miners law defines an expression for the linear cumulative damage,

$$\sum_{i=1}^{n} \frac{n_i}{N} = 1 \qquad (5.18)$$

where $n_i$ and N represent the number of administered cycles and the number of cycles to failure. For the current experiments an appropriately modified form is

$$\sum_{i=1}^{n} \frac{\sigma_{rri}}{\sigma_{stat}} \frac{t_i}{T_c} = 1 \qquad (5.19)$$

where $\sigma_{rri}$, $\sigma_{stat}$, $t_i$ and $T_c$ represent the radial stress induced by each shock, the static tensile failure strength, rise time of the shock wave and a characteristic time. Summing over all of the tests gives the following equation:

$$n^2 \frac{\overline{\sigma}_{rr}}{\overline{\sigma}_{stat}} \frac{\overline{t}}{T_c} = 1. \qquad (5.20)$$

Hercules' value of the static failure strength will be used for $\overline{\sigma}_{stat}$. Table 5.2 lists characteristic times ($T_c$) for membranes failure in their respective environments. Figure 5.10 plots the number of shocks to failure for each bead mixture. 100 shocks were required for membrane failure behind tissue; however, note that the damage behind the two tissue samples are not to the same extent. The temporal scale is on the order of microseconds because 110 MPa, the static failure stress, was chosen for the normalizing stress. $T_c$ can be thought of as an exposure time: Large $T_c$ indicates resistance to non-cavitation failure.

If the characteristic time is plotted versus the ratio of sound speed of the scattering media to the surrounding fluid, Figure 5.14, it can be seen that there is a linear relationship between the sound speed ratio and characteristic time. For small values of the ratio, the characteristic time is small, but for large values of the ratio, the characteristic time is large. In the case of an ESWL operation, the ratio of tissue to water is about one, and a typical procedure takes 1500 or so shock waves. This implies characteristic times much larger than those seen in these experiments.
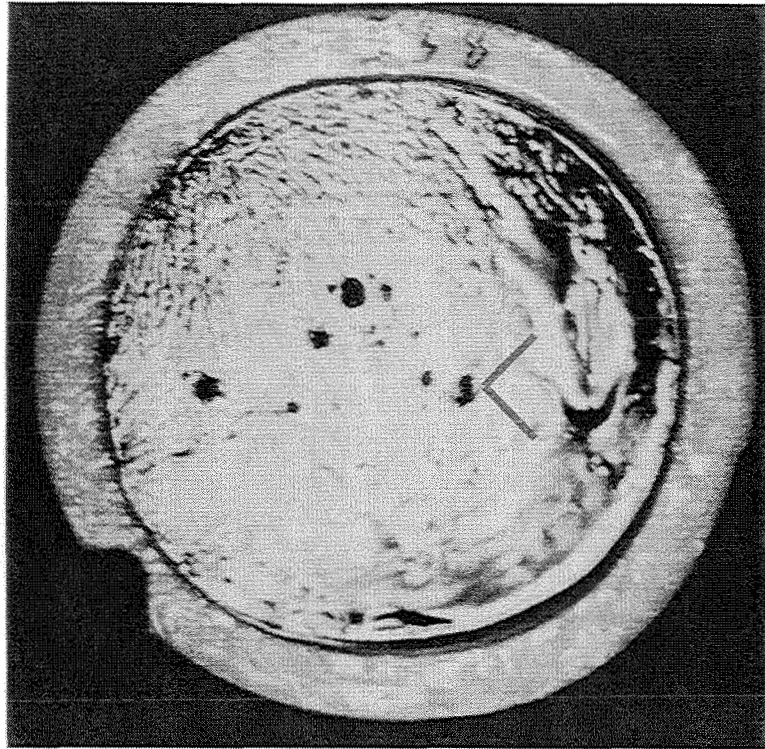
Figure 5.11: Damage at F2 in castor oil behind muscle tissue, 3.8 cm thick; 100 shocks; Membrane ♮338; Scale = 1.0 cm.
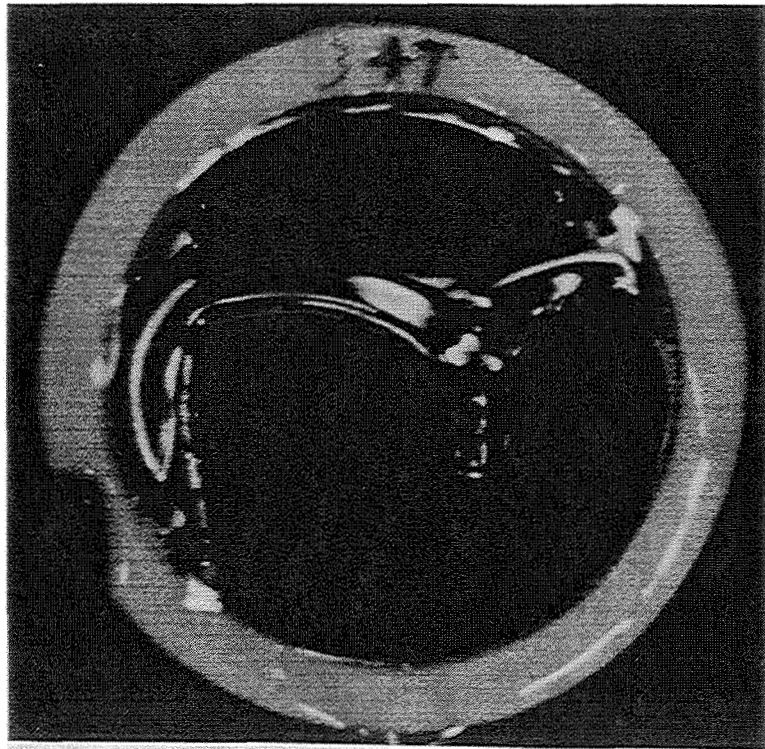


Figure 5.12: Damage at F2 in castor oil behind layered tissue (skin, fat, muscle and kidney), 6.1 cm thick; 100 shocks; Membrane ♮347; Scale = 1.0 cm.
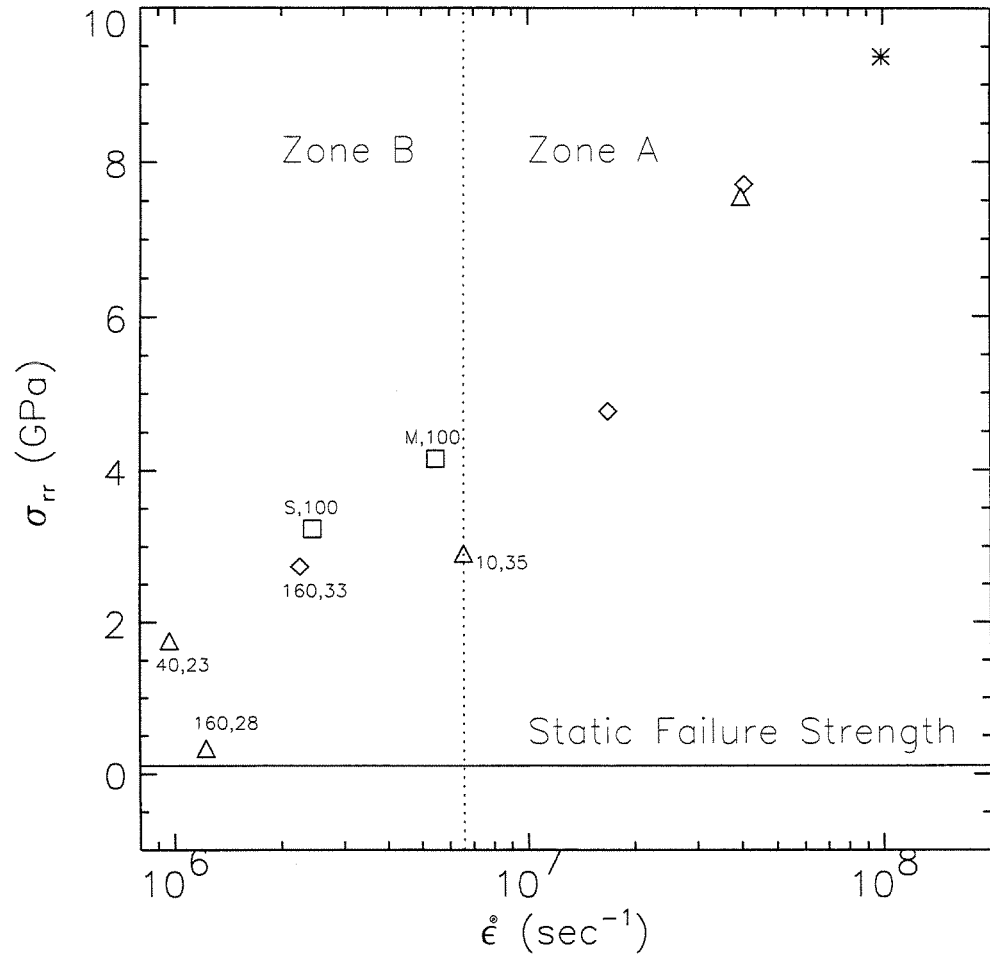
Figure 5.13: Strain rate vs. Radial Stress; — Static Failure Strength, * Water, △ Glycerine, ◇ Castor Oil, and □ Tissue; | Failure Boundary.

| Fluid, Mixture or Solid | Concentration beads/$\mu$l | Shocks to Failure | $\sigma_{\rm rr}$ GPa | Rise Time ns | Strain Rate ($\times 10^{-6}$) s$^{-1}$ | Characteristic Time (T$_{\rm c}$) $\mu$s |
|---|---|---|---|---|---|---|
| Water | N/A | N/A | 9.4 | 50 | 99.0 | N/A |
| Castor Oil | N/A | N/A | 7.7 | 100 | 41.0 | N/A |
| Castor Oil and Beads | 40 | N/A | 4.8 | 150 | 17.0 | N/A |
| Castor Oil and Beads | 160 | 33 | 2.7 | 640 | 2.3 | 17.1 |
| Glycerine | N/A | N/A | 7.6 | 100 | 40.0 | N/A |
| Glycerine and Beads | 10 | 35 | 2.9 | 236 | 6.6 | 7.6 |
| Glycerine and Beads | 40 | 23 | 1.8 | 960 | 1.0 | 8.3 |
| Glycerine and Beads | 160 | 28 | .3 | 144 | 1.2 | .3 |
| Muscle Tissue | N/A | ~100 | 4.2 | 400 | 5.5 | 152.7 |
| Stacked Tissue | N/A | ~100 | 3.2 | 700 | 2.4 | 203.6 |

Table 5.2: Summary of characteristic times.
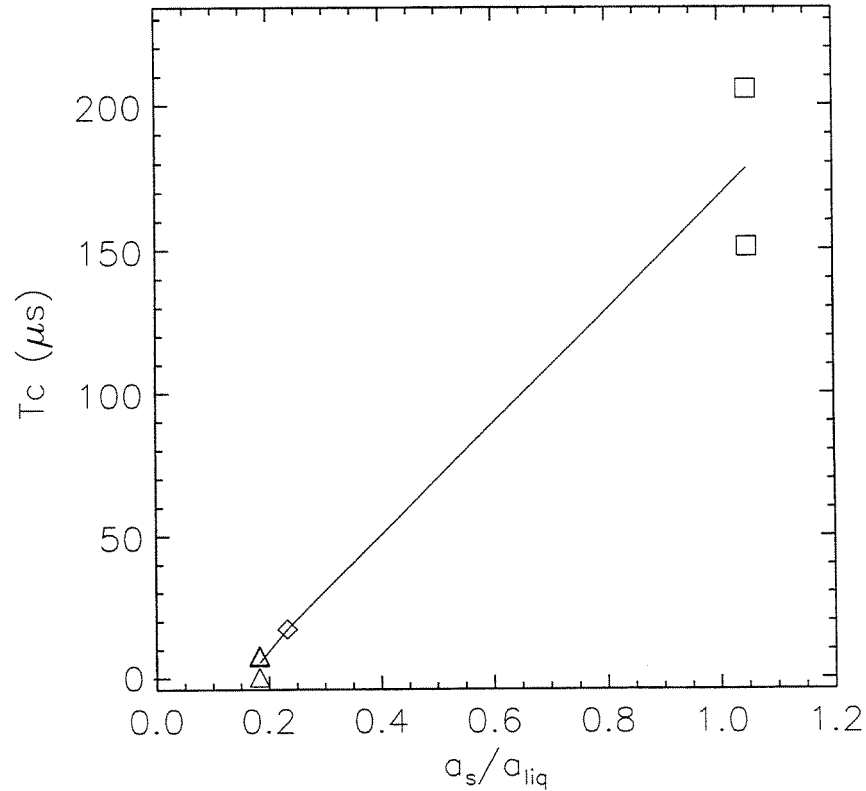


Figure 5.14: Characteristic time to failure for different environments.

# Chapter 6   Conclusions

Tests were conducted in an experimental lithotripter to investigate mechanisms of injury associated with this operation. An analysis was done to explore models of the procedure. Detailed pressure data were collected and analyzed to study the complexity of the shock structure in liquids and behind tissue samples. Two modes of injury were observed unsupported membrane tissue structure.

## 6.1   Pressure Experiments

Pressure measurements were made in different liquids, mixtures and behind tissue samples to analyze the shock wave structure. Measurements were also made in liquids with hollow glass spheres to study how possible non–homogeneities in the body affect the focusing process.

### 6.1.1   Shock Waves In Water

The structure of converging shock waves in water were analyzed. The shock thickness was found to be on the order of 76 nm in water at F2, which disagreed by an order of magnitude with the theoretical value. This discrepancy was caused by the finite thickness of the gauge as well as misalignment. Pressure measurements were made along the axis of focus, and it was determined that the diffracted expansion waves catch the main front 0.4 cm in front of F2 and the diffracted compression waves crossed 1 cm behind F2, making the focal region about 1.4 cm in length. Maximum and minimum peak pressures occurred at about 0.4 cm and 0.25 cm behind F2, respectively.

## 6.1.2 Shock Waves In Other Liquids

Shock waves were explored in other liquids with various viscosities, densities and sound speeds. It was found that an increase in viscosity by an order of magnitude had essentially no effect on the thickness of the shock wave; however, an increase by three orders of magnitude caused the shock thickness to double. In one of the liquids, glycerine, with a speed of sound 20 % higher than water, the shock wave focused 2 cm below F2.

## 6.1.3 Shock Waves In Random Media

The effects of inhomogeneity on shock waves in different liquids were explored. Amplitude attenuation was more severe when inhomogeneities were added to fluids with higher sound speeds. As the inhomogeneity is increased, the shock front is modified: Inhomogeneity causes severe diffraction which forms multiple fronts; rise times are increased which correspond to thicker shock waves. There is a distinct difference between the scattering effect in glycerine and ethylene glycol mixtures, and the castor oil mixture. Multiple fronts do not form as readily and attenuation is not as severe in castor oil as in ethylene glycol and glycerine.

## 6.1.4 Shock Waves In Tissue

Pressure measurements were also made in muscle and stacked tissue (skin, fat, muscle and kidney tissue). It was shown that the muscle tissue did not alter the shock wave structure to the extent of the stacked tissue. The rise time in the stacked tissue was twice that of the muscle tissue.

# 6.2 Membrane Experiments

## 6.2.1 Cavitation Experiments

Studies were conducted to obtain a qualitative understanding of tissue failure due to cavitation damage during an ESWL operation. It was shown that membranes fail when cavities collapse in their vicinity after a few shock waves. Hole size depended on the number of cavities that collapsed near them. The cavitation zone was shown to be -0.4 cm < F2 < 1.4 cm, where the negative pressure was greater than 1.5 MPa. This is also the threshold seen by workers in the field (Holland *et al.* 1990). The damage was shown to be concentrated around the line of focus. It was also shown that the hole diameter increased with an increasing number of small holes. Cavitation damage was shown to exist in liquids with vapor pressures up to 5 orders of magnitude lower than water. The cavitation threshold of castor oil could not be achieved in the lithotripter.

## 6.2.2 Random Media Experiments

Another mode of membrane failure was demonstrated by adding inhomogeneities to various fluids. The concentration of these scatterers were varied in different liquids. This, in some cases, significantly altered the shock wave structure to such an extent as to induce damage in membranes. Damage was recorded photographically. The new failure mode was a tear and not circular as with cavitation damage. Each liquid observed a maximum damage rate and threshold for a given density of scatterers. These mixtures were shown to damage membranes both in the horizontal and vertical positions.

## 6.2.3 Tissue Experiments

Experiments were conducted using muscle tissue and multiple tissue samples as scatterers. Membranes were placed behind these samples at F2. It was shown that the muscle tissue altered the shock wave to cause minor if any damage to membranes

after 100 shocks; however, behind the multiple tissue sample, classical tearing was observed after 100 shocks, which was catastrophic in some cases.

## 6.3   Analysis of Membrane Tearing

It was shown that membranes in lithotripters are subjected to high stresses for short periods of time. However, as the strain rate is decreased—increased exposure time— damage probability increases. In an ESWL operation, shock waves of magnitude 40 MPa or so in water are focused to break kidney stones. If the shock wave attenuates by 28 % by the time it reaches the kidney stone and the rise time increases, tissue damage is inevitable, particularly in light of the accumulated effects over 1500 or more shock waves.

## 6.4   Future Work

Detailed work is needed to quantify important parameters suggested in this thesis. The failure stress of membranes and tissue is needed as a function of strain rate. Also, a better understanding of how cumulative effects induce failure is in order. A more refined model of membrane and tissue failure is necessary which takes into account the transient response of the material. Lastly, correlation between experiments and observed damage in tissue is needed to link the key parameters to observed tissue injury.

# Bibliography

Andreev, S. I. Vanykov, M. P. & Kotolov, A. B. 1962 Growth of the Spark Discharge Canal for a Discharge Circuit with a Rapidly Increasing Current. *Zhurnal Teck. Fiz.*, **32**, 57-62.

Akers, S. R., & Cocks, F. H. 1989 Experimental Laboratory Lithotripter: Design, Construction, and Operation. *Biomed. Instrum. & Technol.*, **January/February**, 50-53.

Bbert, N. M. & Bikales, M. 1972 *Encyclopedia of Polymer Science and Technology.* Interscience Pub., NY.

Blackstock, D. T. 1988 Session OO. Physical Acoustics VI and Bioresponse to Vibration III: Extracorporeal Shock Wave Lithotripsy–Biological Aspects. *J. Acoust. Soc. Am.*, **83**, S88-S89.

Boltz, R. E. & Ture, G. L. 1973 *Handbook of Tables for Applied Engineering Science.* 2nd Ed., CRC Press Inc., OH.

Bourlion, M. Dancer, P. & Lacoste, F. 1994 Design and Characterization of a Shock Wave Generator Using Canalized Electrical Discharge: Application to Lithotripsy. *Rev. Sci. Instrum.*, **65**, 2356-2363.

Boyer, H. E. 1987 *Atlas of Stress–Strain Curves.* ASM International, Metals Park, OH.

Brendel, W., Delius, M. & Goetz, A. 1987 Effect of Shock Waves on the Microvasculature. *Prog. appl. Microcirc.*, **12**, 41-50.

Brennen, Christopher Earls 1995 *Cavitation and Bubble Dynamics.* Oxford University Press, NY.

Burridge, R., Papnicolaou, G. S. & White, B. S. 1988 One–Dimensional Wave Propagation in a Highly Discontinuous Medium, *Wave Motion*, **10**, 19-44.

Cao, L. C., Boevé, E. R., de Bruijn, W. C., Robertson, W. G. & Schröder, F. H. 1993 A Review of New Concepts in Renal Stone Research, *Scanning Microscopy.* **7**, 1049-1065.

Cates, J. E. 1996 Calculation of Focusing of Weak Shocks Using Geometrical Shock Dynamics. Ph.D. Thesis, Graduate Aeronautical Laboratories, California Institute of Technology.

Catherasoo, C. J. 1982 Shock Dynamics in Non–Uniform Media. Ph.D. Thesis, Graduate Aeronautical Laboratories, California Institute of Technology.

Catherasoo, C. J.& Sturtevant, B. 1983 Shock dynamics in non-uniform media. *J. Fluid Mech.*, **127**, 539-539.

Cathignol, D., Mestas, F. Gomez, F. & Lenz, P. 1991 Influence of Water Conductivity on the Efficiency and the Reproducibility of Electrohydraulic Shock Wave Generation. *Ultrasound in Med. & Biol.*, **17**, 819-828.

Chaussy, A., Ch. (Ed.) 1986 *Extracorporeal Shock Wave Lithotripsy, Technical Concept, Experimental Research and Clinical Application.* 2nd, Revised & Enlarged Edition, S. Karger, AG, Basel, Switzerland.

Chester, W. 1954 The quasi–cylindrical shock tube, *Phil. Mag.*, **45**, 1293-101.

Chisnell, R. F. 1955 The Normal Motion of a Shock Wave Through a Non–uniform, One–Dimensional Medium. *Proc. Roy. Soc. A*, **232**, 350.

Chisnell, R. F. 1957 The motion of a shock wave in a channel, with applications to, cylindrical and spherical shock waves, *J. Fluid Mech.*, **2**, 286-298.

Choi, M. J, Coleman, A. J. & Saunders, J. E. 1993 The influence of fluid properties and pulse amplitude on bubble dynamics in the field of a shock wave lithotripter. *Phys. Med. Biol.*, **38**, 1561-1573.

Chuong, C. J., Zhong, P., Arnott, H. J. & Preminger, G. M. 1989 Stone damage modes during piezoelectric shock wave delivery. Proceedings of Shock wave lithotripsy 2: urinary and biliary lithotripsy symposim, on shock wave lithotripsy 5th, 103-106.

Chuong, C. J., Zhong, P. & Preminger, G. M. 1993 Acoustic and mechanical properties of renal calculi: implications in shock wave lithotripsy. Submitted to *J. of Endour..*

Church, C. C. 1989 A Theoretical Study of Cavitation Generated by an Extracorporeal Shock Wave Lithotripter. *J. Acoust. Soc. Am.*, **86**, 215-227.

Coleman, A. J., Saunders, J. E. & Choi, M. J. 1989 An Experimental Shock Wave Generator for Lithotripsy Studies. *Phys. Med. Biol.*, **34**, 1733-1742.

Coleman, A. J., Saunders, J. E., Preston, R. C. & Bacon, D. R. 1987 Pressure Waveforms Generated by a Dornier Extracorporeal Shock-Wave Lithotripter. *Ultrasound in Med. & Bio.*, **13**, 651-657.

Coleman, A., Choi M. J. & Saunders, J. E. 1991 Theoretical Predicitions of the Acoustic Pressure Generated by a Shock Wave Lithotripter. *Ultrasound in Med. & Bio.*, **17**, 245-255.

Coleman, A. & Saunders, J. E. 1992 A review of the physical properties and biological effects of the high amplitude acoustic fields used in extracorporeal lithotripsy. *Ultrasonics*, **31**, 75-89.

Crow, S. C. 1968 Distortion of sonic bangs by atmospheric turbulence. *J. Fluid Mech.*, **37**, 529-563.

Crum, L. A. 1988 Session G.G. Physical Acoustics V and Bioresponse to Vibration II: Extracorporeal Shock Wave Lithotripsy - Physical Aspects. *J. Acoust. Soc. Am.*, **83**, S71-S72.

Dayros, W. J., Garra, B. S., Pahira, J. J. & Zeman, R. K. The Effects of an Attenuating Medium and Increased Power on the Location and Magnitude of Lithotripter Peak Positive Pressure, Department of Radiology and Division of Urological Surgery, 1-20.

DeReggi, A. S. & Harris, G. R. 1980 Polymer hydrophone probes. in *Proc. 1980 Ultrason. Symp.*, 598-599.

DeReggi, A. S., Roth, S. C., Kenney, J. M., Edelman, S. & Harris, G. 1981 Piezoelectric polymer probe for ultrasonic applications. *J. Acous. Soc. Am.*, **69**, 853-859.

Fei, D. Y., Shung, K. K. & Wilson, T. M. 1986 Ultrasonic backscatter from bovine tissues: Variation with Pathology. *J. Acoust. Soc. Am.*, **81**, 166-172.

Field, J. E. 1991 The physics of liquid impact, shock wave interactions with cavities, and the implications to shock wave lithotripsy. *Phys. Med. biol.*, **36**, 1475-1484.

Filipczynski, L., Etienne, J. & Piechocki, M. 1992 An Attempt to Reconstruct The Lithotriptor Shock Wave Pulse in Kidney: Possible Temperature Effects. *Ultrasound in Med. & Biol.*, **18**, 569-577.

Filipczynski, L., Etienne, J. & Kujawska, T. 1994 Shock Wave Pulse Pressure After Penetration of Kidney Tissue. *IEEE Trans. Ultrason., Ferroele. Freq. Cont.*, **41**, 130-133.

Finney, R., Halliwell, M., Mishriki, S. F. & Baker, A. C. 1991 Measurement of lithotripsy pulses through biological media. *Phys. Med. Biol.*, **36**, 1485-1493.

Fischer, N., Müller, H. M., Gulhan, A., Sohn, M., Deutz, F. J., Rubben, H. & Lutzeyer, W. 1988 Cavitation effect: A possible cause of tissue injury during extracorporeal shock wave lithotripsy. in Shock Wave Lithotripsy: State of the Art, *Proc. of 4th Symp. on Shock Wave Lithotripsy*, 517-518, Plenum, NY.

Frost, N. E., Marsh, K. J. and Pook, L. P. 1974 *Metal Fatigue.*

Geise, R. A., Hobbie, R. K. & Titenour, E. R. 1993 Some Factors Affecting Cavitational Erosion of Metal Foils Used for Monitoring Lithotripter Performance. *J. Stone Disease*, **5**, 199-207.

Glaze, S., LeBlanc, A. D., Bushong, S. C. & Griffith, D. P. 1987 Patient and Personnel Exposure During Extracorporeal Lithotripsy. *Health Physics*, **53**, 623-629.

Gravenstein, J. S. (Ed.), & Peter, K. (Ed.) 1986 *Extracorporeal Shock-Wave Lithotripsy for Renal Stone Disease.* Butterworths, Boston, MA.

Grünewald, M., Koch, H. & Hermeking, H. 1987 Modelling of Shock Wave Propagation and Tissue Interaction During Extracorporal Shock Wave Lithotripsy. in

Shock Tubes and Waves: *Proceedings of the 16th International Symposium on Shock Tubes and Waves*, Ed. H. Grönig, 889, VCH, Wendheim, Germany.

Haas, J.-F. 1984 Interaction of Weak Shock Waves and Discrete Gas Inhomogeneities. Ph.D. Thesis, Graduate Aeronautical Laboratories, California Institute of Technology.

Haas, J.-F. & Sturtevant, B. 1987 Interaction of weak shock waves with cylindrical and spherical gas inhomogeneities. *J. Fluid Mech.*, **181**, 41-76.

Harris, G. 1982 Transient ultrasonic fields - A theoretical and experimental study using polyvinylidene fluoride piezoelectric polymer hydrophones. Ph.D. Thesis, Catholic University.

Hercules Inc., 1995 *Nitrocellulose, Chemical and Physical Properties.*

Hesselink, L. 1977 An Experimental Investigation of Propagation of Weak Shock Waves in a Random Medium. Ph.D. Thesis, Graduate Aeronautical Laboratories, California Institute of Technology.

Hesselink, L. & Sturtevant, B. 1988 Propagation of weak shocks through a random medium, *J. Fluid Mech.*, **196**, 513-553.

Holland, C. K. & Apfel, R. E. 1990 Thresholds for transient cavitation produced by pulsed ultrasound in a controlled nuclei environment. *J. Acoust. Soc. Am.*, **88**, 2059-2069.

Holmer, N. G., Almquist, L. O., Hertz, T. G., Holm, A., Lindstedt, E., Perrson, H. W. & Hertz, C. H. 1991 On the Mechanism of Kidney Stone Disintegration by Acoustic Shock Waves. *Ultrasound in Med. & Biol.*, **17**, 479-489.

Kaude, J. V., Williams, C. M., Millnder, M. R., Scott, K. N. & Finlayson, B. 1985 Renal Morphology and Function Immediately after Extracorporeal Shock-Wave Lithotripsy. *AJR*, **145**, 305-313.

Kambe, K., Kuwahara, M., Kurosu, S., Takayama, K., Onodera, O. & Itoh, K. 1985 An Application to Extracoporeal Lithotripsy. in *Shock Waves and Shock Tubes:*

*15th Int'l. Symp. Proc.*, Berkeley, CA, Jul. 28-Aug. 2, 1985, Eds. Bershader, D. & Hanson, R., 641.

Kawai, H. 1969 The piezoelectricity of polyvinylidene fluoride. *Japan J. App. Phys.*, **8**, 975-976.

Kim, C. 1994 Collapse of spherical bubbles in Maxwell fluids. *J. Non–Nuetonian Fluid Mech.*, **55**, 37-58.

Kroschwitz, J. I. 1985 *Encyclopedia of Polymer Science and Engineering.* 2nd Ed., Wiley, NY.

Kulkarny, V. A. 1975 An Experimental Investigation on Focusing of Weak Shock Waves in Air. Ph.D. Thesis, Graduate Aeronautical Laboratories, California Institute of Technology.

Kulkarny, V. A. & White, B. S. 1982 Focusing of waves in turbulent inhomogeneous media. *Phys. Fluids*, **25**, 1770-1784.

Kuwahara, M., Ioritani, N., Kambe, K., Taguchi, K., Saitoh, T., Shirai, S., Orikasa, S. & Takayama, K. 1989 Acoustics Cavitation Bubbles in the Kidney Induced by Focused Shock Waves for the Extracorporeal Shock Wave Lithotripsy (ESWL). in *17th Int'l Symp. on Shock Tubes and Shock Waves*, Bethlehem, PA, Ed. Y. Kim, preprint, Lehigh University, Bethlehem, PA.

Kuwahara, M.D., Masa-aki, & Takayama, Ph.D., Kazuyoshi 1987 Extracorporeal Microexplosive Lithotripter, in PRESENTED AT: *State of the Art Extracorporeal Shock Wave Lithotripsy.* Eds. Kandel, L. B., Harrison, L. H. & McCullough, D. L., Futura Publishing Co., Mount Kisco, NY.

Laake, A., Meier, G. E. A. & Szumowski, A. P. 1986 Underwater Sound Generation by Waterhammer. in PRESENTED AT: Aero- and Hydro-Acoustics IUTAM Symposium, Lyon, 1985, Ed. G. Comte-Bellot and J. E. Ffowes Williams, 333-338, Springer, Berlin Heidelberg.

Laake, A., & Meier, G. E. A. 1986 Generation of Homogeneous Cavitation by Water Sound Pulses. *Fortschtoyyr der Akustik*, **DAGA**, 593-596.

Laake, A. 1987 A Water Sound Generator for Pressure Pulses of High Energy. ISSN 0374-1257 Nr. 85, Max-Planck-Institut für Stromungsforschung, Göttingen.

Lesser, M. B. 1981 Analytic solutions of liquid–drop impact problems. *Proc. R. Lond.*, **377**, 289-308.

Lesser, M. B. & Feild, J. E. 1983 The Impact of Compressible Liquids, *Ann. Rev. Fluid. Mech.*, **15**, 97-122.

Lide, D. R. & Frederikse, H. P. R. 1994 *Handbook of Chemistry and Physics.* 75th Ed., CRC Press Inc., OH.

Likhachev, V. N. 1989 Focusing of Shock Waves in a Highly Viscous Fluid. *U. S. S. R.*, **53**, 750-756.

Lingeman, J. E., Newman, D., Mertz, Jack H. O. , Mosbaugh, P. G., Steele, R. E., Kahnoski, R. J., Coury, T. A. & Woods, J. R. 1986 Extracorporeal Shock Wave Lithotripsy: The Methodist Hospital in Indiana Experience, *J. of Urology*, **135**, 1134-1137.

Lingeman, J. E., Woods, J. R. & Toth, P. D. 1990 Blood Pressure Changes Following Extracorporeal Shock Wave Lithotripsy and Other Forms of Treatment for Nephrolithiasis. *JAMA*, **263**, 1789-1794.

Loske, A. M. MSC. & Prieto, F. E. 1993 The Influence of Electrode Shape on the Performance of Electrohydraulic Lithotripters. *J. Stone Disease*, **5**, 228-240.

Lush, P. A. 1983 Impact of a liquid mass on a perfectly plastic solid. *J. Fluid Mech.*, **135**, 373-387.

Lynch, C. T. 1974 *Handbook of Materials Science.* Vol. I, General Properties, CRC Press Inc., OH.

Malecki, I. 1969 *Physical Foundations of Technical Acoustics.* 1st English ed.,Pergamon Press, Oxford, NY.

Malone, D. E., Becker, C. D., Reich, D., Quenville, N. F. & Burhenne, J. 1989 Soft-Tissue Effects of Biliary Extracorporeal Shockwave Lithotripsy in Swine. *Br. J. Radiol.*, **62**, 843-848.

Marsh, S. 1986 LASL Shock Hugoniot Data (Water). University of California Press, Berkeley, Los Angeles, London.

Mendez, J., Franklin, B. & Kollias, J. 1976 Effect of Ultrasound on the Permeability of $D_2O$ Through Cellulose Membranes. *Biomedicine*, **25**, 121-122.

Miner, M. A. 1945 *J. Appl. Mech.*, **12**, A159.

Mott, G. 1971 Reflection and Refraction Coefficients at a Fluid–Solid Interface. *J. Acous. Soc. Amer.*, **50**, 819-828.

Müller, M. 1987 Experimental Investigations on Focusing of Weak Spherical Shock Waves in Water by Shallow Ellipsoidal Reflectors. *Acustica*, **64**, 85-93.

Müller, M. 1988 Experimental Investigation into the Focussing of Spherical Shock Waves in Water using Deep Ellipsoidal Reflectors. *Acustica*, **66**, 258-266.

Nair, B. & White, B. S. 1991 High–Frequency Wave Propagation in Random Media–A Unified Approach. *SIAM J. Appl. Math.*, **51**, 374-411.

Neuhausel, D. J. 1987 Lithotripsy, A Survey. J. of Clincal Engineering, Vol. 12 (4), 283-295.

Philipp, A., Delius, M., Scheffczyk, C., Vogel, A. & Lauterborn, W. 1993 Interaction of lithotripter–generated shock waves with air bubbles. *J. Acoust. Soc. Amer.*, **93**, 2496-2509.

Pierce, A. D. 1968 Spikes on Sonic–Boom Pressure Waveforms. *J. Acous. Soc. Amer.*, **44**, 1052-1061.

Pierce, A. D. 1981 *Acoustics : An Introduction to its Physical Principles and Applications* McGraw-Hill Book Co., NY.

Pieto, F. E. & Loske, A. M. 1991 An underwater shock wave research device, *Rev. Sci. Instrum.*, **62**, 1849-1854.

Plesset, M. S. & Chapman, R. B. 1971 Collapse of an initially spherical vapour cavity in the neighbourhood of a solid boundary. *J. Fluid Mech.*, **47**, 283-290.

Plotkin, K. J. & George, A. R. 1972 Propagation of weak shock waves through turbulence. *J. Fluid Mech.*, **54**, 449-467.

Reed, R. & Greenwoll, J. 1988 The PVF2 piezoelectric polymer shock stress sensor signal conditioning and analysis for field test applications. Sandia National Laboratories, *SAND*, 88-2907A.

Reinhart, T. J. 1987 *Engineered Materials Handbook.* **2**, ASM International, OH.

Ridah, S. 1988 Shock waves in water. *J. Appl. Phys.*, **64**, 152-158.

Rigatti, P., Colombo, R., Centemero, A., Francesca, F., Di Girolamo, V., Montorsi, F. & Trabucchi, E. 1989 Histological and Ultrastructural Evaluation of Extracorporeal Shock Wave Lithotripsy-Induced Acute Renal Lesions: Preliminary Report. *Eur Urol*, **16**, 207-211.

Schwendeman, D. W. 1988 Numerical Shock Propagation in Non-Uniform Media. *J. Fluid Mech.*, **188**, 383-410.

Setchell, R. E., Storm, E. & Sturtevant, B. 1972 An investigation of shock strengthening in a conical convergent channel. *J. Fluid Mech.*, **56**, 505-522.

Shung, K. K., Yuan, Y. W., Fei, D. Y. & Tarbell, J. M. 1984 Effect of flow disturbance on ultrasonic backscatter from blood. *J. Acous. Soc. Amer.*, **75**, 1265-1272.

Skop, R. A., & Showalter, J. G. 1977 The Refraction of a Plane Shock Wave at an Air-Water Interface. *NRL Memorandum Report 3628*, Naval Research Laboratory, Washington, D. C.

Skvortsov, Y. V., Komel'kov V. S. & Kuznetsov, N. M. 1960 Expansion of a Spark Channel in a Liquid. *Zhur. Tek. Fiz.*, **30**, 1165-1177.

Smith, L. H., Drach, G., Hall, P., Lingeman, J., Preminger, G., Resnick, M. I. & Segura, J. W. 1991 National High Blood Pressure Education Program (NHBPEP) Review Paper on Complications of Shock Wave Lithotripsy for Urinary Calculi. *Amer. J. Med.*, **91**, 635-641.

Sommerfeld, M., & Muller, H. M. 1986 Experimental and Numerical Studies of Shock Wave Focusing in Water. *Experiments in Fluids M 253*, Friedrich-Alexander-Universitat, Erlangen, FRG.

Sturtevant, B. & Kulkarny, V. J. 1976 The focusing of weak shock waves. *J. Fluid Mech.*, **73**, 651-680.

Sturtevant, B. 1990 The physics of shock wave focusing in the context of extracorporeal shock wave lithotripsy. in *Proceedings of the International Workshop on Shock Wave Focusing*, Shock Wave Research Center, Institute of Fluid Science, Tohoku University, Sendai, JAPAN.

Sturtevant, B., Hartenbaum, B., Chuong, C. & Preminger, G. M. 1992 In vivo pressure measurements during extracorporeal piezoelectric lithotripsy. Annual Meeting, *Amer. Urolog. Assoc.*, Washington.

Takayama, K., Esashi, H. & Sanada, N. 1983 Propagation and Focusing of Spherical Shock Waves Produced by Underwater Microexplosions. in *Shock Tubes and Waves: 14th Int'l. Symp. on Shock Tubes and Waves*, Eds. Archer, R. D. and Milton, B. E., 553, Sydney Shock Tube Symp. Publishers, Sydney.

Takayama, K. 1993 Application of Underwater Shock Wave Focusing to the Development of Extracorporeal Shock Wave Lithotripsy. *JPN. J. Appl. Phys.*, **32**, 2192-2198.

Thompson, P. A. 1972 *Compressible Fluid Dynamics.* McGraw–Hill, NY.

Timoshenko, S. 1940 *Theory of Plates and Shells.* The Maple Press Co., York, PA.

Van der Grinten, J. G. M., Smits, M. A., Van der Kogel, H. & van Dongen, M. E. H. 1987 Shock-Induced Wave Propagation in and Reflection from a Porous Column Partially Saturated with Water. in *Shock Tubes and Waves: Proceedings of the 16th International Symposium on Shock Tubes and Waves*, Ed. H. Grönig, VCH, Wendheim, Germany.

Wanner, J.-C., Vallee, J. Vivier, C. & Thery, C. 1972 Theoretical and Experimental Studies of the Focus of Sonic Booms. *J. Acous. Soc. Amer.*, **52**, 13-32.

Whelan, J. P., & Finlayson, B. 1988 An experimental model for the systematic investigation of stone fracture by extracorporeal shock wave lithotripsy. *J. of Urology*, **140**, 395-400.

Whitham, G. B. 1974 *Linear and Nonlinear Waves*. Wiley, NY.

Williams, J. E. F. & Howe, M. S. 1973 On the possibility of turbulent thickening of weak shock waves. *J. Fluid Mech.*, **58**, 461-480.

Williams, A. R., Delius, M., Miller, D. L. & Schwarze, W. 1989a Investigation of cavitation in flowing media by lithotripter shock waves both in vitro and in vivo. *Ultrasound in Med. & Biol.*, **15**, 53-60.

Williams, C. M., Thomas, Jr., W. C., Newman, R. C. & Bland, K. I. 1989b Right Renal Trauma: A Side Effect of Biliary Lithotripsy. *New Eng. J. of Med.*, **320**, 739-739.

Zhong, P., Chuong & C. J. 1993a Propagation of shock waves in elastic solids casued by cavitation microjet impacts. I: Theoretical formulation. *J. Acoust. Soc. Am.*, **94**, 19-28.

Zhong, P., Chuong, C. J. & Preminger, G. M. 1993b Propagation of shock waves in elastic solids casued by cavitation microjet impacts. II: Application in extracorporeal shock wave lithotripsy. *J. Acoust. Soc. Am.*, **94**, 29-36.

Zwillinger, D. I. & White, B. S. 1985 Propagation of Initially Plane Waves in the Region of Random Caustics. *Wave Motion*, **7**, 207-227.

# Exsolution of Volatiles

# (Part II)

Thesis by

Danny D. Howard

In Partial Fulfillment of the Requirements

for the Degree of

Doctor of Philosophy

California Institute of Technology

Pasadena, California

1996

(Submitted April 5, 1996)

# Acknowledgements

This part of my thesis is dedicated to my father, the late Willie James Howard.

# Abstract

This work examines the exsolution of volatiles—carbon dioxide from water—in a cylindrical test cell under different pressure conditions. Water was supersaturated with carbon dioxide under various pressures (620 to 1062 kPa), and depressurized rapidly to investigate how carbon dioxide is undissolved, exsolution, and its effects on the surrounding environment. Cavities grow as a result of convective diffusion: They move before depleting carbon dioxide in a given region. The radius of a cavity in this environment grows at a faster rate ($t^{\frac{2}{3}}$) than that of a cavity at rest ($t^{\frac{1}{2}}$). Bubble growth rates were inferred by measuring the bulk liquid using high speed motion pictures. Water in the test-cell is accelerated as a result of buoyancy induced by cavity growth. Cavities are elliptical in shape and grow until mutual interaction causes them to fragment. Accelerations range from 10 to 100 g were measured with velocities ranging from 7 to 13 m/s.

# Contents

# List of Figures

# List of Tables

# Chapter 1  Introduction

## 1.1  Motivation

Understanding the exsolution of volatiles is not only important in many engineering applications, but medical and geological applications as well. Exsolution occurs anytime there is a substantial amount of gas, volatile, dissolved in a solvent and there is rapid decompression. It can be a problem in the pumping of saturated liquids or liquid sprays (Eddington 1966). In order to keep the liquid saturated, it must remain at the saturation pressure; however, if severe depressurization occurs cavities can form and cause separation within the conduit, affecting the efficiency of the pumping system. Exsolution of volatiles can also pose problems in fluid powered lines: Exsolution of dissolved gases in the working fluid can cause column separation in return lines of fluid power pipelines during decompression operations (Shinada 1994). Another hydrodynamic problem of this nature is when a fluid has to negotiate an obstacle. If the fluid is supersaturated with a gas, the pressure drop encountered can induce exsolution. Extensive damage can be caused when cavities/bubbles are arrested by a solid object (Field 1991; Lesser 1981; Lesser& Field 1983; Lush 1983).

A medical application of this process has to do with suspected damage in the kidney induced by a Dornier HM3 Extracorporeal Shock Wave Lithotripter (ESWL) (Van Liew *et al.* 1994). In these machines shock waves are focused to break kidney stones; each shock wave is accompanied by very strong diffracted expansion waves which drops the pressure and induces cavitation in water. Because body fluids contain dissolved nitrogen, exsolution could possibly increase the size and number of cavities, thereby intensifying damage.

Another medical application of this process is related to decompression sickness (Hill *et al.* 1994; Melamed *et al.* 1992; Van Liew *et al.* 1994). Divers intake air at increased pressures while descending to great depths; oxygen is used in tissue

metabolism, whereas nitrogen is dissolved—the amount is both pressure and temperature dependent. When the diver ascends very quickly to a lower pressure state, nitrogen must exsolve to maintain equilibrium with the environment, bombarding the body with nitrogen gas. This condition is known as decompression sickness. Perhaps a more illustrative example would be the puncturing of a spaceship or space station, exposing the cabin to vacuum.

Another area of applicability involves exsolution of volatiles in a volcanic eruption. When a dome that houses magma ruptures, high temperature, high pressure magma is exposed to low ambient pressure. The dissolved volatiles will be exsolved from the magma. Since decompression is severe, the process will be violent inducing accelerations on the order of 200 g with exit velocities on the order of a few hundred meters per second in some cases (Mader *et al.* 1994).

Exsolution of volatiles is a field which has not received very much attention. However, as seen in the applications presented, a working knowledge of this area can prove beneficial to understanding phenomena in many different disciplines.

## 1.2  Background

### 1.2.1  Solubility Of Gas In Liquid

The solubility of carbon dioxide is determined by a chemical reaction. This reaction greatly increases the solubility of carbon dioxide by forming the compound $H_2CO_3$. Figure 1.1 plots the mole fraction of carbon dioxide versus pressure for the range of interest. In this range the mole fraction is a linear function of pressure. The experimental data was taken from Houghton (1956), and will be used to predict solubilities in the current experiments.

### 1.2.2  Bubble Growth

This section will follow very closely the derivation of Van Wijngaarden (1967) for the growth of a small cavitation bubble by convective diffusion. Van Wijingaarden starts
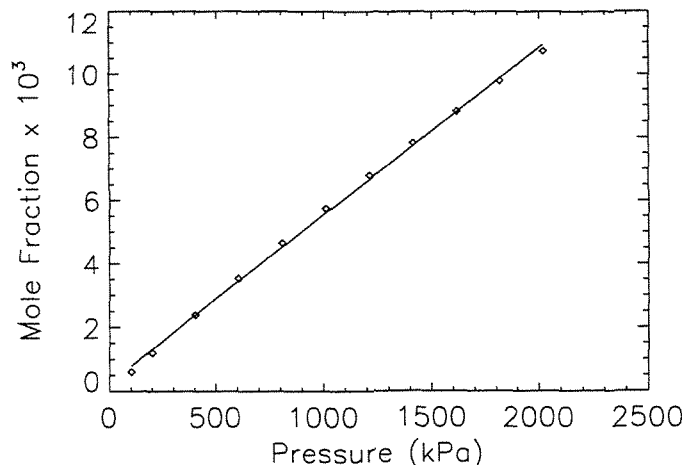
Figure 1.1: Solubility of carbon dioxide.

with the equilibrium bubble equation, and using the perfect gas equation develops a differential equation in terms of volume and number of bubbles. Next he finds a relationship between the number of bubbles and the convection of gas dissolved in the liquid. The differential equation is then solved to determine the growth rate of a bubble in a convective field.

Consider a local density deficit large enough to counter surface tension. The equilibrium equation for an isolated spherical bubble or cavity is (Plesset 1962)

$$P_v = P_f + \frac{2\sigma}{R} \tag{1.1}$$

where $P_v$ represents vapor pressure; $P_f$ represents pressure in the liquid; and $\frac{2\sigma}{R}$ represents stress due to surface tension. A bubble can exist if the excess pressure is balanced by surface tension; the radius where this occurs is known as the critical radius (Plesset 1962),

$$R_{cr} = \frac{2\sigma}{\Delta P}. \tag{1.2}$$

In order for a bubble to grow, there must be some driving mechanism to provide work to overcome surface forces; otherwise, the bubble will collapse. The driving force is

gas diffusion into cavities.

Consider a force balance on a bubble in this environment:

$$P_g + P_v - P_f - \frac{2\sigma}{R} = \rho\left[R\ddot{R} + \frac{3}{2}\dot{R}\right] + \frac{4\mu\dot{R}}{R} \qquad (1.3)$$

where $P_g$, $P_f$, $\dot{R}$, $\ddot{R}$, and $\mu$ represent pressure in the bubble, hydrostatic pressure, bubble velocity, bubble acceleration and the coefficient of viscosity, respectively. Because Van Wijngaarden was interested in slowly growing bubbles, he neglected the time-dependent terms reducing Equation 1.3 to an equilibrium equation.

$$P_f + \frac{2\sigma}{R} = P_g + P_v \qquad (1.4)$$

Also, it was assumed that the bubble was fixed with respect to the fluid, so $P_f$ represents a static pressure.

The perfect gas equation is

$$P_g = \frac{NkT}{V} \qquad (1.5)$$

where N, k, T and V represent the number of moles of gas, universal gas constant, temperature and volume. Differentiating the perfect gas equation and using Equation 1.4, Van Wijngaarden developed an equation to determine the bubble volume,

$$\frac{dV}{dt} = \frac{R_u T}{P_f - P_v + \frac{4}{3}\frac{\sigma}{R}} \frac{dN}{dt}. \qquad (1.6)$$

If the denominator goes to zero, the volume goes to infinity denoting an explosive growth which marks the threshold for vaporous cavitation. In order to solve the above equation, Van Wijngaarden obtained an equation for gas flux into a bubble in terms of solution concentration. If the liquid concentration ($C_\infty$) is much larger than the equilibrium concentration at bubble interface ($C_0$), then there is a concentration gradient. The connection between the mass flux and concentration gradient normal

to the surface is given as follows:

$$\frac{dN}{dt} = \int D \frac{\partial c}{\partial n} dS \tag{1.7}$$

where D represents the diffusion coefficient. Van Wijngaarden used a governing equation for concentration in the following form:

$$\frac{\partial c}{\partial t} + W \cdot \nabla c = D \nabla^2 c \tag{1.8}$$

where W represents convective velocity.

The growth rate of a bubble in an isolated medium which has a constant velocity with respect to that medium can be obtained by solving Equations 1.6, 1.7 and 1.8. Even though the bubbles become distorted as they grow, these equations can be used to estimate growth rates. Equation 1.7 determines the growth rate in terms of gas flux into a bubble. These equations were solved by Van Wijngaarden who followed the solution of Parkin and Kermeen (1963), but modified the solution to include the effects of vapor and surface tension, and incorporated a model developed by Levich (1962),

$$\frac{dN}{dt} = 4 \left( C_\infty - C_0 \right) \left( 2\pi R^3 UD \right)^{\frac{1}{2}}. \tag{1.9}$$

In solving this equation, Equation 1.8 was reduced to a steady state equation. Using Equations 1.9 and 1.6, Van Wijngaarden obtained the following integral:

$$\int_{t_0}^{t_1} dt = \frac{\sqrt{\pi}}{\sqrt{2UDkT \left( C_\infty - C_0 \right)}} \int_{R_0}^{R_1} \left( P_f - P_v + \frac{4}{3} \frac{\sigma}{R} \right) R^{\frac{1}{2}} dR. \tag{1.10}$$

If $P_f$ - $P_v$ is large compared to the surface tension, the following solution can be obtained:

$$R = \left( \frac{3\sqrt{2UDkT} \left( C_\infty - C_0 \right)}{2\sqrt{\pi} \left( P_f - P_v \right)} \right)^{\frac{2}{3}} t^{\frac{2}{3}}. \tag{1.11}$$

The above equation states how convective diffusion induces a growth rate ($t^{\frac{2}{3}}$) different from that predicted by classical bubble growth theory ($t^{\frac{1}{2}}$) where the bubble is at rest with respect to the medium (Epstein & Plesset 1950).

## 1.3 Bubble Interaction Experiments

In order to understand the violent nature of this process, it is necessary to study certain key parameters—bubble interaction, acceleration and fragmentation. Detailed work has been done in this area from two different perspectives. The evaporation of fluid by explosive boiling, and the exsolution of gas from a liquid. This work enables us to gain a better understanding of the violent nature that fluids exhibit either during explosive boiling or violent degassing.

### 1.3.1 Evaporation Wave Experiments

There are two types of evaporation waves: waves with bubbly upstream liquid and waves with pure upstream liquid. Fritz (1965) was one of the first to study evaporation waves in bubbly upstream liquids. The evaporation wave speeds were on the order of 1 to 2 m/s, and the acceleration front region was measured to be several centimeters thick. This experiment was done in a vertical glass tube with water (degassed and normal) pressurized to 3.5 atm and heated to temperatures ranging from 105° to 125° C.

Grolmes and Fauske (1974) were the first to observe evaporation waves with pure upstream liquid states. They used refrigerant 11, methyl, alcohol and degassed water. Once the superheat exceeded a threshold value—different for each liquid and test–cell—evaporation waves were observed. The average velocity of the front ranged from .32 to .48 m/s

A very detailed study of evaporation waves was done by Hill (1991) using refrigerants 12 and 114 and with similar experiments done later by Moreira (1994) using dodecane. Hill used high speed motion pictures along with still photography to study

evaporation waves, and described each division of the flow—the upstream liquid region, wave front–leading edge bubble region and developed downstream two phase flow region. He also identified three start–up modes which depended on the test liquid and reservoir pressure. The evaporation wave speeds observed were around .63 m/s with the two phase flow traveling at 35 m/s; the wave front thickness was on the order of 1 centimeter.

## 1.3.2   Exsolution Experiments

In exsolution experiments, liquid phase change is eliminated from the complex problem. The only experiments of this type known to the author have been conducted at GALCIT by Zhang and Sturtevant and presented in a paper by Mader *et al.* (1994). In these experiments carbon dioxide was dissolved in water under various pressures at ambient temperatures, and rapidly depressurized to a pressure above the vapor pressure of water. Fragmentation was observed and resulted from bubble rupture due to expansion and acceleration of the flow. The velocities were around 14 m/s with accelerations up to 200 g, and the volume growth rate was shown to increase as $t^2$ which implies that bubble radius growth increased as $t^{\frac{2}{3}}$.

## 1.3.3   Present Experiments

The present work was designed to follow work done by Zhang and Sturtevant—taking the experiments a step farther to higher pressures and mass flow rates with better temporal and spatial resolution. In addition, the behavior of the fragmented flow was studied far down stream. The experimental method will be discussed in Chapter 2, while a detailed observation will be discussed in Chapter 3; Chapter 4 will give conclusions.

# Chapter 2  Experimental Method

## 2.1  Experimental Apparatus

The basic test facility was built by Larry Hill; modifications were made as necessary to achieve desired test conditions. Additional references to this test facility can be found in Hill's thesis (1990). The experimental facility can be seen pictorially in Figure 2.1 and schematically in Figure 2.3, with the set–up consisting of a test–cell, reservoir, control panel, digitizing oscilloscope, two cameras and interfacing electronics. Operating gases and vacuum apparatus are located behind the test assembly; the test liquid is located above the control panel adjacent to the reservoir unit.

### 2.1.1  Test–Cell/Reservoir Unit

The test–cell/reservoir unit consists of a low pressure reservoir tank, a reservoir adapter plate, knife blade assembly and test–cell assembly. The test–cell assembly is connected to the reservoir via the reservoir adapter plate, and separated by an aluminum diaphragm (see Table 2.4) which is ruptured by a knife blade when the desired test conditions have been achieved, and all recording instruments are ready.

The low pressure tank consists of two cylindrical sections that are flanged on both ends and bolted together, and was constructed from $\frac{1}{2}$–inch–thick rolled stainless steel; the flanges are $\frac{3}{4}$ inches thick, with 16, $\frac{1}{2}$–inch–diameter holes. Both ends are closed using $\frac{3}{4}$–inch–thick aluminum plates. The tank is 3 feet in length and 2 feet in diameter (i.d.) with a volume of 9.4 cubic feet. It is elevated 4 feet off the floor by a slotted–angle iron construction that was designed to put the test–cell assembly at eye level when the observer is seated. It will accommodate pressures between vacuum and 4 bars of absolute pressure.

The reservoir adapter plate was made from $\frac{3}{4}$–inch–thick aluminum plate, 10 inches
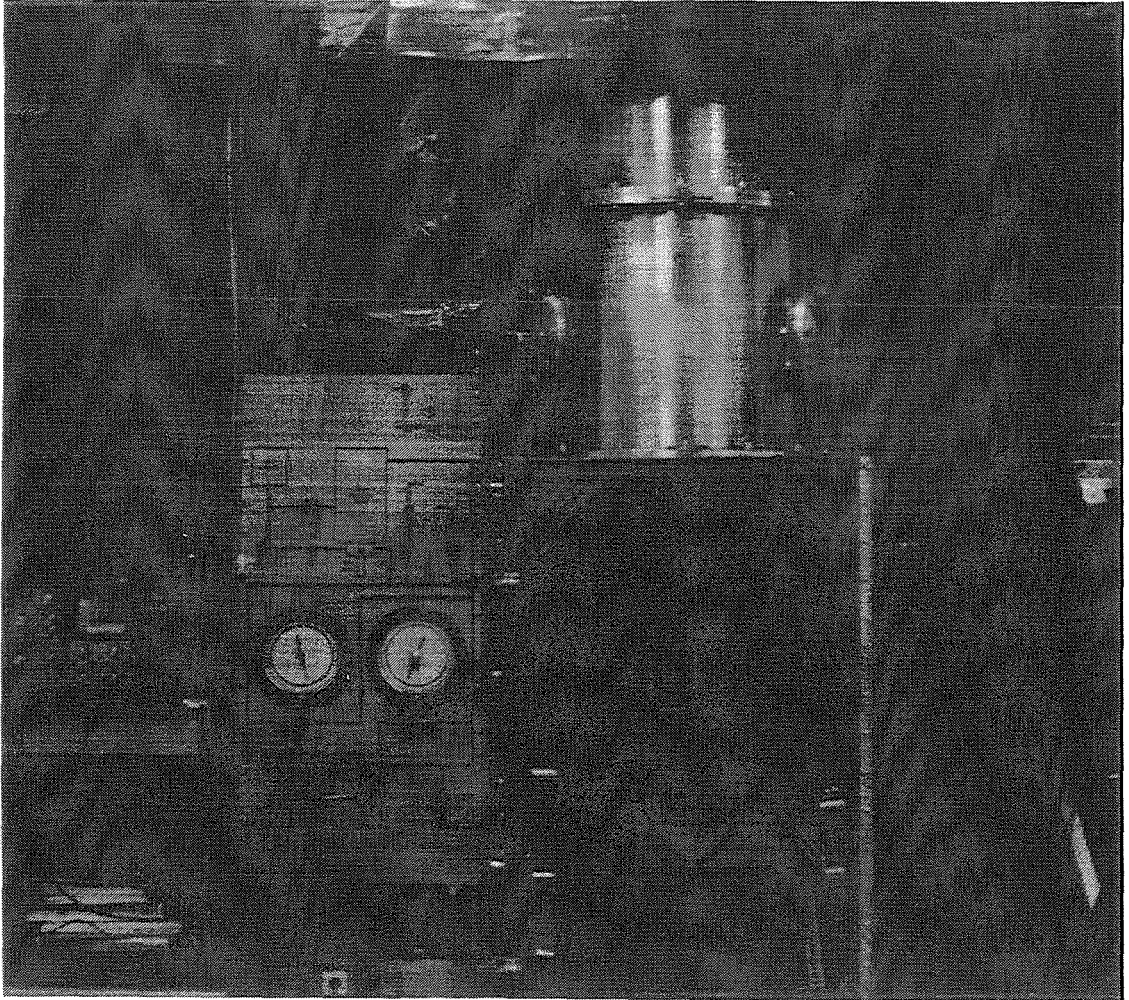
Figure 2.1: Experimental test facility.

in diameter. It is bolted to the low pressure tank with 6, $\frac{3}{8}$–16 inch bolts, and is sealed with a single O-ring . The bottom of the reservoir adapter plate has a $\frac{3}{8}$–inch extension (2.995 inches in diameter) which protrudes into and seals against the test–cell adapter plate—actually against the diaphragm—with an O-ring. The test–cell adapter plate is connected to the reservoir adapter plate via 2, $\frac{1}{2}$–inch–diameter stainless steel rods which allows the test–cell assembly vertical mobility for diaphragm insertion. It bolts to the reservoir adapter plate via 4, $\frac{3}{8}$–16 bolts.

The diaphragm cutter assembly is located on top of the reservoir adapter plate as seen in Figure 2.2 (free standing). This assembly consists of a pneumatic cylinder, an extension rod , crossed knife blades and supporting assembly. The pneumatic cylinder was purchased from Grainger Industrial and Commercial Equipment Company; it has a 2 inch stroke with an available force (lb) of .44 times the energizing pressure (psi). It is connected to a three way solenoid valve which returns the line pressure to that of the reservoir, allowing the cylinder to be de-energized by its spring mechanism. In order for the diaphragm rupture to be independent of the knife speed, the knife blade taper was made very small (6°).

The test–cell assembly (Figure 2.2) consists of the test–cell adapter plate, a glass tube and the test–cell holder plate. The test–cell adapter plate was made from 1–inch–thick aluminum plate, 5.25 inches in diameter, and has a 1.7 inch extension that is 3.25 inches in diameter (o.d.)  which protrudes to provide support for the glass tubing. A seal is made at the top with the reservoir adapter plate in two places: in the depression where the diaphragm is placed, and on the outer edge of the plate around the stainless steel connecting rods. So, the diaphragm is sandwiched between the reservoir and test–cell adapter plates, and sealed by their respective o-rings.

Glass tubing is inserted into the extension of the test–cell adapter plate using a nylon sleeve—this allows for variability in the size of the glass tubing—and is sealed at the top with an o-ring. The bottom of the test–cell is closed with the test–cell holder plate. This plate was made from a 2–inch–thick aluminum plate, 5 inches in diameter. The glass tubing is fitted into the test–cell holder plate also using a nylon sleeve; it is sealed at the bottom using an annular gasket instead of an O-ring to
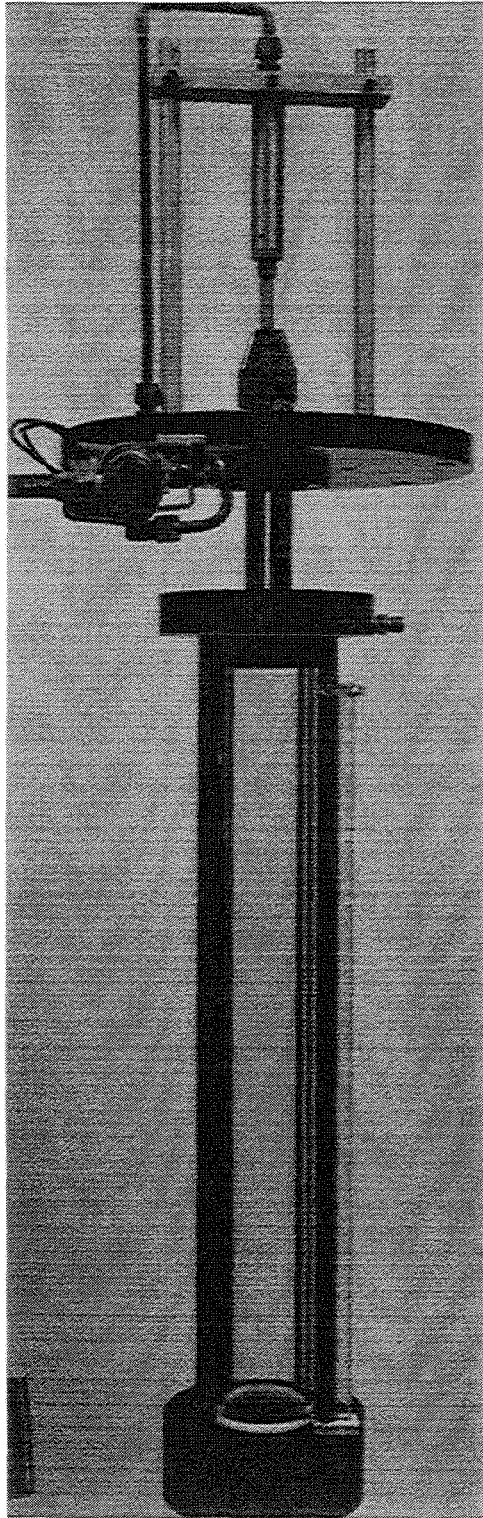
Figure 2.2: Test–cell assembly and reservoir adapter unit.

minimize nucleation sites. Four $\frac{1}{2}$–inch diameter rods hold the assembly together, and seal the two plates against the glass tubing. Each rod is torqued equally to prevent asymmetric loading.

The glass tubing has an outer diameter of 2.756±0.001 inches and an inner diameter of 2.000 inches; the tubes used were 19 and 20 inches in length. The experimenter is protected from possible explosion by a 5 inch by 5 inch lexan box, 40 inches in length with a $\frac{3}{8}$–inch wall thickness. This box also served as a light reflector to direct light into the test–cell.
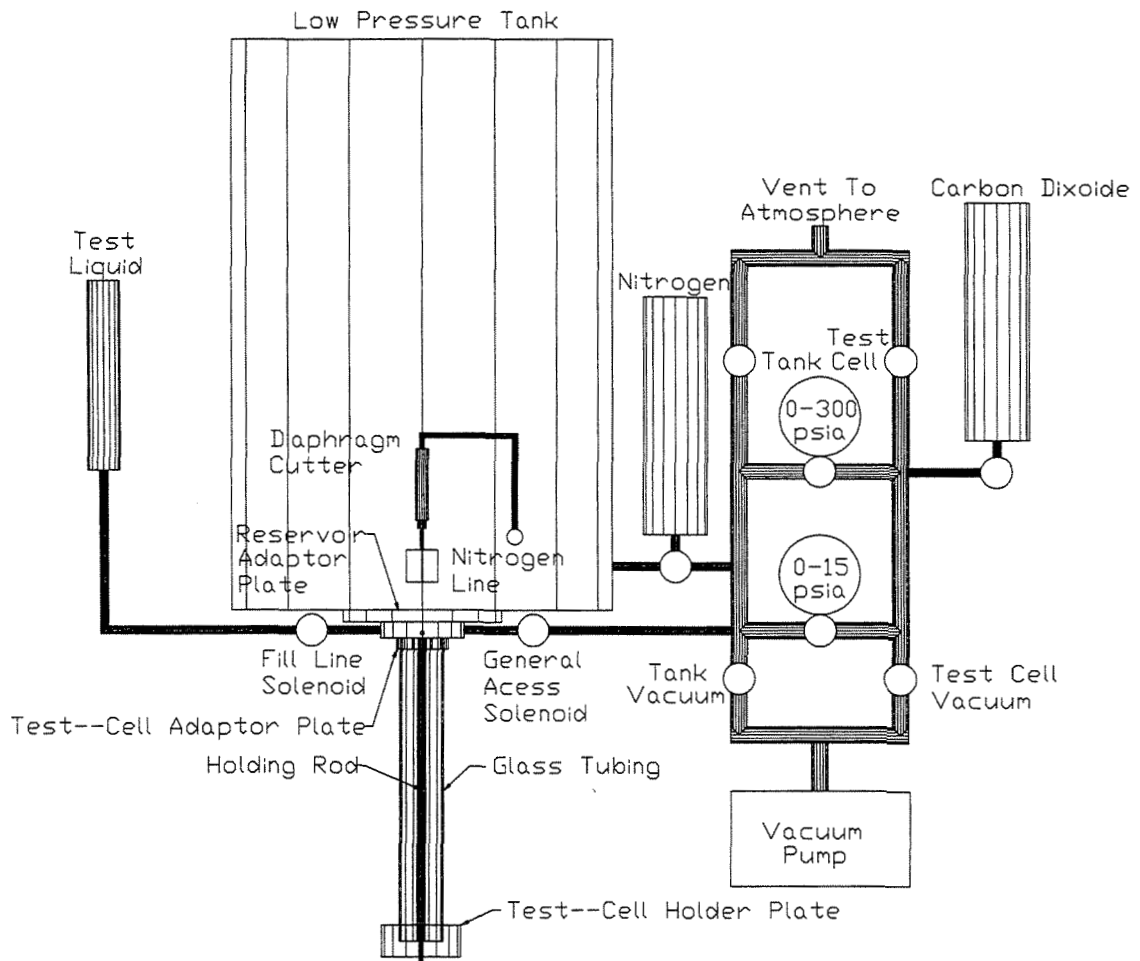


Figure 2.3: Schematic of test facility control system.

## 2.1.2 Control Panel

A schematic of the control panel can be seen in Figure 2.3. It consists of two Heise 6–inch bourdon–tube pressure gauges each connected by a three–way ball valve which allows the experimenter to measurer test–cell pressure, reservoir pressure or to turn the gauge off. Each gauge covers a specific range of interest: The 0 to 15 psia range is covered by the gauge on the left while the 0 to 300 psia range is covered by the gauge on the right (refer to Figure 2.1)—both are accurate to 0.1 % full scale. The test–cell is accessed by two types of lines: The fill line is used to supply the test–cell with test liquid, and the general access line monitors and regulates the pressure. Each line is equipped with a solenoid valve at the test–cell to minimize leaks and pressure drops. The fill line solenoid is open only during filling operations. However, the general access line stays open to allow the pressure to be monitored until the diaphragm solenoid is activated—it closes for two seconds and reopens. Pressure in the reservoir can be monitored and regulated as well. As mentioned earlier, the test liquid is located above the instrument panel and test–cell; this allows the test–cell to remain at the test pressure while filling. In some cases a very small $\Delta P$ (1 psi) was applied to combat friction in the line.

## 2.2 Instrumentation

### 2.2.1 Pressure Measurements

Pressure measurements were taken using PCB high resolution piezoelectric pressure transducers (model number 112A1) which were amplified using a PCB amplifier (model 482A04). This model of transducer measures dynamic and sound pressure from .069 to 690 kPa at any static level from full vacuum to 1,379 kPa. It has a fast rise time (2 $\mu$s), and is noted for its compatibility with liquids. Two transducers were used: One at the exit, located in the test–cell adapter plate, and the other at the bottom, located in the test–cell holder plate.

Piezoelectric transducers have two notable characteristics: They are dynamic and

| Property | Unit | Transducer | Amplifier | Oscilloscope |
|---|---|---|---|---|
| Manufacturer | N/A | PCB | PCB | Nicolet |
| Model | N/A | 112A1 | 482A04 | 409B |
| Linearity | % F.S. | 1 | 1 | 0.1 |
| Signal to Noise Ratio | dB | 108 | 90 | 72 |
| Time Constant | s | 1 | 10 | D.C. coupled |

Table 2.1: Properties of hardware.

pyro–electric; dynamic in the sense that a step change will eventually decay to zero—the time of decay depends on the time constant and does so in an approximately exponential fashion—and pyro–electric in the sense that the pressure sensitivity changes with temperature. Because the time constant was greater than one second, the former was not a problem. However, the exit transducer was thermally shielded using RTV Silicon Rubber Cement.

Data were taken using a Nicolet 4094B Digital Oscilloscope. It was triggered when the signal from the exit transducer reached a preselected voltage; this voltage was induced by an expansion wave when the diaphragm ruptured. Data were stored redundantly: On $5\frac{1}{4}$ inch floppy disks in order to acquire it back to the oscilloscope, and on the network, via an IOTECH bus for data analysis. The schematic of the pressure acquisition set–up can be seen in Figure 2.4, and a list of properties of the transducer, oscilloscope and amplifier are given in Table 2.1.

## 2.2.2 High–Speed Motion Pictures.

Flow visualization was accomplished using a Hycam II high speed 16 mm motion picture camera, manufactured by Redlake Corporation. This camera has an event trigger function which was used to initiate the experiment: The camera sends a signal to open the diaphragm cutter's solenoid valve once a steady state filming rate has been achieved. Hill built the event trigger box to specifications given by Redlake Corporation. A schematic of the filming set–up can be seen in Figure 2.4.

The Hycam exposes the film via a multifaceted prism which allows it to take up to 11,000 frames per second; the film length depends on the framing rate—the higher
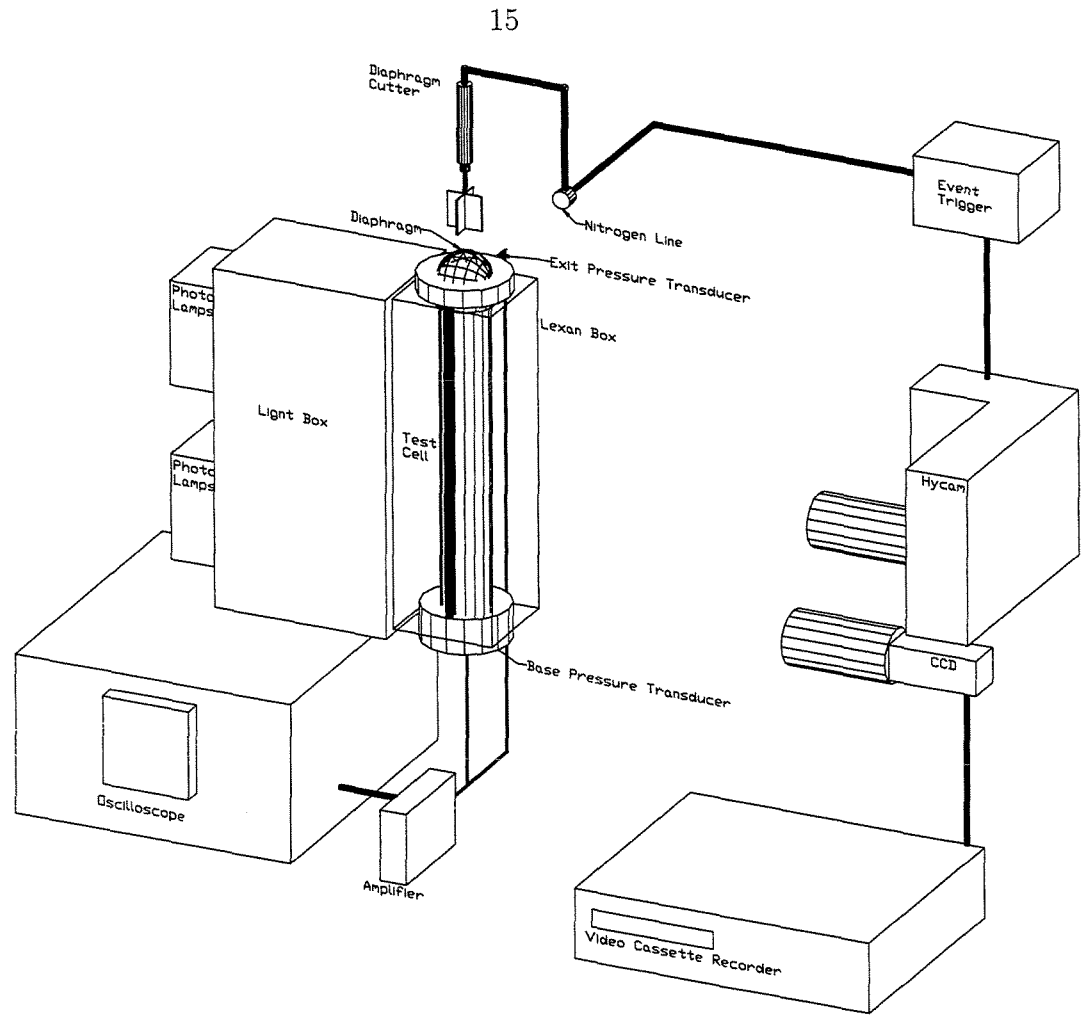
Figure 2.4: Schematic for motion picture runs.

the framing rate the more film needed to accelerate the camera to the appropriate speed. A table was provided by Redlake to determine the necessary length of film for each framing rate as well as the associated test times.

The film is exposed to timing markers so that the actual framing rate may be determined. In the current experiments a framing rate of 3000 frames per second was used. A 100 foot roll of film was necessary to accelerate the camera to speed and film each experiment. Two types of film were used: Eastman 7222 Double–X Negative black and white film (ASA 200) and Fujii 8670 color film (ASA 500). Even though no color features are discernible in the pictures, the color film proved to give better resolution.

The test–cell was illuminated from the back using two 1000 watt FCM photo–

lamps mounted in Berkey Colortran fixtures (Model 104–051). These lamps were connected to a Power Stat voltage controller (Model 116B) to regulate intensity, and mounted at the entrance of a light tube (19 × 50 × 25.4 cm) with a highly polished aluminum surface. Light was distributed through the test–cell using 0.3 cm–thick frost glass located at the exit of the light tube. The aluminum lined safety box provided additional illumination by reflecting scattered light into the test–cell.

A Nikon Macro–Zoom lens (70–210 mm, f4–f5.6) was used, and the aperture adjusted along with the light source in order to optimize the picture quality. The test–cell was divided into 3 photographing regions—9.5 cm to 22 cm (interface view), 22 cm to 35 cm (intermediate view) and 35 cm to the top (exit view)—in order to maximize the depth of field and minimize the wide angle effect of a shallow focus. The camera was positioned 2.7 meters away from the test–cell to increase the visible length of the test–cell.

## 2.2.3  Secondary Observations

In each test the liquid was monitored using a Progressive Scanning Full Frame Shutter Camera (Model TM–9700)—also known as a CCD camera— manufactured by Pulnix. It has a $\frac{2}{3}$–inch progressive scanning interline transfer CCD imager with a television resolution of 570 (H) × 584 (V) pixels, and operates at 14.3 MHz, and has an electronic shutter speed range of $\frac{1}{125}$ to $\frac{1}{16000}$ seconds. This camera was connected to a Sony VCR where the images were recorded at 30 frames per second; however, the $\frac{1}{16000}$ second shutter speed was used to provide the highest sensitivity. The CCD was also fitted with a Nikon Macro–Zoom lens (70–210 mm, f4–f5.6). It was positioned under the Hycam, and set–up to view the test liquid.

| Property | Unit | Water | Carbon Dioxide |
|---|---|---|---|
| Chemical Formula | N/A | $H_2O$ | $CO_2$ |
| Molecular Weight | N/A | 18.02 | 44.01 |
| Ratio of Specific Heats ($\gamma$) | N/A | N/A | 1.29 |
| Gas Constant (R) | J/kg K | N/A | 188.92 |
| Vapor Pressure@20C | kPa | 2.33 | 6079.80 |
| Boiling Point@1atm | K | 373.10 | 194.60 |
| Critical Pressure | MPa | 22.10 | 7.38 |
| Critical Temperature | K | 647.30 | 304.20 |
| Density@25C | $kg/m^3$ | 997.00 | 1.77 |
| Surface Tension@300K | N/mx10 | 0.72 | N/A |
| Viscosity@300K | $Ns/m^2$ | 855.00 | 14.90 |
| Solubility Parameter | $MPa^{\frac{1}{2}}$ | 47.90 | 12.30 |
| Molar Volume | $cm^3$/g-mole | 18.00 | 55.00 |
| Heat of Vaporization | kJ/g-mole | 2.26 | 16.04 |
| Diffusion Constant | $m^3/s\times10^{-9}$ | 1.77 | 1.77 |

Table 2.2: Physical properties of water and carbon dioxide.

# 2.3  Experimental Conditions

## 2.3.1  Test Liquid

The test liquid consisted of water saturated with carbon dioxide under various constant pressures. Each sample was kept under pressure for at least eight hours: This was the experimentally determined time for supersaturation. A summary of the properties of water and carbon dioxide can be seen in Table 2.2.

## 2.3.2  Summary of Run Conditions

The only parameter varied was the initial saturation pressure—the reservoir pressure was set to 3.0±0.7 kPa. A summary of run conditions can be seen in Table 2.3 for each view. $P_{init}$, $P_{res}$, $h_{init}$ and $h_{fin}$ represent the initial and reservoir pressures, and the initial and final heights of the liquid, respectively. Liquid heights are in compliance with the adjacent scale, and do not include 2.54 cm of liquid obscured by the test–cell holder plate. Measurements are presented in this manner so that the heights given in the table correspond to those that will be seen in the pictures.

| Run Conditions | Unit | Views | | |
|---|---|---|---|---|
| | | Interface | Intermediate | Exit |
| $P_{init}$ | kPa | 620.50 | 624.00 | 610.20 |
| $P_{res}$ | kPa | 4.41 | 4.14 | 3.79 |
| $h_{init}$ | cm | 16.80 | 16.60 | 16.00 |
| $h_{fin}$ | cm | 5.50 | 4.00 | 4.50 |
| $P_{init}$ | kPa | 637.80 | 644.70 | 648.10 |
| $P_{res}$ | kPa | 5.17 | 3.52 | 2.90 |
| $h_{init}$ | cm | 16.60 | 15.50 | 15.80 |
| $h_{fin}$ | cm | 3.60 | 2.40 | 2.00 |
| $P_{init}$ | kPa | 706.70 | 706.7 | 689.50 |
| $P_{res}$ | kPa | 3.45 | 3.45 | 3.58 |
| $h_{init}$ | cm | 15.80 | 16.40 | 16.40 |
| $h_{fin}$ | cm | 2.00 | 1.80 | 1.50 |
| $P_{init}$ | kPa | 855.00 | 844.60 | 851.50 |
| $P_{res}$ | kPa | 4.96 | 3.58 | 4.41 |
| $h_{init}$ | cm | 16.70 | 16.50 | 17.20 |
| $h_{fin}$ | cm | 4.00 | | 3.00 |
| $P_{init}$ | kPa | 1040.90 | 1054.90 | 1048.00 |
| $P_{res}$ | kPa | 3.86 | 3.45 | 3.31 |
| $h_{init}$ | cm | 16.20 | 16.40 | 16.20 |
| $h_{fin}$ | cm | 2.30 | 0.50 | 2.50 |

Table 2.3: Summary of run conditions.

# 2.4  Experimental Procedure

## 2.4.1  Pre–Experimental Operations

There are several tasks that must be accomplished in order to complete a successful run. First the test liquid must be prepared; this was accomplished by pouring $\frac{3}{8}$ l of distilled water in a 0.5 l stainless steel bottle. Next, a vacuum was pulled to remove any air above or dissolved in the water; carbon dioxide was then injected into the void, bringing the bottle to the desired test pressure. The water remained at this pressure for at least eight hours. The test–cell was soaked over night in a laboratory glass cleaning solution.

## 2.4.2  Experimental Operations

It was necessary to isolate the metal bottom from the test solution with a fluid that would not nucleate at the test conditions. A buffer layer of distilled, thoroughly degassed water was found to work well in suppressing heterogeneous nucleation. The first step was to boil the buffer water. Next the test–cell was assembled: The glass tube was taken out of the Micro brand cleaning solution (manufactured by International Products Corporation) and placed between the test–cell holder and adapter plate; the ends were sealed by compression. Torque on each rod was measured to ensure an equal load distribution was applied on the glass tube. The test–cell was then rinsed a few times with alcohol and distilled water to remove any foreign particles introduced during the assembly process. Once the buffer water cooled, 50 ml was poured into the test–cell; it was then sealed using an appropriate diaphragm (see Table 2.4) to prevent contamination.

The reservoir adapter plate was bolted to the low pressure tank, and the test–cell assembly was inserted into the protective box and attached to the reservoir adapter plate via two stainless steel rods. Pressure transducers, fill line and general access lines were connected. A vacuum was pulled for about 2 hours on the test–cell to completely degas the buffer water. The test–cell was then pressurized with carbon dioxide to the

| Diaphram Thickness (mm) | Burst Pressure (kPa) |
|---|---|
| 50.8 | 149.1 |
| 76.2 | 335.7 |
| 101.6 | 581.9 |
| 152.4 | 1056.5 |

Table 2.4: Burst pressure of diaphragms.

desired test pressure (test liquid pressure), and the test liquid was introduced into the test–cell by gravitational potential. Sometimes a small $\Delta P$—about 1 psi—was used to combat friction in the fill line; however, this was done slowly to minimize diffusion. A vacuum was pulled on the low pressure tank to bring it to the desired reservoir pressure.

The light box was positioned and adjusted behind the protective box. The Hycam was focused and loaded with film. Next the CCD camera was set–up and focused. Transducer power supply and event trigger box were turned on, and the oscilloscope trigger was set. Test–cell pressure, reservoir pressure, temperature and initial height of the test liquid were recorded. The VCR was activated; the lights were turned on; and the Hycam was triggered. The Hycam accelerated to speed and triggered the diaphragm cutter to initiate the experiment.

## 2.4.3 Post–Experimental Operations

The final height of the test liquid was recorded, and the data saved on floppy and hard disks. Photo–lamps were turned off and the Hycam was unloaded. The VCR tape was then checked for heterogeneous nucleation which might have invalidated the experiment. The test liquid bottle was refilled and prepared for another run. The test–cell was disconnected and disassembled, and the glass tubing was placed in its cleaning solution. The low pressure tank was then cleaned for the next run.

# Chapter 3  Experimental Observation

This chapter explores in detail observed effects of exsolution, from the start–up condition to the point where the liquid is finely fragmented and traveling at a constant velocity, exiting the test–cell.

## 3.1  Start–Up

In order to understand the quasi–equilibrium state, an understanding of the start up process is necessary. A pressure trace which emphasizes the features of start–up can be seen in Figure 3.1 for an initial saturation pressure of 620.5 kPa. When the diaphragm breaks, expansion waves are launched into the overlying carbon dioxide; the head of these waves travel at the sound speed of carbon dioxide. Wave amplitude is limited by choking at the exit, as is evident from the plateau in the exit pressure trace at about 391.0 kPa in Figure 3.1. Actually, there are three plateaus, the other two are located at 161 kPa and 67.3 kPa, respectively. The plateaus represent choked conditions. The initial temporal width of the expansion waves is dictated by the time it takes for the knife blade to completely open the diaphragm—this of course varies with diaphragm thickness and pressure across it. Because the opening was not filmed, no definite times can be quoted for the current experiments; however, if the opening time defined by Hill (1990) is used—the time it takes for the pressure to drop $1/e$ of the plateau pressure—then for the waves in Figure 3.1, the temporal width is estimated to be 0.46 ms with a corresponding spatial thickness of 12.35 cm.

The initial depressurization process can be considered isentropic, but are these waves weak enough to be approximated as acoustic? Relative density change can be
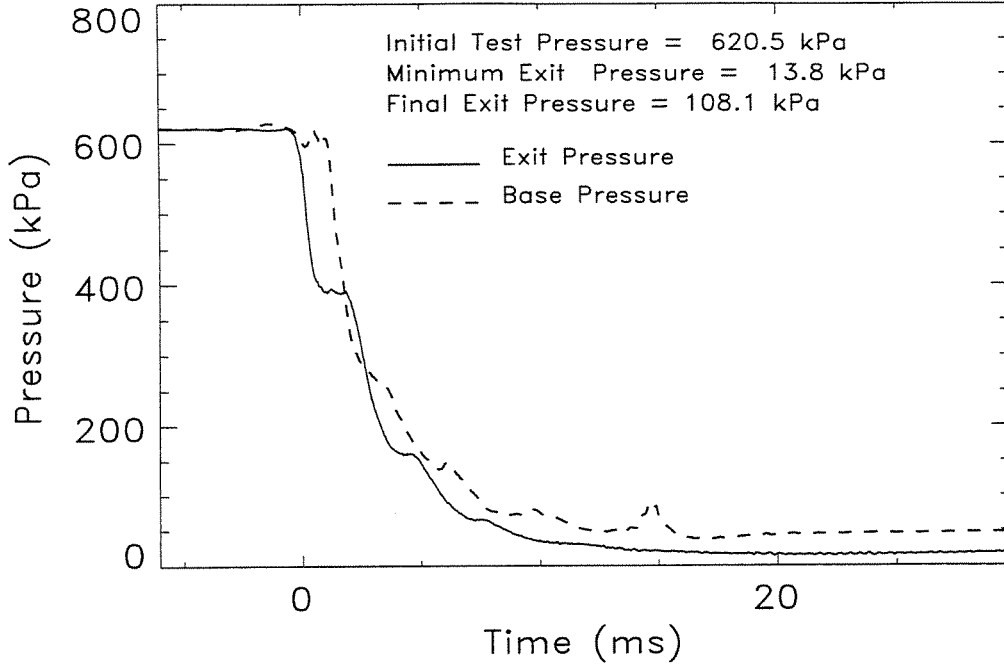
Figure 3.1: Pressure trace emphasizing start–up features.

related to pressure using the following equation:

$$\frac{\rho_{0CO_2} - \rho_{eCO_2}}{\rho_{0CO_2}} = 1 - \left(\frac{P_{eCO_2}}{P_{0CO_2}}\right)^{\frac{1}{\gamma}} \tag{3.1}$$

where 0, e, and $\gamma$ represent the initial state, exit state and ratio of specific heats, respectively. This change is about 0.44 for the case in Figure 3.1. The relative change should be much less that one for the acoustic approximation to be valid. Therefore the initial waves in carbon dioxide are not acoustic.

Once the head of the initial expansion wave reaches the liquid surface, it is partially transmitted and partially reflected. Because the ratio of acoustic impedance (liquid to carbon dioxide) is about 474, the wave behaves as though it has encountered a solid wall and reflects as an expansion wave reaching the top about 2.25 ms after the initial drop in pressure. Because the flow through the exit is choked the expansion waves reflect from the open and with no change of sign. Thus the pressure in the
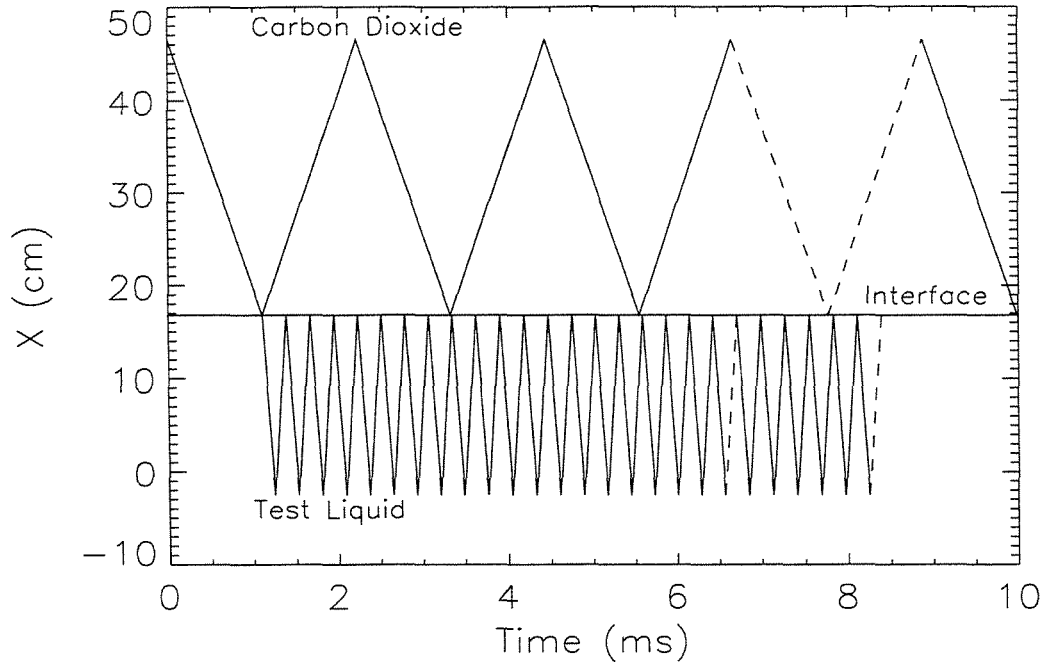
Figure 3.2: t-h diagram; $P_init$=620.5 kPa; - - compression, — expansion.

test–cell decreases monotonically, with pauses every 3 to 4 ms, the round–trip travel time of the wave, until the exit unchokes at about 6.6 ms. Then the vapor column acts like an open–ended organ pipe, and the wave changes sign each time it reflects from the open end (Figure 3.2, after 6.6 ms). After 10 ms the system has reached a quasi–steady state.

Transmitted waves enter the liquid traveling at its speed of sound and reflect from the rigid bottom as expansion waves. Owing to the large sound speed of water, there are many reverberations of waves. Eventually a steady state pressure is obtained at the bottom.

Gaseous carbon dioxide was mixed with water vapor at the initial saturation pressure. When the pressure drops, the water vapor becomes supersaturated at the new pressure state: The excess water vapor condenses to form a fog above the liquid. This is the first visual sign of depressurization. Fog scatters light more effectively than carbon dioxide, making this section of the test–cell appear dark. It begins to

form after about eight reverberations of waves in carbon dioxide, about 7.25 ms for the case in Figure 3.1. Fog forms completely in about 14 ms; once a steady state condition is established, dry $CO_2$ exsolves from the water interface and does not form a fog. A contact surface is formed separating condensed vapor from "dry" vapor. This signifies the establishment of a new state in which exsolved $CO_2$ is saturated with water vapor at the tank pressure. Figure 3.3 shows an example of a contact surface, dividing the light area above the interface from the dark region above.

Another salient feature in the base pressure signal (Figure 3.1) is the disturbance before the expansion waves reach the bottom of the test–cell. Hill (1990) observed precursor compression waves in the base transducer; his explanation was that the compression waves were created by the knife blade impacting the diaphragm, traveling down the glass and into the metal, reaching the base transducer before the expansion waves inside the test–cell. In all of the experiments performed the precursor waves were expansions and compressions occurring at 0.5 ms for this case, with associated reflections occurring at 0.85 ms and 1.05 ms, respectively, before the arrival of expansion waves in the liquid at 1.35 ms.

## 3.2  Bubble Growth

Unlike the behavior of evaporation waves, with explosive exsolution there is not a clear differentiable wave front across which the flow is accelerated to a new state. The mechanism of acceleration will be discussed in Section 3.4. Bubble structure, coalescence and fragmentation process will be discussed in detail in this section. It should also be mentioned that bubble is used "loosely" to mean cavity.

Dynamic bubble growth in infinite media can be classified into three categories: spherical, ellipsoidal and hemispherical–cap. Spherical bubbles are classified as having nearly spherical shapes, actually representable by ellipsoids with the minor axis within 10 % of the major axis. Ellipsoidal bubbles are oblate with a convex interface around the entire surface. Spherical–cap bubbles look like segments cut from spheres or from oblate spheroids of low eccentricity; they have a flat or indented base, and lack fore-

or aft–symmetry. The following is a list of parameters important to bubble growth in a dynamic field:

$$f = f\left(\rho_g, \rho_l, g, R, \mu, \sigma, U\right) \tag{3.2}$$

$\mu$ represents the coefficient of viscosity. Some dimensionless groups that result are given below (Clift *et al.* 1978).

$$Eo = \frac{g\left(\rho_l - \rho_g\right)R^2}{\sigma} \tag{3.3}$$

$$M = \frac{g\left(\rho_l - \rho_g\right)\mu^4}{\rho_l^2\sigma^3} \tag{3.4}$$

$$Re = \frac{\rho_l U R}{\mu} \tag{3.5}$$

$$We = \frac{\rho_l U^2 R}{\sigma} \tag{3.6}$$

$$Fr = \frac{U^2}{gR} \tag{3.7}$$

These groups represent the Eötvös, Morton, Reynolds, Weber and Froude numbers, respectively. The values of these parameters can be used to predict the shape that a bubble will adapt as well as other important features in the flow.

## 3.2.1 Liquid State After Initial Depressurization

As discussed in an earlier section, initial depressurization takes place via a series of isentropic waves which finally establish quasi–equilibrium states at the exit and base of the test–cell. In the liquid, this process is essentially isothermal with no notable

change in volume. The pressure differential across the liquid is given by the new quasi–equilibrium states at the exit and base of the test–cell; this can be seen for example in Figure 3.1 after about 8 ms. Figure 3.3a shows a series of pictures with the camera viewing the liquid interface. No bubbles have been formed in the liquid at this time.

## 3.2.2 Initial Growth of Bubbles in Column

In the new quasi–equilibrium state, pressure is much lower than it was before depressurization, so the initial volume of dissolved carbon dioxide can't remain dissolved. Cavities are formed into which carbon dioxide diffuses while being converted from a liquid–like state back to a gaseous state. The reason this does not occur sooner is because initial waves reflect and establish equilibrium faster than the liquid can respond by diffusion. Figures 3.3 through 3.5 show a series of pictures for an initial pressure of 706.7 kPa with the camera viewing the liquid interface. About 6.0 ms after the fog begins to form, bubbles appear in the liquid. It should be noted that time for the motion pictures is related to when the fog first appears. Bubbles start to appear at the interface and propagate down into the liquid; however, this process is spatially nonuniform and temporally unsteady. No large scale motions are observed until about 17 ms. As individual bubbles grow under the dynamical field, they become distorted: The structures are more discernible, and the detectable shapes are ellipsoidal. At this time no global motions are detectable with the given measuring technique.

A buffer layer of degassed water was used at the bottom of the test–cell to remove any gas trapped in the metal bottom. The test liquid was injected slowly from the top such that the liquid contacted the walls of the test–cell to minimize mixing. Even though much care was taken to avoid diffusion between the two liquids, total isolation was impossible. If total isolation during filling were possible, there would still be a motion of the interface induced by the initial waves. Because the buffer water was not allowed sufficient time to become saturated with carbon dioxide from above, the
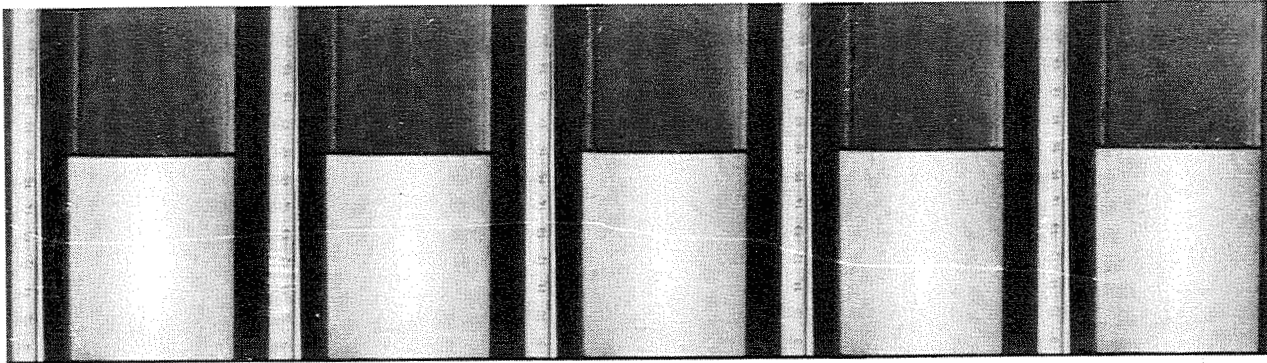
(a.) t=5.7–7.0 ms.
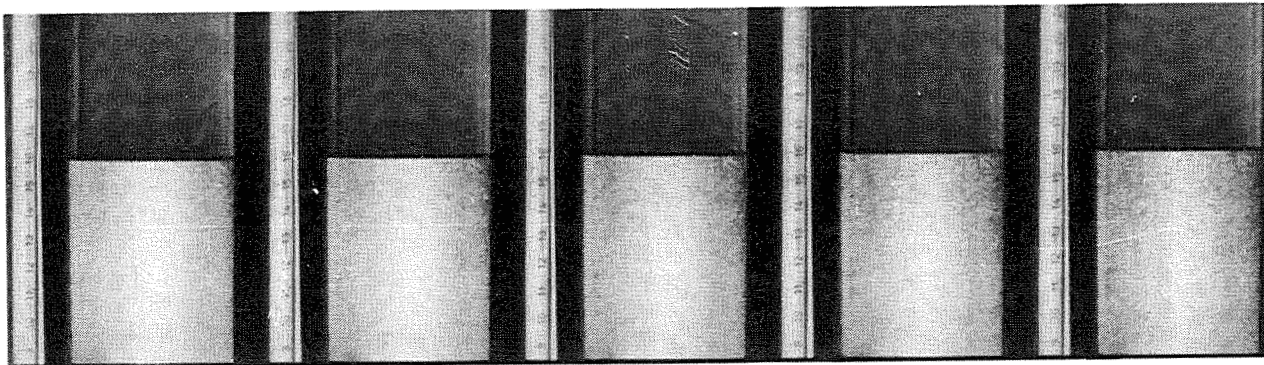


(b.) t=7.3–8.7 ms.
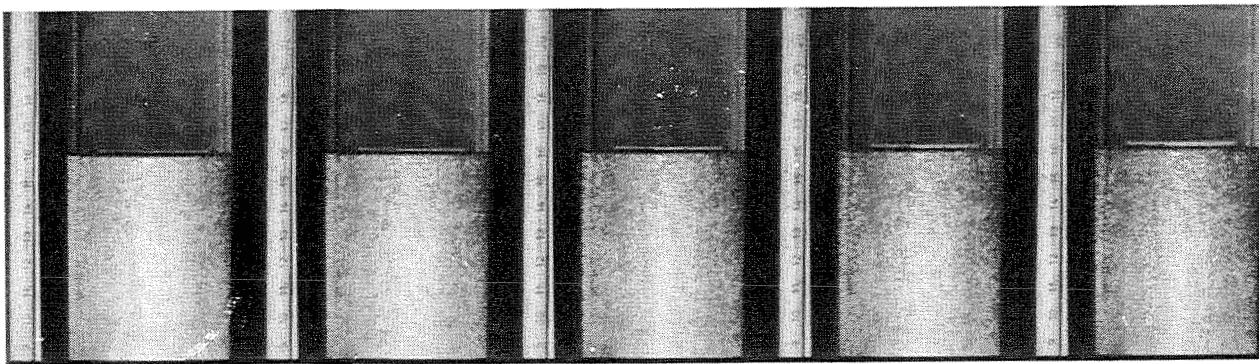


(c.) t=9.0–10.3 ms.

Figure 3.3: $P_{init}$=706.7 kPa.
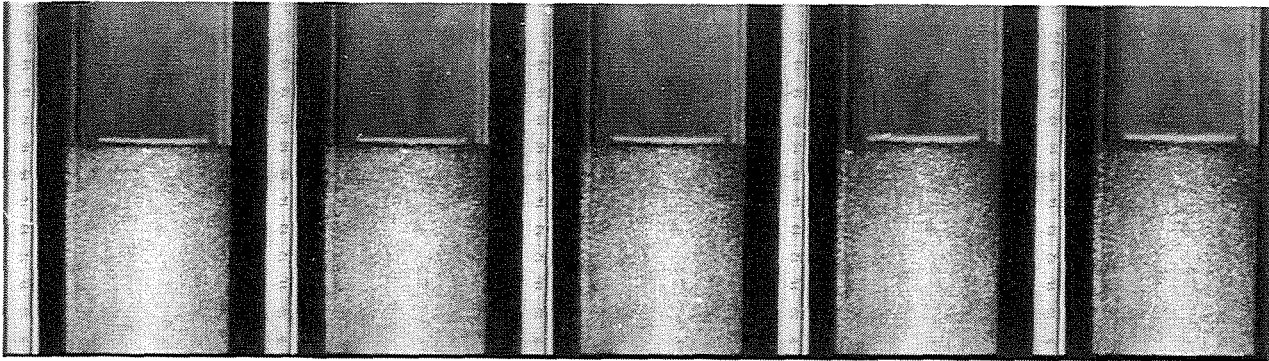
(a.) t=10.7–12.0 ms.
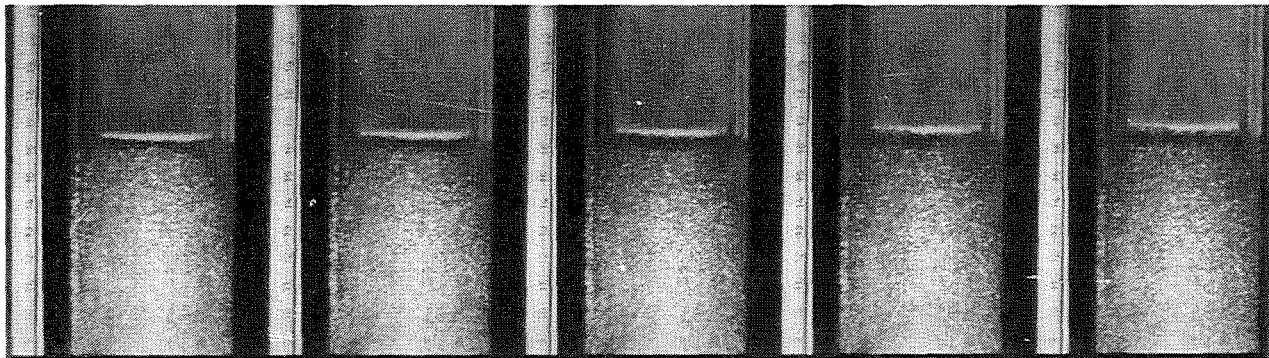


(b.) t=12.3–13.7 ms.
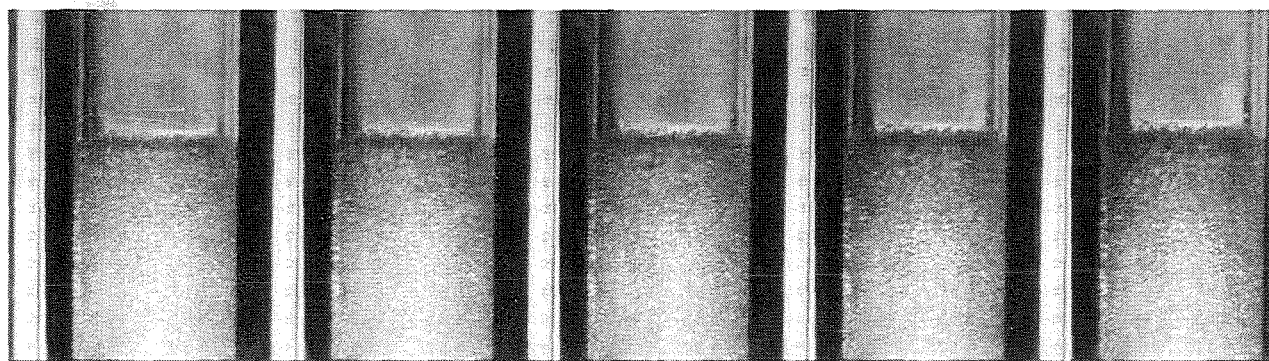


(c.) t=14.0–15.3 ms.

Figure 3.4: $P_{init}$=706.7 kPa.
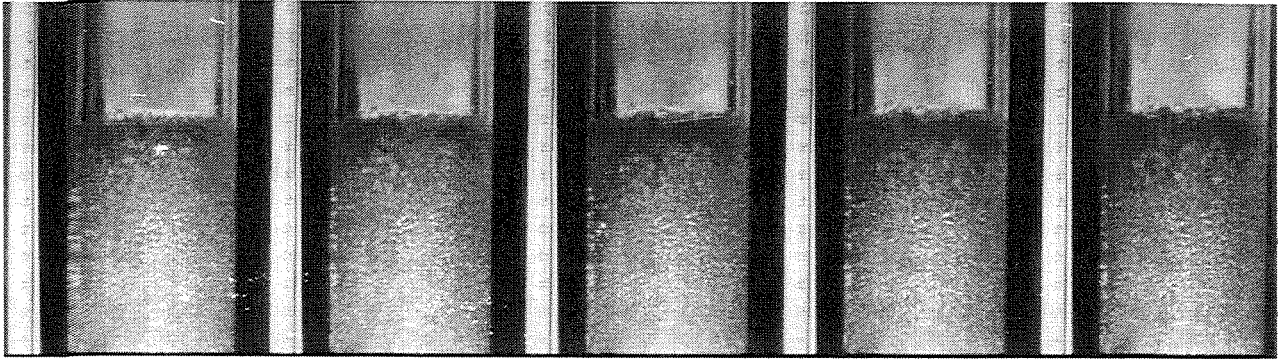
(a.) t=15.7–17.0 ms.
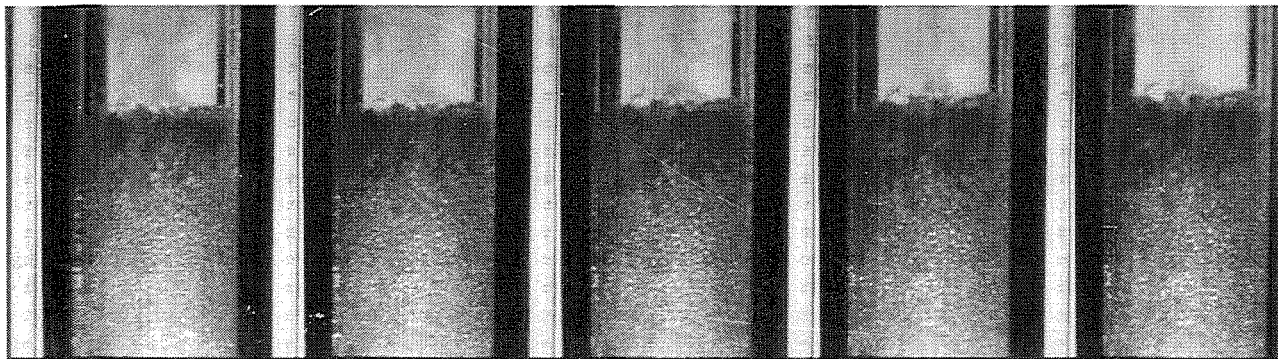


(b.) t=17.3–18.7 ms.
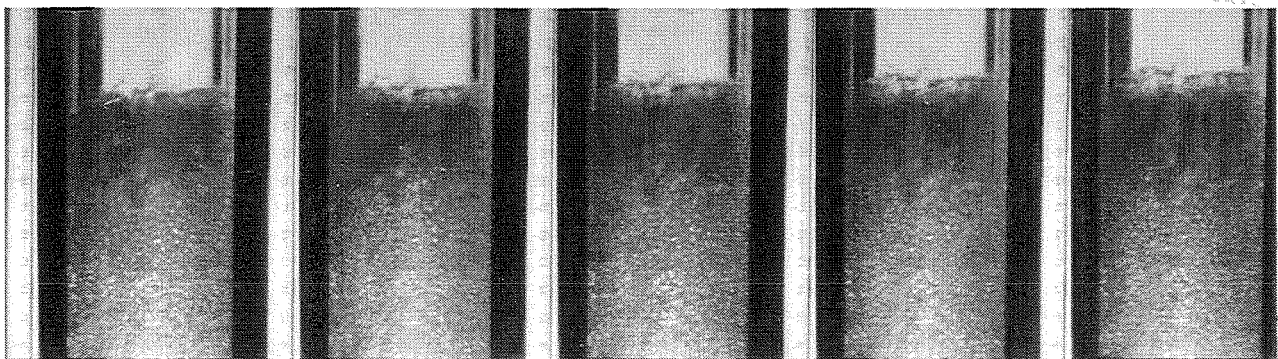


(c.) t=19.0–20.3 ms.

Figure 3.5: $P_{init}$=706.7 kPa.

two liquids were at different states. As a result, very few bubbles formed in the buffer water, and did not grow fast enough to affect the global structure of the flow.

### 3.2.3 Bubble Coalescence and Fragmentation

Each bubble has a definite limit to which it can grow before it coalesces with other bubbles and eventually fragment. The bubbles are essentially elliptical in shape when this occurs. Fragmentation produces a relatively dense aerosol which scatters light more effectively than the bubbles, giving the test–cell an even darker appearance; no individual bubbles are detectable after fragmentation at the observed spatial resolution, except at the interface. Bubble size at the point of coalesce is difficult to measure; however, they have been observed to grow as large as 2 mm in diameter. Secondary bubble growth is also detectable at the interface; this is caused by diffusion of carbon dioxide, still trapped in the aerosol, into cavities. Once a layer of bubbles breaks up, vapor continues to evolve from the droplets, adding further volume to the system. This process has not been quantified.

### 3.2.4 Bubble Growth Rates

Growth rate averaged over the volume of the test fluid was determined by measuring the change in the interface position with respect to time. No still pictures were taken to accurately measure the size and growth of individual bubbles. Consider an t-h diagram constructed for a case where the initial pressure was 706.7 kPa, Figure 3.6. Time for the experiments began when fog was observed, the intermediate and exit curves were shifted to align with the interface view. The shifts can be seen in Table 3.1. The interface region on the t-h diagram was fitted with a quadratic equation; the transition and exit regions were fitted with a linear equation. Figure 3.6 shows an example of the fits in the three regions. The quadratic portion of the t-h diagram represents constant acceleration and bubble growth which primarily occurs in the interface view. Once the fluid leaves the intermediate view, the flow moves with a constant velocity. The initial volume change can be described with the following

| Pressure (kPa) | Intermediate (ms) | Exit (ms) |
|---|---|---|
| 620.5 | 7.5 | -8.0 |
| 637.8 | 8.0 | 10.8 |
| 706.7 | 0.0 | -3.5 |
| 851.5 | -5.5 | 6.5 |
| 1061.8 | -9.0 | -23.0 |

Table 3.1: Summary of time shifts.

| Pressure kPa | Interface | | | Intermediate | | Exit | |
|---|---|---|---|---|---|---|---|
| | $a_0$ (cm) | $a_1$ ($\frac{m}{s}$) | $a_2$ ($\frac{m}{s^2}$) | $a_0$ (cm) | $a_1$ ($\frac{m}{s}$) | $a_0$ (cm) | $a_1$ ($\frac{m}{s}$) |
| 620.5 | 16.8 | .39 | 55.0 | 20.2 | 4.4 | 31.8 | 7.4 |
| 637.8 | 16.6 | .55 | 47.0 | 24.4 | 8.4 | 35.4 | 12.7 |
| 706.7 | 16.0 | .90 | 198.0 | 21.2 | 8.9 | 34.2 | 11.7 |
| 851.5 | 16.6 | 1.10 | 172.0 | | | 33.0 | 10.4 |
| 1061.8 | 16.0 | .51 | 479.0 | 21.3 | 9.1 | 34.2 | 9.7 |

Table 3.2: Summary of $a_i$.

equation:

$$V = \left( a_0 + a_1 t + a_2 t^2 \right) A \qquad (3.8)$$

where $a_i$—units and values can be seen in Table 3.2—are constants, and A is the cross sectional area of the test–cell, which is also a constant. If the first two terms in the series are assumed to be small compared to the last term, the bubble radius can be approximated as

$$R \approx b t^{\frac{2}{3}} \qquad (3.9)$$

where b, $\left( \frac{4a_2}{3\pi n} \right)^{\frac{1}{3}}$, is a constant—n represent the number of bubbles at a given time. Growth rates for all the cases observed (620.5 kPa–1054.9 kPa) exhibited the same behavior—the other t-h diagrams can be seen in Figures 3.11 to 3.14. Equations 1.11 and 3.9 can be equated to show the number of bubbles computed at 10 ms (4 ms
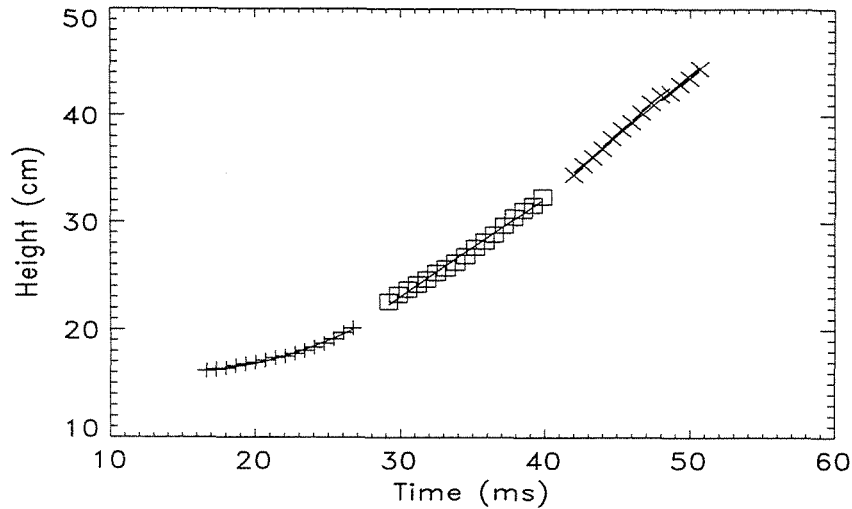
Figure 3.6: t-h diagram; $P_{init}$=706.7 kPa.

after bubbles start to grow) is 3000. A convective velocity of 1 m/s was used—this was calculated from the classical hydrodynamics terminal velocity equation, assuming an acceleration of 40 g and a drag coefficient of one. Also $C_\infty$ was assumed to be much greater than $C_0$, and $P_f$ much greater than $P_v$. A radius of 0.8 mm was used. Figure 3.3a shows that the number of bubbles present at that time is on the order of thousands.

## 3.3  Dynamical Effects of Bubble Growth

After fragmentation occurs, the liquid and carbon dioxide are finely dispersed into aerosol, Figure 3.5 for example. Some small structures begin to break away from the interface; these structures are more prevalent in the exit view. The various stages of coalescence are gauged by their ability to scatter light: The two extremes being the undisturbed liquid and finely dispersed aerosol. There is also some secondary bubble growth which may be seen at the interface, Figure 3.4. These structures are sparse and do not grow large enough to become influential.

Figure 3.7 show a sequence of pictures of the flow near the top of the test–cell. Far down stream, the liquid interface has been reduced to a streak with independent

structures proceeding it; this nonuniform propagation is caused by local unsteady accelerations at the interface in the former, and carbon dioxide being liberated at the interface and entraining liquid, eventually reaching a terminal velocity, in the latter. These structures begin to break away when the liquid fragments and accelerates away from the front.



Figure 3.7: $P_{init}$=689.5 kPa; t=47.3–48.7 ms.

Table 3.3 gives a summary of the accelerations and velocities for each saturation pressure along with the concentrations. They were obtained from the constants in Table 3.2 in the following manner: $W = a_1$ and $a = \frac{2a_2}{g}$, which is no more than differentiating the fits. The intermediate velocity for Case IV could not be measured because the camera was positioned too low in this run (see Figure 3.13 for t-h diagram). In the intermediate view the acceleration approaches zero; notice that the magnitude of the final velocities are of the same order as the intermediate velocities. The velocities range from about 7 to 13 m/s at the exit; the accelerations range from about 10 to 100 g.

There are several non–intuitional discrepancies that can be seen in Table 3.3. The most obvious is the decrease in acceleration from 706.7 kPa to 851.5 kPa, Cases III and IV. This behavior was not expected because the acceleration should increase with saturation pressure, Figure 3.8. In this figure the vertical scale is the dissolved

| Case | Pressure (kPa) | Concen-tration (kmole/m$^3$) | Accel-eration (g) | Mid Velocity (m/s) | Exit Velocity (m/s) |
|------|----------|-----------|-----------|-----------|-----------|
| I | 620.5 | 0.20 | 11.2 | 4.4 | 7.4 |
| II | 637.8 | 0.20 | 9.6 | 8.4 | 12.7 |
| III | 706.7 | 0.22 | 40.4 | 8.9 | 11.7 |
| IV | 851.5 | 0.26 | 35.1 | | 10.4 |
| V | 1061.8 | 0.32 | 97.6 | 9.1 | 9.7 |

Table 3.3: Acceleration and velocity summary.
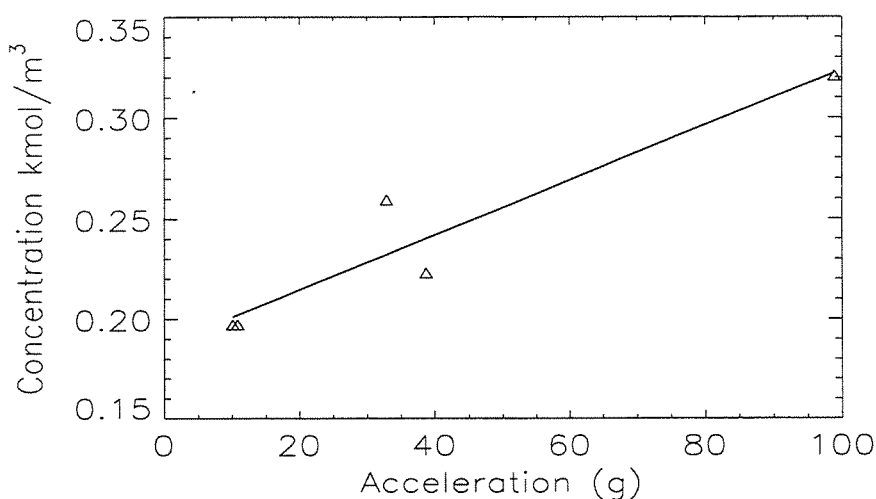


Figure 3.8: Acceleration variation with concentration.

concentration of carbon dioxide at the respective pressures, Figure 1.1. It was generally observed that the number of bubbles increases with saturation pressure, but this did not occur from Cases III to IV. The density of bubbles in Case III is such that individual bubble detection is difficult (Figure 3.5). Individual bubbles in Case IV (Figure 3.10) are more discernible and not as uniform as Case III; hence, higher acceleration is obtained with a greater number of smaller bubbles. The reason for the limited number of bubbles in Case IV could not be explained. Cases I and II pressures are too close to make any conclusive arguments; however, there is some over-lap in the interface and intermediate views (see Figure 3.11).

As the acceleration increases (increased number of bubbles), coalescence and frag-
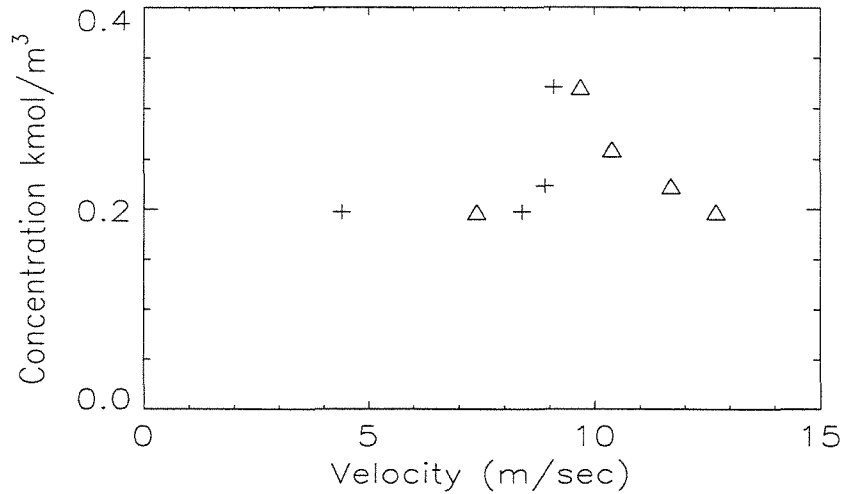
Figure 3.9: Velocity variation with concentration; + Mid Velocity, △ Exit Velocity.

| Case | Pressure (kPa) | Mid-Velocity (m/s) | Exit-Velocity (m/s) |
|------|------|------|------|
| II | 637.8 | 9.6 | 14.5 |
| III | 706.7 | 8.6 | 12.8 |
| V | 1061.8 | 9.1 | 10.5 |

Table 3.4: Forward structure terminal velocity summary.

mentation take place earlier limiting the speed to which the flow is accelerated. The difference in the exit and intermediate velocity depends on the fragmentation time scale, which depends strongly on the initial concentration (see Figure 3.9). In the extreme case, Case V, most of the acceleration takes place in the interface view. The low velocities measured in Case I can not be explained.

t-h diagrams were constructed for forward structures that broke away from the interface to measure their velocities. Table 3.4 gives a summary of the terminal velocities for three of the cases—the constants of the fits can be seen in Table 3.5. These values are close to the liquid velocities, comparing Tables 3.3 to 3.4.

| Pressure | Intermediate | | Exit | |
|---|---|---|---|---|
| kPa | $a_0$ | $a_1$ | $a_0$ | $a_1$ |
| | (cm) | $(\frac{m}{s})$ | (cm) | $(\frac{m}{s})$ |
| 637.8 | 24.4 | 9.6 | 35.6 | 14.5 |
| 706.7 | 22.4 | 8.6 | 33.7 | 12.8 |
| 1061.8 | 22.1 | 9.1 | 34.4 | 10.5 |

Table 3.5: Summary of $a_i$ for forward structures.
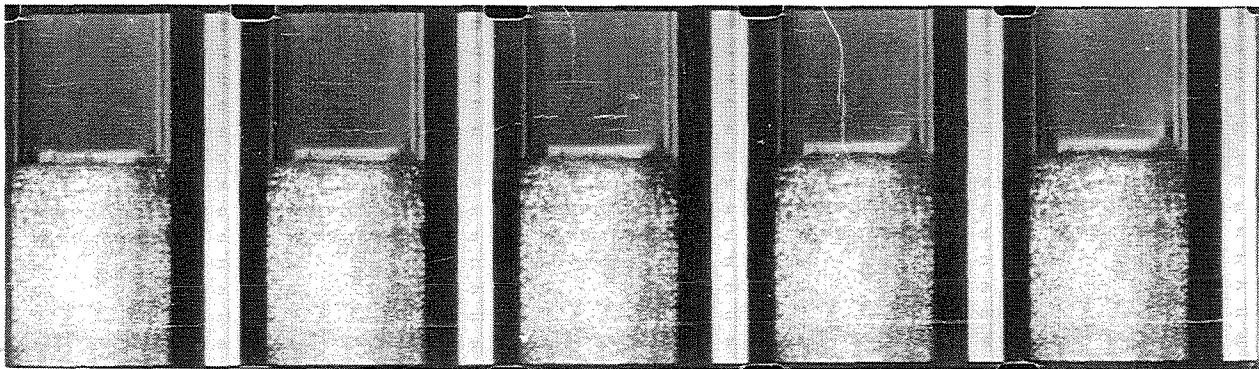


Figure 3.10: $P_{init}$=851.5 kPa; t=11.7.0–13.0 ms.
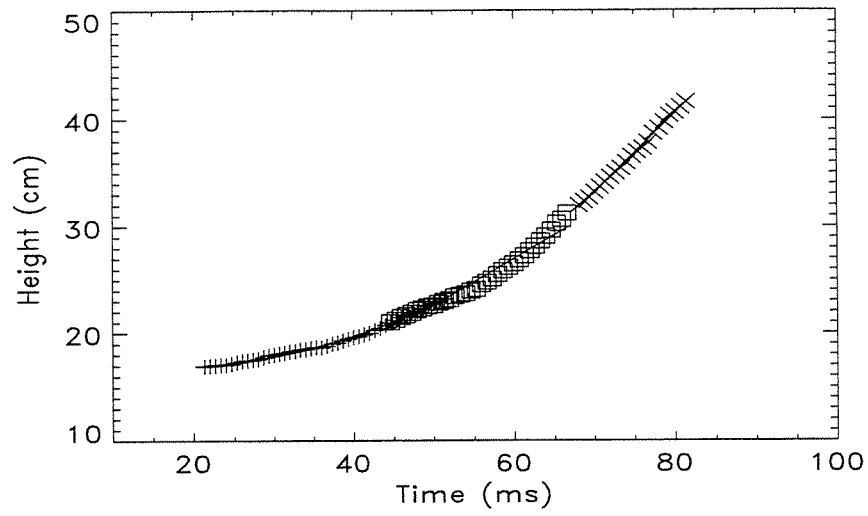
Figure 3.11: t-h diagram; $P_{init}$=620.5 kPa.
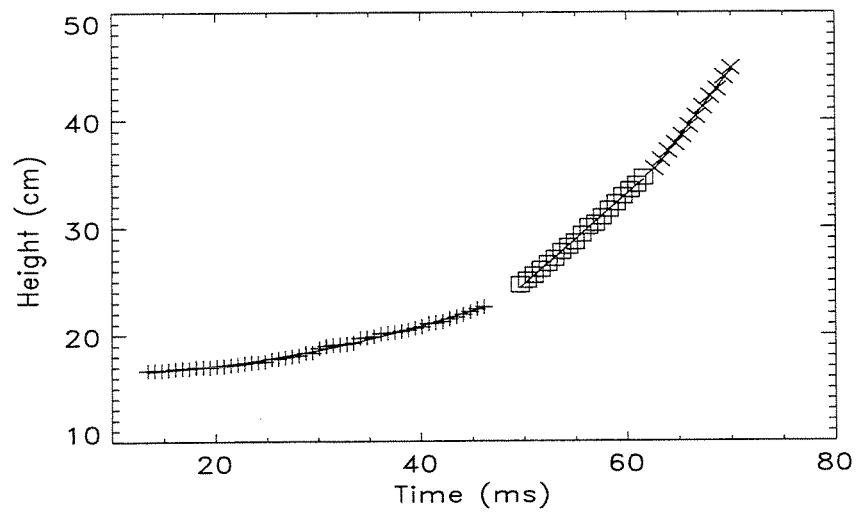


Figure 3.12: t-h diagram; $P_{init}$=637.8 kPa.
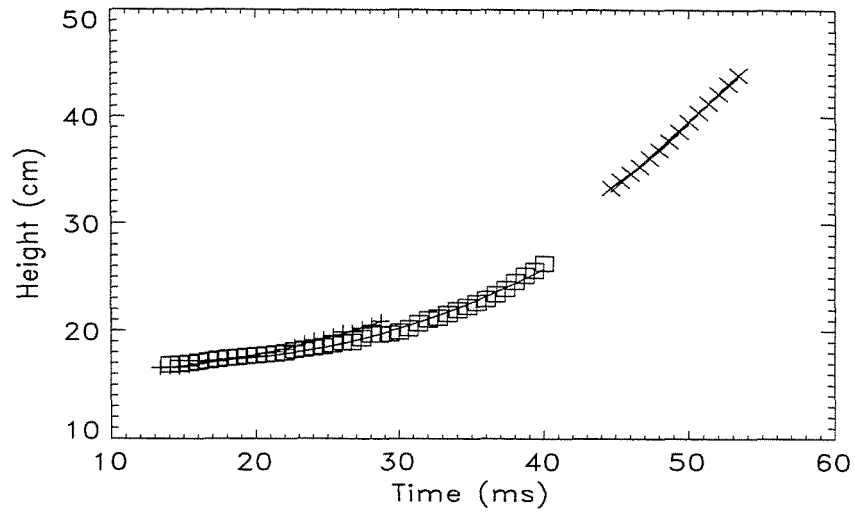
Figure 3.13: t-h diagram; $P_{init}$=851.5 kPa.
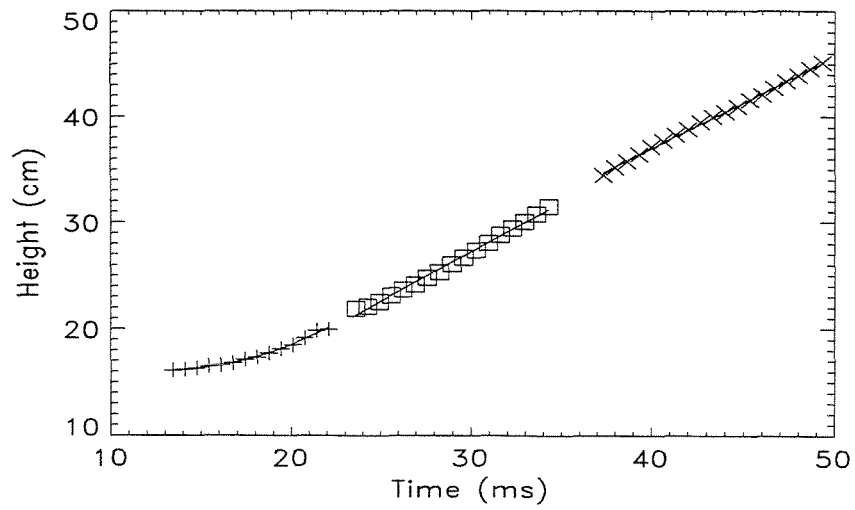


Figure 3.14: t-h diagram; $P_{init}$=1,061.8 kPa.

# Chapter 4   Conclusions

Exsolution of volatiles has been studied by depressurizing water supersaturated with carbon dioxide. Very few studies treat this phenomena despite its usefulness. When gas is dissolved in a liquid, the gas is converted into a liquid–like state even though the pressure may not be high enough to merit an actual phase change. The amount of gas dissolved is both pressure and temperature dependent. For moderate pressures and temperatures, the relationship between pressure and moles of gas dissolved is linear.

## 4.1   Start–Up

Experiments were analyzed using high speed motion pictures and pressure measurements. When the diaphragm ruptures, expansion waves are launched and reverberate in the test–cell, dropping the pressure in a few milliseconds. The first sign of depressurization is condensation resulting from a change in vapor pressure; this occurs after about eight reverberations of the initial waves above the liquid. Once a steady state pressure is obtained, a new partial pressure is established and water condensation ceases; the fog is subsequently accelerated out of the test–cell.

## 4.2   Initial Growth Of Bubbles

Once a steady state condition is achieved in the test cell, exsolution begins. Cavities form into which carbon dioxide diffuses. Initially the cavities are spherical. Bubbles start to appear at the interface, and then propagate down into the liquid; this process is spatially nonuniform and temporally unsteady.

# 4.3  Bubble Coalescence And Fragmentation

Once the bubbles fill the void in their respective regions, contact is inevitable. Further growth causes additional stress on the bubble walls eventually reaching a level that causes the walls to collapse. This process is termed fragmentation. The observed shape of the bubbles when this occurs is elliptical. Fragmentation produces dense aerosol which scatters light more efficiently than the liquid or bubbles. In this turbulent mixture of entrained carbon dioxide, secondary bubbles are formed, but do not grow large enough to become influential. Most of the liquid is expelled from the column.

# 4.4  Bubble Growth Rates

It was demonstrated theoretically that a bubble subjected to a convective velocity field grows as $t^{\frac{2}{3}}$ (Parkin 1963; Van Wijngaarden 1967). In our case, the growth rate of the entire volume was measured to infer the growth rates for individual bubbles which agreed with the theorical growth rate.

# 4.5  Dynamical Effects Of Bubble Growth

After fragmentation is completed the liquid reaches a terminal velocity and propagates out of the test cell at this speed. The liquid interface does not maintain its integrity: The center of the liquid protrudes ahead of the main body; in addition, some small structures break away from this protrusion. t-h diagrams were constructed for each pressure case; acceleration, transitional and constant velocity regions were shown. The spatial and temporal resolution of these cases depends on the initial saturation pressure.

For pressures ranging from 620.5 kPa to 1061.8 kPa, accelerations on the order of 10 to 100 g were obtained. The exit velocity peaked around 13 m/s at 637.8 kPa, and decreased to 9 m/s at 1061.8 kPa. However, the general trend is a decrease in

exit velocity and an increase in acceleration for an increase in saturation pressure. There is a discrepancy in acceleration, Cases III and IV. This is attributed to the number of bubbles observed: More bubbles should have been seen in Case IV, but the converse was actually observed. The velocity of the forward moving structures are also tabulated; they travel about 1 m/s faster than the main flow.

# Bibliography

Anilkumar, A. V., Sparks, R. S. J. & Sturtevant, B. 1993 Geological Implications and Applications of High Velocity Two-Phase Flow Experiments. In press, *J. Volcanol. Geothermal Res.*

Atkins, P. W. 1982 *Physical Chemistry.* 2nd Ed.,W.H. Freeman, CA.

Avedisian A. 1985 The Homogeneous Nucleation Limits of Liquids. *J. Phys. Chem. Ref. Data*, **14**, 695-728.

Barbone R., Frost A. & Nerenberg J. 1994 Explosive Boiling of a Depressurized Volatile Liquid. *IUTAM Symposium*, Kyoto, Japan.

Barton Allan F. M. 1983 *Handbook of Solubility Parameters and Other Cohension Parameters.* 2nd Edition, CRC Press.

Bennett, F.D., Kahl, G.D. & Wedemeyer, E.H. 1964 Resistance Changes Caused by Vaporization Waves in Exploding Wires. in *Exploding Wires*, **3**, Eds. W.G. Chace and H.K. Moore, Plenum Press, New York.

Bennett, F. D. 1971 Vaporization Waves in Explosive Volcanism. *Nature*, **234**, 538-439.

Bennett, F. D. 1974 On Volcanic Ash Formation. *American J. of Science*, **274**, 648-661.

Brennen, Christopher Earls 1995 *Cavitation and Bubble Dynamics.* Oxford University Press, NY.

Clift, R., Grace, J. R. & Weber, M. E. 1978 *Bubbles, drops, and particles.* Academic Press, NY.

Dodds, W. S. Stutzman L. F. & Sollami B. J. 1956 Carbon Dioxide Solubility in Water. *Indus. Eng. and Chem.*, **1**, 92-95

Eddington R. B. 1966 Investigation of Shock Phenomena in a Supersonic Two–Phase Tunnel. AIAA Paper, No. 66-87, *3rd Aerospace Science Meeting*, Jan. 24-26.

England, C. 1986 Gas Solubilities in Physical Solvents. *Chem. Eng.*, **93**, 63-66.

Epstein P. S. & Plesset M. S. 1950 On the stability of gas bubbles in liquid-gas solutions, *J. Chem. Phys.*, **18**, 1505-1509.

Field, J. E. 1991 The physics of liquid impact, shock wave interactions with cavities, and the implications to shock wave lithotripsy. *Phys. Med. biol.*, **36**, 1475-1484.

Fritz, G. 1965 Coolant ejection studies with analogy experiments, *Proc. Conf. on Safety of Fast Reactors*, ANL-7120, 890.

Frost D. & Sturtevant B. 1986 Effects of ambient pressure on the instability of a liquid boiling explosively at the superheat limit. *J. Heat Trans.*, **108**, 418-424.

Frost, D. L. 1988 Dynamics of explosive boiling of a droplet. *Phys. Fluids*, **31**, 2554-2561.

Grolmes M.A. & Fauske, H.K. 1974 Axial propagation of free surface boiling into superheated liquids in vertical tubes. *Proc. Fifth Intl. Heat Transfer Conf.*, **4**, 30-34.

Harmathy T. Z. 1960 Velocity of Large Drops and Bubbles in Media of Infinite or Restricted Extent. *A. I. Ch. E. J.*, **6**, 281-288.

Hiderbrand J. H., Prausnitz J. M. & Scott R. L. 1970 *Regular and Related Solutions; The Solubility of Gaes, Liquids, and Solids.* Van Nostrand Reinhold Co.

Hilderbrand J. H. & Scott R. L. 1964 *The Solubility of Nonelectrolytes.*, 3rd Edition, Dover Publication.

Hill R. C., Miller C. W. & Tucker A. 1994 Influence of Carbon Dioxide on Venous Gas Emboli Production During Altitude Decompression in Goats. *Aviation, Space and Enviro. Med.*, **65**, 139-143.

Hill L. G. & Sturtevant B. 1990 An experimental study of evaporation waves in a superheated liquid. Adiabatic Waves in Liquid-vapor Systems eds. G.E.A. Meier & P.A. Thompson, *IUTAM Symp.*, Gottingen, Germany, 25-37.

Hill L. G. 1991 An experimental study of evaporation waves in a superheated liquid. Ph.D. Thesis, Graduate Aeronautical Laboratories, California Institute of Technology.

Houghton, G., Mclean, A. M. & Ritchie, P. D. 1956 Compressibility, fugacity, and water–solubility of carbon dioxide in the region 0–36 atm. and 0–100deg. *Chem. Eng. Sci.*, **6**, 132-137.

Ikeda T., Okamoto Y. & Hashimoto A. 1993 Bubble Formation & Decompression Sickness on Direct Ascent From Shallow Air Saturation Diving. *Aviation, Space and Enviro. Med.*, **64**, 121-125.

Kieffer S. W. & Sturtevant B. 1984 Laboratory studies of volcanic jets. *J. Geophys. Res.*, **89**, 8253-8268.

Lesser, M. B. 1981 Analytic solutions of liquid–drop impact problems. *Proc. R. Lond.*, **377**, 289-308.

Lesser, M. B. & Feild, J. E. 1983 The Impact of Compressible Liquids, *Ann. Rev. Fluid. Mech.*, **15**, 97-122.

Levich, V. G. 1962 *Physicochemical Hydrodynamics.* Prentice–Hall, NJ.

Lush, P. A. 1983 Impact of a liquid mass on a perfectly plastic solid. *J. Fluid Mech.*, **135**, 373-387.

Mader H.M., Zhang Y., Phillips J.C., Sparks R.S.J., Sturtevant B. & Stolper E.M. 1994 Experimental simulations of explosive degassing of magma. *Nature*, **372**, 85-88.

Matsumoto Y. & Takemura F. 1994 Influence of Internal Phenomena on Gas Bubble Motion Effects of Thermal Diffusion, Phase Change on the Gas–Liquid Interface and Mass Diffusion between Vapor and Noncondensable Gas in the Collapsing Phase. *JSME Inter. J.*, **37**, 288-296.

Melamed Y., Shupak A. & Bitterman H. 1992 Medical Problems Associated With Underwater Diving. *New Eng. J. of Med.*, **326**, 30-35.

Mesler R. 1982 Research on Nucleate Boiling. *Chem. Eng. Educ.*, **Fall 1982**, 152-156.

Mesler R. & Bellows W. S. 1988 Explosive Boiling: A Chain Reaction Involving Secondary Nucleation. *ASME Proceeding of the 1988 National Heat Transfer Conference*, **HTD–Vol. 96**, 487-491.

Moreira J. R. S. 1994 Adiabatic Evaporation Waves Ph.D. Thesis, Rensselar Polytechnic Institute.

Parkin B. R. & Kermeen R. W. 1963 The Roles of Convective Air Diffusion and Liquid Tensile Stresses During Cavitation Inception. *Proc. IAHR Symposium on Cavitation and Hydraulic Machinery*, Sendai, Japan.

Peebles, F. N. & Garber, H. J. 1953 Studies on the motion of gas bubbles in liquids. *Chem. Eng. Prog.*, **49**, 88-97.

Plesset, M. 1962 Bubble Dynamics. Report 85–23, Division of Eng. and App. Scie., California Institute of Technology, CA.

Prosperetti A. & Plesset M. 1977 Vapor–bubble growth in a superheated liquid. *J. Fluid Mech.*, **85**, 349-368.

Shepherd, J. E. 1980 Dynamics of Vapor Explosions: Rapid Evaporation and Instability of Butane Droplets Exploding at the Superheat Limit. Ph.D. Thesis, Graduate Aeronautical Laboratories, California Institute of Technology.

Shinada, M. 1994 Influence of Gas Diffusion on Fluid Transient Phenomena Associated with Column Separation Generated during Decompression Operation. *JSME Inter. J.*, **37**, 457-466.

Shino, K. 1978 *Principles of Solution and Solubility*. M. Deker, NY.

Sparks R. S. J. 1978a The dynamics of bubble formation and growth in magmas: A review and analysis. *J. Vol. & Geothermal Res.*, **3**, 1-37.

Sparks R. S. J. 1978b The dynamics of bubble formation and growth in magmas: A review and analysis. *J. Vol. & Geothermal Res.*, **3**, 1-37.

Sparks, R. S. J., Wilson L. & Hulme G. 1978c Theoretical modeling of the generation, movement, and emplacement of pyroclastic flows by column collapse. *J. Geophys. Res.*, **83**, 1727-1739.

Sparks, R. S. J. 1978d The Dynamics of Bubble Formation and Growth in Magmas: a Review and Analysis. *J. Vol. & Geothermal Res.*, **3**, 1-37.

Sparks R. S. J. 1986 The dimensions and dynamics of volcanic eruption columns. Bull. *Volcanol.*, **48**, 3-15.

Sun, D. C. & Brewe, D. E. 1992 Two Reference Time Scales for Studying the Dynamic Cavitation of Liquid Films, Trans. *ASME*, **114**, 612-615.

Toba Y. 1959 Drop Production by Bursting of Air Bubbles on the Sea Surface II Theoretical Study on the Shape of Floating Bubbles. *J. Oceanographical Soc. of Japan*, **15**, 1-10.

Toramaru A. 1988 Formation of propagation pattern in two-phase flow systems with application to volcanic eruptions. *Geophys. J.*, **95**, 613-623.

Toramaru A. 1989 Vesiculation process and bubble size distributions in ascending magmas with constant velocities. *J. Geophys. Res.*, **94**, 17523-17542.

Van Liew H. D., Conkin J. & Burkard M. E. 1994 Probabilistic Model of Altitude Decompression Sickness Based on Mechanistic Premises. *J. Appl. Physiol.*, **76**, 2726-2734.

Van Liew H. D. & Burkard M. E. 1993 Density of Decompression Bubbles and Competition for Gas Among Bubbles, Tissue, and Blood. *J. Appl. Physiol.*, **75**, 2293-22301.

Wallis, G. B. 1969 *One-Dimensional Two-Phase Flow*. McGraw Hill, NY.

Wiebe R. & Gaddy V. L. 1940 The Solubility of Carbon Dioxide in Water at Various Temperatures from 12 to 40deg and at Pressures to 500 Atmospheres. Critical Phenomena. *J. Am. Chem. Soc.*, **62**, 815-817.

Wijngaarden, L. van 1967 On the growth of small cavitation bubbles by convective diffusion. *Int. J. Heat Mass Transfer*, **10**, 127-134.

Wilson L. 1976 Explosive volcanic eruptions, III, Plinian eruption columns. *Geophys. J. Roy. Astro. Soc.*, **45**, 543-556.

Wilson L., Sparks R. S. J., Huang T. C. & Watkins N. D. 1978 The control of volcanic column heights by eruption energetics and dynamics. *J. Geophys. Res.*, **83**, 1829-1836.

Wilson L. 1980a Relationships between pressure, volatile content and ejecta velocity in three types of volcanic eruption. *J. Volcanol. Geotherm. Res.*, **8**, 297-314.

Wilson L., Sparks, R.S.J., Walker G.P.L. 1980b Explosive volcanic eruptions IV. The control magma properties and conduit geometry on eruption column behavior. *Geophys. J. Roy. Astro. Soc.*, **63**, 117-148.